DIRECT DATING AND CHARACTERIZATION OF THE POPE'S HILL REE OCCURRENCE, LABRADOR.

by

©Alexander N. Chafe

A thesis submitted to the

School of Graduate Studies

in partial fulfillment of the requirements for the degree of

Master of Science

Earth Sciences

Memorial University of Newfoundland

October 2015

St. John's, Newfoundland and Labrador

ABSTRACT

The Pope's Hill (PH) rare earth element (REE) occurrence, located in central Labrador, is a syenite-hosted, highly enriched unit with whole-rock geochemical analyses indicating REE contents ranging from <1 to 22 weight percent. Samples of ore, altered host rock, and unaltered country rock, were collected throughout the occurrence in order to: 1) determine which phases concentrate the REE and also quantify their abundances and distribution in the ore; 2) determine the host rock emplacement age; 3) determine the timing of the subsequent hydrothermal alteration and REE mineralization; and 4) constrain the source of the REE using in situ LA-ICPMS and ID-TIMS U-Pb geochronology and in situ Sm-Nd isotopes using LA-MC-ICPMS in monazite.

The REE-enrichment occurs in millimeter- to decimeter-scale pods that are locally discontinuous and consist of primary and secondary REE minerals including a variety of silicate, phosphate, carbonate, and niobate phases; the most abundant being allanite-(Ce), monazite-(Ce), britholite-(Ce), and an unnamed LREE-enriched mineral similar in composition to titanite.

ID-TIMS geochronology reveals monazite dates from ~1090 to 940 Ma that coincide with Grenvillian metamorphism and plutonism during continent-continent collision suggesting that locally derived REE in the PH syenite crystalized into primary REE-silicates either before or during Grenvillian events. Microtextures in thin section indicate that secondary non-silicate REE minerals were produced by the breakdown of primary REE-silicates, suggesting either hydrothermal fluid alteration, or metamorphism.

ACKNOWLEDGEMENTS

The guidance and encouragement offered to me by John Hanchar, Chris Fisher, James Crowley, Phil Piccoli, Peter Dimmell, and Greg Dunning was instrumental in completing this project. All were a pleasure to work with and I would like to thank them for many hours of their time, often past regular working hours, where they provided invaluable knowledge, advice, and courtesy.

Financial support for this project was provided by the Research and Development Corporation (RDC) of Newfoundland and Labrador, Silver Spruce Resources Inc., and the Natural Sciences and Engineers Research Council (NSERC).

Silver Spruce Resources Inc. also graciously provided logistical support, allowing unrestricted access to their field area and samples, affording me extraordinary creative freedom. I would like to thank their staff, especially Peter Dimmell, Adree Delazzer, Wayne Doucette, Bryint, Sheldon, and Ford Savory, and James Flowers for their hard work, kindness and companionship during my time in the field.

I would like to thank my family and friends, who's support during my many years at University has gotten me through good times and bad, especially Danielle Hoddinott, my parents, grandparents, and sisters. I was so lucky to have gone through graduate school with a group of very talented, inspiring geologists whose friendships I value greatly and would like to thank them for the endless entertainment, meaningful discussions, and deep inspiration they continue to provide me.

Finally, I would like to dedicate this work to my late grandfather Ronald Henry Chafe.

Table of Contents

List of Tables

List of Figures

CHAPTER 1: INTRODUCTION

1.1 Purpose of Thesis

Global demand for REE is driven by an ever-increasing need for REE in in manufacturing industries. With Asia's dominant share of the REE market, North American companies would seek to decrease foreign dependence causing a boom in the REE exploration industry. With interest at a high point, work in Labrador during the 2010-2011 field seasons saw the development of a number of rare earth element (REE) prospects. These occurrences are spread throughout the Precambrian rocks of Labrador, from Strange Lake in the north (Fig. 1, point A), to the Red Wine Mountains (Fig. 1, point B) and Pope's Hill (Fig. 1, point C) in central, and Port Hope Simpson (Fig. 1, point D) in the southeastern Labrador. They cover multiple tectonic provinces, where the most significant prospects have been discovered in the Churchill and Grenville. The focus of this study, Pope's Hill (PH) is in the Grenville, 100 km southwest of Happy Valley/Goose Bay along the Trans-Labrador Highway (Fig.1).

Prospectors working with a junior exploration company, Silver Spruce Resources, first discovered REE mineralization at Pope's Hill. Workers noticed anomalous levels of background radiation from high levels of U-Th present in the rocks. Subsequent geochemical analyses lead to the discovery of the Pope's Hill REE potential, where assay results from hand samples reveal up to 24% total REE and are of economic grade.

This work is a comprehensive study that characterizes the ore and altered host rocks of Pope's Hill, as well as constrains the timing of the mineralization, the source of REE, and their petrogenesis. The geological setting of Pope's Hill allows this study to

have implications ranging from the future of the prospect itself, to the overall, general mobility and transport of REE through metasomatic and metamorphic systems, and the subsequent crystallization of various REE minerals. Micro-scale mineral analysis obtained by combining cathodoluminescence (CL), back-scattered electron (BSE) imaging, and mineral liberation analysis (SEM-MLA), give a qualitative view of the REE distribution and abundance. Those images were used to guide the subsequent in situ chemical analyses, obtained by electron probe microanalysis (EPMA), laser ablation-inductively coupled plasma-mass spectrometry (LA-ICPMS) and laser ablation multi collector inductively coupled plasma-mass spectrometry (LA-MC-ICPMS), isotope dilution thermal ionization mass spectrometry (ID-TIMS) and mineral species data from powder X-ray diffraction (XRD) all of which are combined to produce a near complete characterization of the abundance, composition, and mineralogy of the abnormally high REE-enrichment at Pope's Hill. Additionally, using simultaneous U-Pb and Sm-Nd techniques laser ablation split stream (LASS) (Goudie et al., 2013) and ID-TIMS, precise dates are obtained that reveal a paragenetic sequence, which dates metamorphic and hydrothermal fluid events during REE mineral crystallization, and provides constraints on the sources of the REE at the Pope's Hill Occurrence. On an interpretive level, the dating work presented here improves our understanding of the REE-forming processes that lead to occurrences such as Pope's Hill. Characterizing, dating, and interpreting the evolution of REE-enriched hydrothermal fluids and their deposits have wide-reaching effects that are of scientific and industrial significance, as the importance of REE continues to climb in the global market.

1.2 Objectives

The objectives of this study are as follows: (1) identify the mineralogy of the economic grade REE-enriched rock at Pope's Hill, (2) determine the source of REE that formed these minerals, (3) create a paragenetic sequence of events using petrographic and geochronological evidence in order to constrain the timing of crystallization and method of emplacement, and (4) compare the genetics of the Pope's Hill REE with other REE deposits that may have experienced similar tectonic, metamorphic, or metasomatic events.

1.3 Location and Accessibility

The Pope's Hill area is located within a one-hour drive, southwest toward Churchill, along the Trans-Labrador Highway outside of the town Happy Valley – Goose Bay in central Labrador; the mainland region of the province of Newfoundland and Labrador on the eastern coast of Canada. The field area is along the Pinus River, a second-order river that drains into the Churchill River. The Churchill River runs over 700km, starting at the Smallwood basin in western Labrador, and exiting into Lake Melville close to Happy Valley – Goose Bay. Along the river is significant hydroelectric infrastructure that is developed in Churchill Falls, to the west, and under development in the east at Muskrat Falls – adjacent to our study area. The Pope's Hill Area, as claimed by Silver Spruce Resources Inc. in 2011, includes a narrow series of claims that approximately follow the Churchill River. The area is densely forested and of high topographic relief with limited outcrop exposure; mapping of the region has traditionally

been based on river traverses, compiled by Wardle et al., (1997), although the recent construction of the Trans-Labrador Highway has unearthed a limited amount of exposure in road-cuts and gravel pits.

1.4 Previous Exploration

Silver Spruce Resources discovered Pope's Hill during a regional prospecting project in 2006 when anomalous radioactivity was discovered in a gravel pit. The region would remain unexplored until 2010, when REE exploration in the Grenville Province of Labrador was at a high point. The company's first-pass at exploration discovered whole-rock grab samples, from float, assaying upwards of 20 weight percent (wt%) REE. A follow-up program in the summer of 2011 would identify the source of these rocks in situ and provide the material for this study.

1.5 Layout of Thesis

Chapter 1 of this thesis provides an introduction to REE, our study area and the objective of this project. Chapter two contains a manuscript of a paper written to be submitted to peer-reviewed scientific journal, Economic Geology. The manuscript is laid out to give a brief introduction to REE, their importance to mining and manufacturing, and an overview of significant REE deposits (Chapter 2.1) followed by a summary of the regional and local geology of Pope's Hill area (Chapter 2.2). Analytical techniques used (Chapter 2.3) and the results from analyses are presented (Chapter 2.4), where mineralogy and geochronology are discussed in detail. A discussion of the implications

of mineral chemistries, timing of crystallization and origin of REE (Chapter 2.5) precedes presentation of this study's conclusions (Chapter 2.6). Finally Chapter 3 provides the conclusion of the study and recommendations for future work.

1.6 Statement of Co-authorship

Alexander N. Chafe: I collected the samples used for this project and prepared them for whole rock assay, XRD analysis, creation of thin sections and grain mounts including all cutting, crushing, grinding and mineral separations. I collected EPMA data at the University of Maryland with the assistance of Philip M. Piccoli. I collected and reduced LA-ICPMS data including trace elements and dating with the assistance of Chris M. Fisher and John M Hanchar. I collected XRD data with the assistance of John M. Hanchar. The manuscript (Chapter 2) was written by myself and benefitted from the input, contributions, and guidance of all co-authors.

Christopher M. Fisher: Chris provided assistance with the collection of all laser analyses including trace elements and age dating, using Sm-Nd and U-Pb by LASS, as well as Sm-Nd alone. Chris provided guidance as I reduced the laser data and input on interpretations. Chris also gave constructive criticism and contributions to the manuscript providing a great deal of help and guidance.

John M. Hanchar: John designed the project and helped implementation. He assisted with preparation of samples, collection and interpretations of LA-ICPMS and XRD analyses. John provided constructive criticism and contributions throughout every stage of the project, including preparation of the manuscript.

Philip M. Piccoli: Phil ran the EPMA at the University of Maryland during data collection, reduced the data and provided input on the geochemistry of minerals. He also provided guidance on the objectives of this study as well as interpretation of results.

James L. Crowley: Jim collected ID-TIMS data at Boise State University, including "*in-situ"* TIMS analyses using a micro saw to cut material from thin sections. Jim reduced the data, produced the results and provided input on the isotopic properties of the minerals.

Peter M. Dimmell: Peter provided me with full access to the Pope's Hill area allowing me to complete the fieldwork required for this project. Peter provided fieldwork and geological guidance; access to all assay analyses collected; and contributed grammatical assistance and constructive criticism to the manuscript.

CHAPTER 2: PAPER MANUSCRIPT

Direct dating and characterization of the Pope's Hill REE Occurrence, Labrador

Alex N. Chafe[1], Christopher M. Fisher[2], John M. Hanchar[1], Philip M. Piccoli[3], James L. Crowley[4], Peter M. Dimmell[5]

[1]Department of Earth Sciences, Memorial University of Newfoundland, St. John's, Newfoundland A1B 3X5

[2]School of the Environment, Washington State University, Pullman, Washington 99164

[3]Department of Geology, University of Maryland, College Park, Maryland 20742

[4]Department of Geosciences, Boise State University, Boise, Idaho 83725

[5]Silver Spruce Resources, Inc., 59 Carpasian Rd., St. John's, NL, A1B 2R2

ABSTRACT

The Pope's Hill (PH) rare earth element (REE) occurrence, located in central Labrador, is a syenite-hosted highly enriched unit where whole-rock geochemical analyses indicate REE contents ranging from 1 to 22 weight percent. Samples of ore, altered host rock, and unaltered country rock, were collected throughout the occurrence in order to: 1) determine which phases concentrate the REE and quantify their abundances and distribution in the ore; 2) determine the host rock emplacement age; 3) determine the timing of the subsequent hydrothermal alteration and REE mineralization; and 4)

constrain the source of the REE using in situ LA-ICPMS and ID-TIMS U-Pb geochronology and in situ Sm-Nd isotopes using LA-MC-ICPMS in monazite.

The REE-enrichment occurs in millimeter- to centimeter-scale pods that are locally discontinuous and consist of primary and secondary REE minerals including a variety of silicate, phosphate, carbonate, and niobate phases; the most abundant being allanite-(Ce), monazite-(Ce), britholite-(Ce), and an unnamed LREE-enriched mineral similar in composition to titanite.

ID-TIMS geochronology reveals monazite dates from ~1090 to 940 Ma that coincide with Grenvillian metamorphism and plutonism during continent-continent collision suggesting that locally derived REE in the PH syenite crystalized into primary REE-silicates either before or during Grenvillian events. Microtextures observed in thin section indicate that secondary non-silicate REE minerals were produced by the breakdown of primary REE-silicates, suggesting either hydrothermal fluid alteration, or metamorphism.

2.1 INTRODUCTION

2.1.1 Significance of REE

The rare earth elements (REE) include the fourteen naturally occurring lanthanides discovered by European chemists through the late eighteenth and early twentieth centuries. These elements are divided into two categories, lanthanum to samarium are considered the light rare earth elements (LREE) and gadolinium to ytterbium are considered the heavy rare earth elements (HREE), while europium displays

chemical properties of both groups. Early geochemists noted that the REE all behave similarly, are very heavy, extremely immobile in the earth's crust, and have similar atomic radii. Researchers routinely use these properties to track a rock or mineral's evolution throughout the crust and mantle in order to interpretation small changes in geochemical conditions (Henderson, 1982). This widespread practice of fingerprinting the origin of natural geologic materials with trace concentrations of REE, such as in Sun (1982), Sun and McDonough (1989), and Taylor and McLennan (1985) has given the scientific community a relatively comprehensive understanding of REE behavior in natural systems. For our purposes, "REE" are defined as only the fourteen naturally occurring lanthanide elements, and do not include promethium, yttrium or scandium.

Increasing global demand for REE as critical components of high technology and consumer products lends further importance to the understanding of their natural formation in the Earth's crust. In a recent review paper, the demand for REE is driven by rapidly growing demand for modern products in which REE are more efficient and less environmentally harmful than their traditional counterparts (Goonan, 2011). For instance, powerful magnets and batteries based on Nd alloys are found in small devices, such as hard disks, servos, electric car motors and wind turbine generators; magnets and batteries made with REE have very high energy density and contain less toxic elements, making traditional technology antiquated.

The combination of the importance of REE and Asia's dominant share of the REE market (e.g., ~90%, Haxel et al. 2002), caused North American companies seek to secure their REE needs, resulting in a spike in REE prices and exploration in 2010 and 2011.

2.1.2 Characteristics of REE Deposits

Rocks that contain ore-grade REE contents (e.g., > 1% to about 25%), are orders of magnitude above the REE content of an average sedimentary, metamorphic or igneous rock. It is widely accepted that these REE enriched rocks are the result of highly evolved, often peralkaline, magmas, where fractional crystallization of compatible elements has caused enrichment of incompatible elements in residual magma (e.g. Sørensen, 1997; Markl, 2001). The incompatible-element enriched magmas can crystallize primary igneous REE-minerals under distinct pressure, temperature and chemical conditions, such as those outlined for carbonatites by Lee and Wyllie (1998b), forming low abundance, incompatible-enriched rocks in the host pluton making well-preserved examples rare. While the behavior of REEs in common crustal rocks is relatively well understood, the behavior of these highly enriched rocks throughout the complexities of metamorphic and metasomatic events remains enigmatic.

The knowledge upon which our understanding of REE behavior in ore-grade systems has been built heavily on three major deposits: the Mountain Pass Mine in San Bernardino County, California; the Strange Lake Intrusive Complex in Northern Quebec; and Bayan Obo, Inner Mongolia, China.

2.1.3 Mountain Pass

An early study of Mountain Pass by Olson et al. (1954), remains today as one of the best sources of information on the region. The REE deposits in the Mountain Pass Mine occur in highly evolved Mesoproterozoic igneous intrusive rocks varying in

composition from shonkinite, a feldspar-bearing mafic syenite, to carbonatite, a carbonate-bearing primary igneous rock. Bastnäsite ([Ce,La]CO_3F) is the primary REE-bearing mineral in the ore, accompanied by lesser monazite, allanite, cerite ($Ce_9Fe^{3+}[SiO_4]_6[SiO_3][OH]_4$), parisite ($Ca[Ce,La]_2CO_3F_2$), and sahamalite ($[Mg,Fe][Ce,La[_2[CO_3]_4$). The host rocks surrounding the ore deposit are Paleoproterozoic granulite-facies gneisses and schists that are complexly folded and banded (Castor, 2006). Metasomatic alteration by hydrothermal fluids is not thought to have played a significant role in the crystallization of REE minerals at Mountain Pass.

2.1.4 Strange Lake

One of, and possibly the largest, HREE and HFSE deposits in North America, occurs on the Quebec side of the northern Labrador-Quebec border, in the Churchill tectonic province (point A in Fig. 1). The Strange Lake Intrusive Complex is described by Boily and Williams-Jones (1994) as Mid-Proterozoic quartz undersaturated peralkaline plutons, which contain sodic amphibole and pyroxene, arfvedsonite and aegirine, respectively. Three igneous units are distinguished: a hypersolvus pluton; a subsolvus pluton; and post-emplacement pegmatites and aplites. The three granitoid rock types contain some of the highest concentrations of REE and HFSE ever reported for alkali granites. Exotic mineral phases host REE and HFSE in a number of uncommon incompatible-enriched minerals including, elpidite ($Na_2ZrSi_6O_{15}•3H_2O$), gittinsite ($CaZrSi_2O_7$), pyrochlore ($[Na,Ca]_2[Nb,Ta]_2O_6[OH,F]$), gadolinite ($(Ce,La,Nd,Y)_2Fe^{2+}Be_2Si_2O_{10}$+HREE), kainosite ($Ca_2(Ce,Y,HREE)_2Si_4O_{12}(CO_3)•H_2O$),

gagarinite ($Na(Y,Ca,No,REE)_2F_6$), bastnäsite and less exotic phases such as titanite, zircon, and thorite. These phases comprise from 10 to 50% of the volume of the pegmatite-aplite. Metasomatic alteration has played a large role in the post-emplacement mineralization of Strange Lake. Salvi and Williams-Jones (2006) describe a scenario where highly saline, F-rich hydrothermal fluids mobilize and stabilize REE and HFSE while altering sodic minerals in the granites. When these F-complex rich fluids interacted with convecting groundwater driven by heat from the pluton, they altered sodic minerals while precipitating exotic phases.

2.1.5 Bayan Obo

One of the largest known REE districts in the world, Bayan Obo is located in Inner Mongolia, China, an area where subduction and continent-continent collision drove plutonism (Wang, 1985). The main REE deposits are proximal to various carbonate and siliceous sedimentary rocks, with the main ore bodies hosted in the "H8" dolomite marble (Smith and Chengyu, 2000). The history of mineralizing events at Bayan Obo is very complex, involving many generations of various mineral species, over 170 in total, with 18 first described at the deposit, including monazite, bastnäsite and apatite (Zhang, 1991). Mineralization is found within banded, metasomatized areas and also occurs in discontinuous pods (Drew et al., 1990). REE-complexation occurred in chlorine and ligand bearing fluids (Chou and Eugster, 1977) during metasomatism associated with orogenesis, which ultimately crystallized banded and pod-like REE minerals.

2.1.6 REE Deposits in Labrador

With interest for REE exploration at a high point, exploration and research in Labrador during the 2010-2011 field seasons saw the development of a number of potential REE occurrences, in addition to a significant exploration undertaken at Strange Lake. These occurrences, summarized in a review paper by Kerr (2011), are spread throughout the Precambrian rocks of Labrador, from the Red Wine Mountains in northwestern Labrador, to Pope's Hill in central Labrador, to the Port Hope Simpson area on the southeastern coast of Labrador (Gower et al. 2011) (Fig. 1 points B, C and D). Not enough research has been done (i.e., U-Pb geochronology and tracer radiogenic isotopes such as Sm-Nd), to determine any relationship between these REE occurrences.

As summarized by Kerr and Rafuse (2011), the Red Wine Intrusive Suite consists of two Mesoproterozoic metamorphosed peralkaline plutons consisting of quartz-undersaturated rocks and quartz-bearing rocks. REE are found primarily in the undersaturated syenite in a complex silicate mineral eudialyte ($Na_4[Ca,Ce]_2[Fe^{2+},Mn,Y]ZrSi_8O_{22}[OH,Cl]_2$.), that has a highly variable chemical composition (Kerr and Rafuse, 2011, Table 1).

On the south Labrador coast, the recently discovered Port Hope Simpson REE District, also described by Kerr and Rafuse (2011), lies on the boundary between the Grenvillian Lake Melville and Pinware Terranes. The REE occurrences are found in an extensive, anomalously radioactive, Paleoproterozoic orthogneiss that is fine-grained and of quartzofeldspathic composition.

2.2 GEOLOGIC SETTING

2.2.1 Regional Geology

The Pope's Hill REE occurrence is located on the east coast of Canada in central Labrador. Four tectonic boundaries divide Labrador (Fig. 1), the Churchill (Paleoproterozoic) and Nain (Archean) in the north, Superior (Archean) in the west and the Grenville (Paleoproterozoic to Mesoproterozoic) in the south. Locally, deformation in the gneiss is heterogeneous; immediately surrounding the REE host rocks are phyllite, mylonite, banded gneiss and anastomosing granitic gneiss. The polylithic nature of the orthogneiss country rock was investigated during sample collection and mapping for this project. The country rock contains layers that are generally meter-scale; pink coarse-grained granitic layers containing plagioclase, alkali feldspars and quartz with minor hornblende, chlorite, garnet, chalcopyrite and pyrite were common. Contrasting dark grey layers are biotite or amphibole-rich and are weakly magnetic. Continuous coarse-grained granitic pegmatites, on decimeter- to meter-scale are perpendicular, subparallel, and parallel, to gneissosity indicating that they were emplaced both syn- and post-deformation. Although the majority of gneiss layers contain only trace amounts of REE, syenitic layers, similar to those hosting the massive PH mineralization, occur infrequently throughout the area, and contain enrichment in REE up to 1000 ppm. These syenites have been characterized, and dated (sample PH-5), with monazite found as the only REE-bearing mineral of significance. The units are distinguished from the pink granite gneiss by their >80% abundance of alkali feldspar and slightly anomalous radioactivity, most likely due to thorium in monazite.

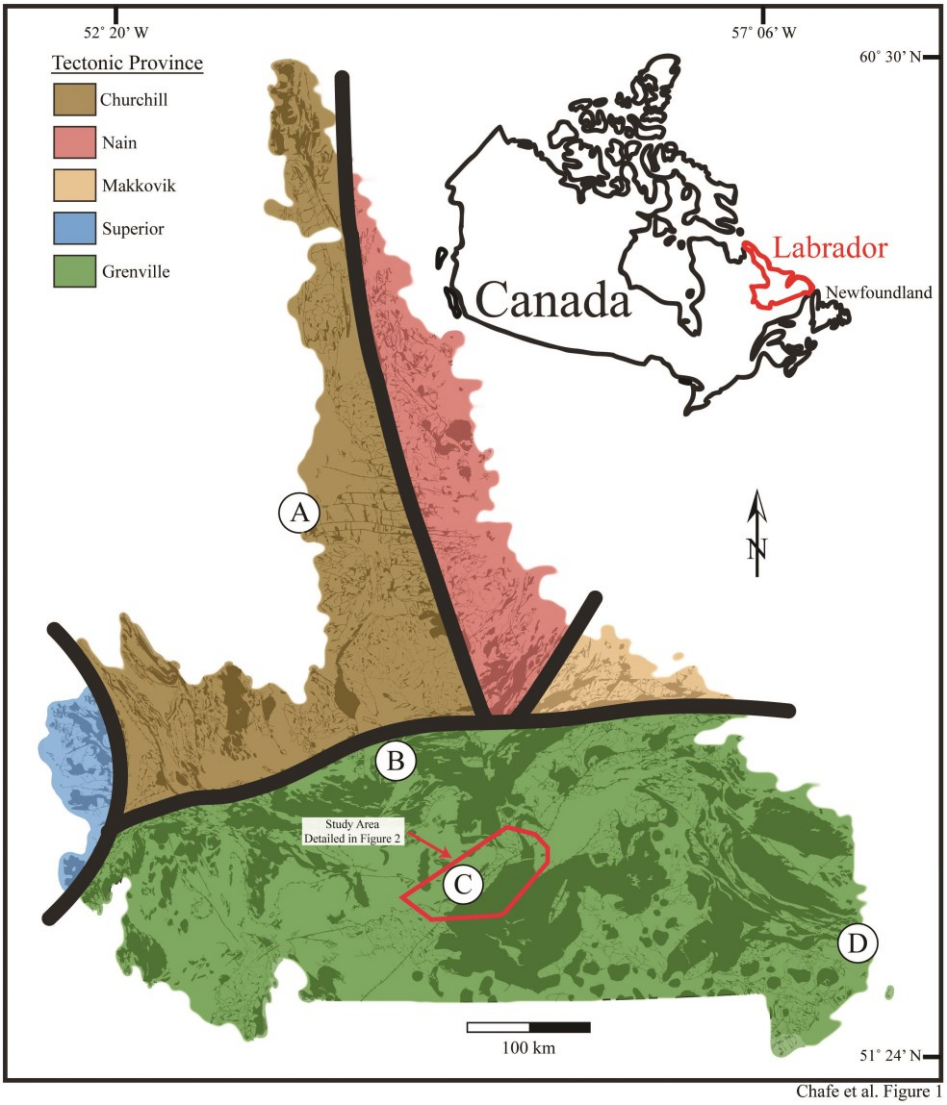

Figure 1.

A simplified geological map of Labrador (after Wardle et al. 1990) showing tectonic boundaries and terranes, from north to south; Churchill Province, in dark brown; Nain Province, in red; Makkovik Province on the east coast, in light brown; Superior Province, to the west and in blue; and Grenville Province, covering central and southern Labrador, in green. Locations of significant REE deposits are labeled: A - Strange Lake intrusive complex on the Labrador-Quebec border: B - Red Wine intrusive suite; C - Pope's Hill and MRT, the focus of this study; D - Port Hope–Simpson REE district. The red box shows the area of the detailed map, Figure 2.

Schärer et al. (1986) dated accessory minerals of the Eastern Grenville terrane in Labrador reporting U-Pb zircon, monazite, and titanite mixed dates with end members at ~1700 and ~1030 Ma. These two populations are also reported in Schärer and Gower (1988, Fig. 5) in detail and form the framework of the Grenville in this region, indicating emplacement of the protolith at ~1735 Ma followed by granulite facies metamorphism between 1671 and 1633 Ma, and later extensive reworking during the Grenville orogeny around 1030 Ma. Banded migmatic gneiss from Mealy Mountain terrane, sample CG-495 reported by Schärer et al. (1986, Fig 9b), shows a concordia diagram with concordant monazite and discordant zircon analyses. The monazite reveals Grenvillian, Late Mesoproterozoic ages ~1030 Ma. A regression line drawn through monazite and zircon has an upper intercept of 1677 Ma. The Grenville was experiencing a change from arc-related plutonism, at ~1230 Ma, to back arc extension associated with intra-plate plutonism, ~1180 Ma (Rivers, 1997), which was interpreted by Corrigan and Hanmer (1995) as the beginning of continent-continent collision during the Grenville Orogeny.

2.2.2 The Pope's Hill REE Showing

Two REE occurrences have been discovered in an area between 40 and 100 km west of Happy Valley-Goose Bay along the Trans Labrador Highway (Fig. 2),

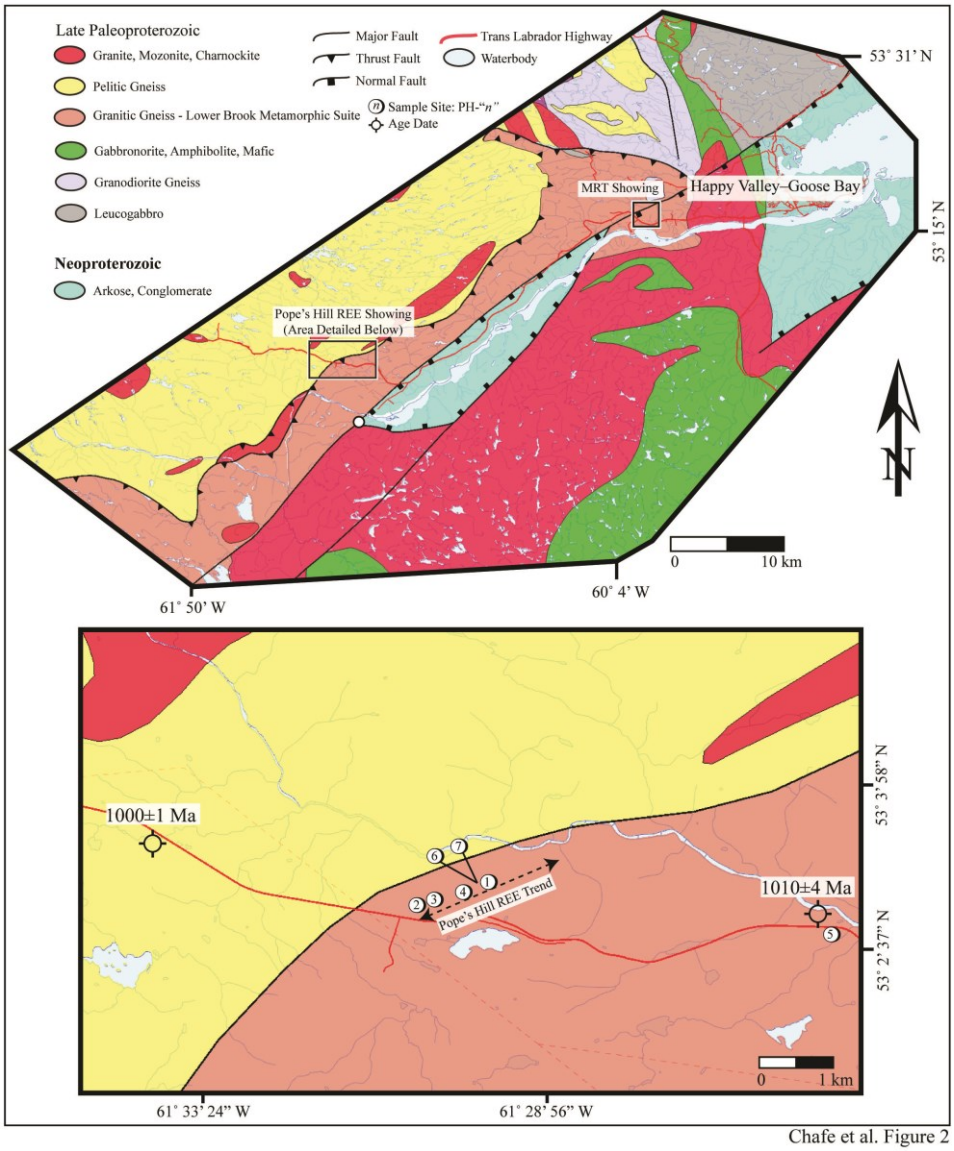

Figure 2.

Geological map of the Pope's Hill region outside of Happy Valley–Goose Bay, Labrador, after Wardle, et al. (1990), showing both the Pope's Hill and MRT REE prospects, with Pope's Hill expanded. The surface expression of the deposit is outlined in red and circles mark the locations of key samples.

referred to as Pope's Hill and MRT. The Pope's Hill Occurrence in the southwest and the "Mr. T" Prospect (MRT) in the northeast form a linear northeast-southwest trend; approximately parallel to the Churchill River Valley.

The orthogneiss that hosts the Pope's Hill showing, known as the Lower Brook Metamorphic Suite (LBMS), follows the northeastern regional strike, while geophysical surveys indicate that MRT is located within an anticline. Both prospects are densely forested and of moderate to high topographic relief with limited outcrop exposure. Regional mapping was initially done on river traverses (Wardle et al., 1997), however, with the completion of the Trans-Labrador Highway through that area, construction exposed new outcrops in road-cuts and gravel pits including those that are the focus of this study.

Initial reconnaissance exploration in the area was carried out in 2010 and involved the collection of whole-rock samples, from glacial and alluvial float, which gave whole rock assays containing up to 24 weight percent (wt. %) REE. The author (A. Chafe) and the staff of Silver Spruce Resources began fieldwork for this study the following year and identified the source of these REE-enriched float in situ (Fig. 3a and 3b). The mineralization occurs in radioactively anomalous disconnected "pods" hosted in pink, medium-grained, perthitic quartz syenite that dips ~60˚ to the southeast (Fig. 3c). These pods cause only a slight anomaly on a hand-held scintillometer, an increase from background values of 150 counts per second (CPS, which includes cumulative alpha, beta and gamma emissions) to 200 CPS above the 5 to 30 cm thick, humus, A and B soil horizons although the increase is enough to locate mineralization. After hand trenching

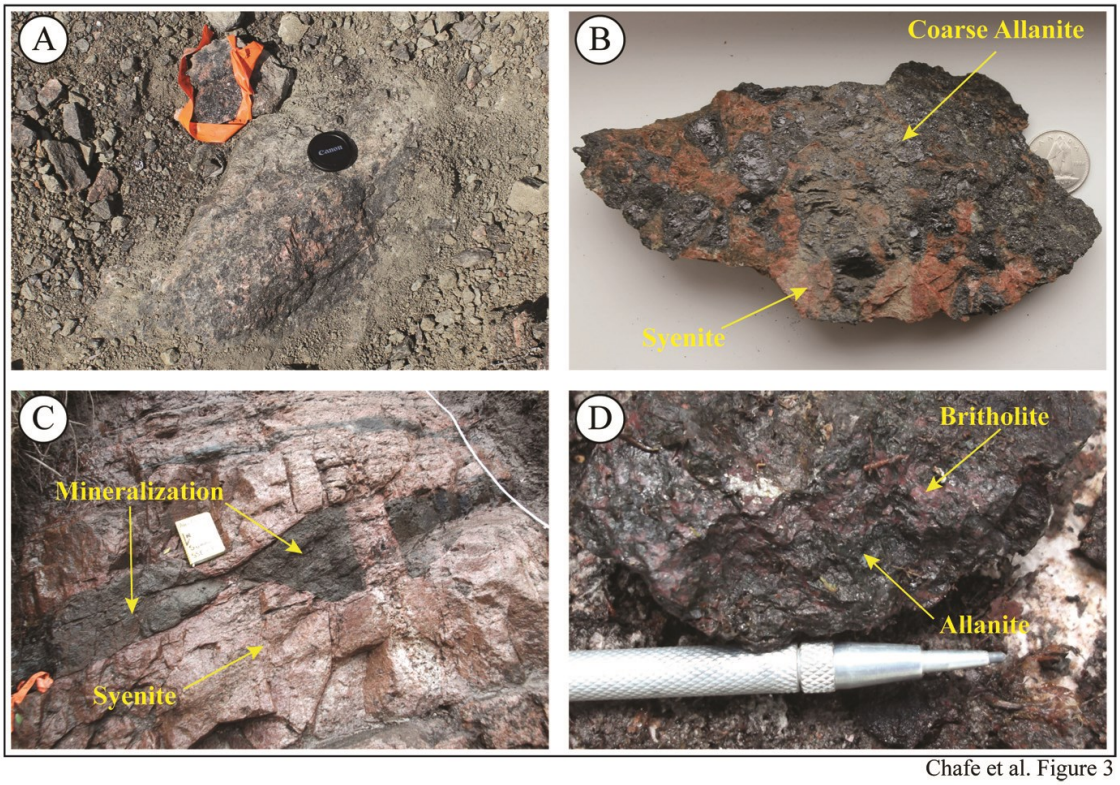

Figure 3

An overview of the mineralized outcrop and hand samples from initial prospecting work. A and B show the REE mineralization initially identified in a gravel pit on the TLH, at sample site PH-3 (Fig. 2), the dark grey-black, coarse allanite in a pink syenitic host, which led to the discovery of the Pope's Hill REE prospect. At sample site PH-1, (C) mineralization in dark grey-green to black weathered "massive pods" pinch and swell in a pink syenitic host and are cross cut by a small discontinuous pegmatite dike. In D, the fresh surface of a hand sample shows allanite, finer than in A and B, associated with an earthy red mineral, later identified as britholite.

the exposed bedrock, measures up to 6000 CPS in a distinctive vitreous dark-grey and earthy red coarse-grained mixture of glassy, metamict, minerals including allanite in the host rock. These pods are up to 40 x 20 cm and are oriented parallel to the regional gneissic fabric, and to the fabric of the foliated syenitic host rock, indicating coeval deformation with the host rock. Fist-sized samples, commonly found on the land surface on bedrock, replicate the initial 20 wt% REE prospecting samples. The massive pods were extensively sampled during this project and are well represented by sample PH-1.

In addition to the massive pods, the REE-rich material is present in fine, ~5 mm wide bands, which occur parallel to the foliation and occupy, at most, 30% of the outcrop surface. The syenite also contains fine grain green bands of hedenbergite ± hornblende ± biotite, which can be macroscopically mistaken for a REE-rich band, but are distinguished based on their low radioactivity, earthy luster and medium to dark green colour. The mineralization has been traced, using a scintillometer to detect radioactivity, for ~2.8 km and, as of 2011, remains open-ended in both directions. Contacts between the host syenite and the granitic gneiss country rock are covered with vegetation, however, the width of the host syenite intrusion is estimated to be greater than 30 m based on field observations, where REE pod-bearing layers are up to 10 m thick.

2.3 ANALYTICAL METHODS

2.3.1 Sample Collection and Preparation

Samples for this study were collected during exploration of the REE occurrences at Pope's Hill and MRT by A. Chafe and came from prospecting, field mapping, trench excavation and sampling using rock saw, and diamond drilling. Sampling for REE mineralization focused on three rock types: (1) mineralized REE-enriched samples, referred to as ore, taken from areas where values reach tens of weight percent REE (PH-1, PH-2, PH-3, PH-4); (2) syenite samples, taken in the Pope's Hill area, including samples from the syenite that hosts the massive mineralization and syenitic layers outside the mineralization (PH-5, PH-6, PH-7); (3) country rock, consisting mainly of the gneiss typical in the LBMS which are not REE-enriched (PH-8, PH-9, PH-10, PH-11, PH-12, PH-13); and (4) mineralized and unmineralized samples taken from the MRT showing (MRT-1, MRT-2, MRT-3, MRT-4, MRT-5) A full list of sample names is given in Appendix 1, Table A1. These four group divisions will remain, and their geochemistry, mineralogy and geochronology will be discussed accordingly. Thirty-two (32) samples, of hundreds taken, were selected as characteristic of their respective group, and a thin section of each was made by Texas Petrographic Services. After petrographic examination using transmitted and polarized light supplemented by CL imaging, nineteen of these samples were selected for analysis and labeled based as either "PH" or "MRT" based on their locality as follows: typical Pope's Hill massive REE mineralization is best represented in two samples, PH-1 and PH-2; MRT mineralization is characterized by sample MRT-1; syenite is characterized by sample PH-5; and granitic gneiss country rock

is characterized by sample PH-10. In addition to thin sections, samples were crushed using a jaw crusher and disk mill with portions used for both XRD and assay for major, trace element, and tracer radiogenic isotopes (The work completed on samples is summarized in Appendix 1).

For trace element and Sm-Nd isotopic analysis, and dating by LA-ICPMS and ID-TIMS, zircon, monazite, titanite, britholite (the Si and REE end-member of the apatite group) and fergusonite were separated using standard heavy liquid and magnetic separation techniques. Before analysis, these mineral separates were mounted in epoxy pucks, polished and then imaged by Scanning Electron Microscope (SEM).

2.3.2 Whole Rock Geochemistry

Since essentially all available laboratory standards contain a much lower concentration of REE than in our whole rock samples of massive mineralization, both ActLabs of Ancaster, Ontario and Memorial University of Newfoundland's (MUN) TERRA facility for whole rock major, minor, and trace element analyses ensured data accuracy. Routine commercial packages were used at each: 4LithoResearch+Code 8-REE at ActLabs; and TERRA's major and trace element package. To complement in situ Sm-Nd isotope analyses, samples analyzed by MUN TERRA TIMS facility for whole rock Sm-Nd isotope analysis.

2.3.3 EPMA

A JEOL JXA-8900 SuperProbe EPMA at the Department of Geology at the University of Maryland was used for imaging and determining mineral compositions from polished thin sections. Energy dispersive spectroscopy (EDS) was used to aid in mineral identification. Quantitative mineral chemistry was determined using standard wavelength dispersive spectroscopy (WDS) techniques..

In total four element schedules were run by WDS techniques: the first optimized for analysis of allanite, titanite and fergusonite, which included SiO_2, Al_2O_3, FeO, MnO, CaO, Na_2O, TiO_2, As_2O_5, SrO, ZrO_2, Nb_2O_5, BaO, La_2O_3, Ce_2O_3, Pr_2O_3, Nd_2O_3, Sm_2O_3, Eu_2O_3, Gd_2O_3, Dy_2O_3, Yb_2O_3, Ta_2O_5, PbO, ThO_2, UO_2, Cl and F; the second for apatite-britholite, monazite and REE-carbonates, which included SiO_2, FeO, MnO, CaO, Na_2O, P_2O_5, As_2O_5, SrO, BaO, La_2O_3, Ce_2O_3, Eu_2O_3, Nd_2O_3, Sm_2O_3, Gd_2O_3, Dy_2O_3, Yb_2O_3, Y_2O_3, PbO, ThO_2, UO_2, SO_3, Cl and F; the third for pyroxene and amphibole including SiO_2, Al_2O_3, FeO, MnO, MgO, CaO, Na_2O, K_2O, TiO_2 and BaO; and the fourth, optimized for feldspars include SiO_2, Al_2O_3, FeO, MnO, MgO, CaO, Na_2O, K_2O, TiO_2, Rb_2O, SrO and BaO.

2.3.4 SEM

To investigate mineral abundances and textures, we completed full thin section mapping and additional BSE imaging was completed using SEM-MLA at the MAFIIC SEM facility of MUN, using the FEI MLA 650F with BrukerXFlask 5030 SDD X-ray detectors, at 25 kV and 10 nA and the MLA software (Gu and Napier-Munn, 1997).

Imaging of epoxy mounts was completed using standard BSE imaging techniques, focusing on single grains of zircon, in order to discern any internal heterogeneity shown as variations in mean atomic number. These images were used to ensure in situ LA-ICPMS analyses would not mix core and rim dates. Grains from heavy mineral separates mounted into epoxy were examined for apatite-britholite and monazite in order to obtain material for future ID-TIMS analysis.

2.3.5 LA-ICPMS

In order to better quantify the abundance of trace elements and to complete in situ Sm-Nd isotopes, we collected data from thin sections at the MAF-IIC LA-ICPMS laboratory using a GEOLAS 193mm excimer laser, coupled to either a the single collector Finnigan XR mass spectrometer, a multi-collector Finnigan NEPTUNE, or both simultaneously using the newly developed LASS technique, as outlined by Goudie et al. (2013). For trace element analyses, standard NIST 610 glass was used for primary standardization, supplemented by BCR-2G and NIST 612 glass as secondary standards. Additionally probe data for Ca from allanite and britholite, Y for fergusonite, Th for monazite and Si for titanite minerals was used as an internal standard while processing trace element data using Iolite software (e.g., Paton et al., 2011). For the LA-ICPMS U-Pb geochronology, zircon 91500 (Wiedenbeck et al., 2004), trebilcock monazite and an LREE-enriched glass Sm-Nd isotope analyses (Fisher et al., 2011) were used depending on the composition of the mineral being analyzed.

2.3.6 ID-TIMS

Samples, PH-1, PH-2 and PH-5, were sent to Boise State University (BSU), where Dr. J. Crowley completed high precision ID-TIMS U-Pb analyses using mineral fragments from monazite, titanite, allanite and fergusonite extracted from thin sections and epoxy mounts. Dates were corrected for ^{204}Pb using the model of Stacey and Kramers (1975) for samples PH-1 and PH-5, while for sample PH-2 the composition of common Pb was taken from analyses of K-feldspar separated from the sample. ID-TIMS dates are presented as $^{207}Pb/^{235}U$ in order to avoid Th/U correction issues common in monazite (Parrish, 1990), as the high Th/U ratio in allanite, titanite and monazite would likely create $^{206}Pb/^{238}U$ ages older than crystallization. Fergusonite dates are discordant and have the lowest Th/U, thus $^{206}Pb/^{238}U$ dates are presumed accurate for this mineral.

2.3.7 XRD

We examined the mineral structure of these highly enriched REE phases by powder XRD at the MUN TERRA XRD laboratory. A Rigaku Ultima IV X-ray diffractometer was used at room temperature from 5˚ to 115˚ 2θ with 0.5˚ intervals and a collection time of 2 seconds. Data were processed using JADE software to identify the mineral phases.

2.4 RESULTS

2.4.1 Whole Rock Geochemistry

Both ActLabs and MUN data are in good agreement, proving the robustness of each laboratory's internal standardization techniques for high-grade whole rock REE samples. The data from ActLabs (Table 1) show samples ranging from 0.99 to 21.90% REE (Fig. 4). Major elements typical of syenite, SiO_2, Al_2O_3, Na_2O, and K_2O are in negative correlation with REE, while FeO, CaO, TiO_2 and P_2O_5 have a positive relationship, indicative of the chemistry of the REE minerals influencing the whole rock chemistry. Incompatible trace elements are correlated with REE enrichment including Y, Hf, Th, U, Nb, Ta, and Pb; Zr behaves indifferently or is depleted; Ba becomes depleted.

Whole rock chondrite normalized REE patterns from Pope's Hill samples (Fig. 5) indicate that all samples show Eu-depletion and as REE concentration varies, the slope from all samples at Pope's Hill remains the same. Un-REE enriched syenite samples from Pope's Hill plot <0.5% REE.

Whole rock Sm and Nd concentrations in mineralized sample, PH-1 are highly enriched with values for Nd and Sm of ~44,000 ppm and 7000 ppm, respectively. The syenitic country rock, PH-5 contains ~89 ppm Nd and 8.9 ppm Sm, while the regional granitic gneiss, PH-10 has ~122 ppm Nd and 23.2 ppm Sm (data are summarized in Appendix 1). All ID-TIMS concentration data agree to within ~4% of the ActLabs data (Table 1).

Table 1

TABLE 1. WHOLE ROCK MAJOR AND TRACE ELEMENT GEOCHEMISTRY

Sample	Ore				Syenite			Host Rock		
	PH-1	PH-2	PH-3	PH-4	PH-5	PH-6	PH-7	PH-8	PH-9	PH-10
%										
SiO_2	31.52	45.23	41.44	33.93	71.80	63.70	60.93	52.15	67.11	58.86
Al_2O_3	4.75	7.62	5.06	1.24	14.36	15.93	18.34	13.68	14.85	16.64
Fe_2O_3(T)	10.17	17.83	22.99	26.71	1.44	4.52	5.03	7.81	5.43	8.97
MnO	0.24	0.39	0.59	0.43	0.03	0.10	0.21	0.10	0.10	0.19
MgO	0.24	0.63	0.60	0.96	0.28	0.53	0.50	6.64	1.43	0.20
CaO	10.46	9.45	13.69	10.95	0.49	1.72	1.24	4.66	2.67	3.50
Na_2O	0.33	1.72	1.30	0.47	4.20	4.17	4.54	1.53	2.82	4.49
K2O	0.52	2.32	1.21	0.16	5.71	6.73	7.23	7.38	3.81	5.30
TiO_2	4.37	2.02	0.68	1.57	0.18	0.06	0.44	2.28	0.75	0.76
P_2O_5	4.84	1.85	2.00	2.58	0.03	0.08	0.03	1.78	0.23	0.16
LOI	1.42	1.44	0.36	2.40	0.24	0.70	0.82	1.43	0.07	0.00
Total	68.85*	90.5*	89.92*	81.39*	98.76	98.24	99.30	99.44	99.26	98.52
Nb_2O_5	0.54	N.D.	N.D.	0.18	N.D.	N.D.†	N.D.	N.D.	N.D.	N.D.
TREE§	21.90	7.77	5.96	13.07	0.07	0.08	0.04	0.07	0.04	0.06
ppm										
Sc	45	25	25	26	2	11	7	13	12	10
Be	4	6	19	14	2	2	1	2	2	3
V	34	12	11	13	13	16	15	187	77	7
Cr	< 20	< 20	< 20	< 20	< 20	< 20	< 20	230	< 20	< 20
Co	46	88	41	33	172	88	63	75	152	80
Ni	< 20	< 20	< 20	< 20	< 20	< 20	< 20	200	< 20	< 20
Cu	< 10	30	110	40	< 10	20	30	20	40	10
Zn	150	390	540	720	< 30	70	40	120	70	160
Ga	493	194	141	281	20	27	24	21	18	30
Ge	126	52.90	40.50	80.40	1.60	2.80	2.20	2.00	2.20	2.80
As	376	136	94	223	< 5	< 5	< 5	< 5	< 5	< 5
Rb	5	43	28	2	137	160	146	164	114	100
Sr	177	236	221	387	1370	138	293	3052	290	131

TABLE 1. WHOLE ROCK MAJOR AND TRACE ELEMENT GEOCHEMISTRY

Sample	Ore				Syenite			Host Rock		
	PH-1	PH-2	PH-3	PH-4	PH-5	PH-6	PH-7	PH-8	PH-9	PH-10
Y	15800	4460	8300	14200	11	91	120	23.90	54.10	108
Zr	759	879	389	349	67	232	845	786	251	2050
Nb	N.D.	N.D.	615	N.D.	9.20	7.60	26.30	21.20	18	93
Mo	36	10	9	6	< 2	< 2	< 2	< 2	< 2	< 2
Ag	6.50	7.50	3.50	3.70	0.60	1.80	6	5.90	1.80	14.90
In	0.30	0.20	0.20	0.30	< 0.1	< 0.1	< 0.1	< 0.1	< 0.1	< 0.1
Sn	26	23	11	15	< 1	2	3	5	3	1
Sb	0.50	< 0.2	< 0.2	< 0.2	< 0.2	0.40	< 0.2	< 0.2	< 0.2	< 0.2
Cs	< 0.1	0.20	0.20	< 0.1	0.40	0.20	0.30	1.50	1.00	0.10
Ba	86	202	131	94	2751	787	1278	7618	1150	1223
La	43700	15300	12800	24600	209	154	76.90	155	80.30	112
Ce	101000	35400	26000	57600	324	349	159	330	169	249
Pr	11300	4160	2900	6720	29.40	39	17.20	39.70	19.70	30.30
Nd	41900	15600	10600	25800	90.30	149	65.60	154	76.80	127
Sm	6920	2530	1900	4740	9.16	25.80	11.90	21.60	14.40	25.20
Eu	156	55.30	65.70	123	1.56	3.16	2.31	4.77	1.68	5.07
Gd	5730	1970	1770	4060	5.99	21.80	13.20	12.70	12.90	22.90
Tb	751	254	262	584	0.60	3.45	2.81	1.32	2.05	3.89
Dy	4050	1300	1580	3350	2.77	19.40	20.40	5.20	10.50	20.70
Ho	667	207	292	577	0.45	3.95	5.10	0.83	2.03	4.21
Er	1630	520	805	1400	1.21	10.80	15.90	2.07	5.25	11.60
Tm	183	55.10	98.60	165	0.14	1.61	2.52	0.25	0.70	1.77
Yb	874	270	490	839	0.74	9.88	15.90	1.45	4.12	11.00
Lu	116	36.60	65.40	110	0.10	1.63	2.78	0.21	0.60	1.93
Hf	55	33.60	23.80	37	1.70	5.70	20.50	16.70	6.20	41.90
Ta	171	68	19.60	51	4.75	2.15	2.47	1.67	3.57	5.76
W	211	362	147	146	763	336	251	202	636	301
Tl	< 0.05	0.17	0.18	0.18	0.67	0.72	0.68	1.12	0.57	0.33
Pb	139	53	128	115	35	26	25	29	21	23
Bi	0.30	< 0.1	0.20	0.20	< 0.1	< 0.1	< 0.1	< 0.1	< 0.1	< 0.1
Th	4980	1880	1930	2750	82.20	25.20	16.20	7.79	12.20	14
U	197	66	227	189	3.01	0.73	1.22	0.76	0.77	1.24

*Low major element totals in these samples are due to strong enrichment in REE and incompatible elements.

†N.D. = not determined.

§TREE = Total rare earth elements, including only lanthanides.

TABLE 1 (continued). WHOLE ROCK MAJOR AND TRACE ELEMENT GEOCHEMISTRY

	Host Rock		Various Lithologies from MRT Showing				
Sample	PH-11	PH-15	MRT-1	MRT-2	MRT-3	MRT-4	MRT-5
%							
SiO_2	54.25	62.52	43.44	55.68	63.52	54.22	44.71
Al_2O_3	12.95	17.72	4.11	15.81	18.28	13.93	16.14
Fe_2O_3(T)	11.05	8.04	23.77	9.07	1.70	10.72	12.01
MnO	0.24	0.13	0.61	0.14	0.06	0.17	0.26
MgO	4.17	2.65	5.01	0.99	0.29	4.24	0.60
CaO	5.09	2.38	15.56	4.00	1.53	5.60	7.47
Na_2O	2.61	2.86	1.26	2.87	4.37	3.69	3.91
K2O	5.01	3.11	0.30	6.76	8.21	4.00	0.62
TiO_2	0.63	0.86	1.04	0.19	0.07	1.50	0.52
P_2O_5	1.27	0.09	0.35	0.18	0.15	0.29	0.30
LOI	1.73	0.51	3.41	2.31	0.50	0.78	2.21
Total	99.00	100.90	98.84	97.99	98.66	99.16	88.74*
Nb_2O_5	N.D.	N.D.	N.D.	N.D.	N.D.	N.D.	N.D.
TREE[§]	0.32	0.03	0.99	1.74	0.15	0.02	8.10
ppm							
Sc	10	15	60	15	5	23	25
Be	6	3	10	2	5	6	5
V	54	110	95	37	7	156	101
Cr	150	100	40	< 20	< 20	130	20
Co	61	151	61	56	81	80	51
Ni	100	40	< 20	< 20	< 20	60	< 20
Cu	40	< 10	150	40	< 10	20	40
Zn	250	90	400	70	< 30	140	150
Ga	38	22	48	72	27	24	195
Ge	5.20	2.00	9.60	9.70	2.50	2.40	29.70
As	6	< 5	12	19	< 5	< 5	89
Rb	90	75	10	178	329	131	19
Sr	150	527	284	1449	1108	406	1266

TABLE 1 (continued). WHOLE ROCK MAJOR AND TRACE ELEMENT GEOCHEMISTRY

	Host Rock		Various Lithologies from MRT Showing				
Sample	PH-11	PH-15	MRT-1	MRT-2	MRT-3	MRT-4	MRT-5
Y	354	27	241	87.70	35.90	55	317.00
Zr	1020	263	80	12	10	210	20
Nb	113	13.80	72.60	6.40	15.10	25.30	3.80
Mo	< 2	< 2	8	< 2	< 2	< 2	< 2
Ag	7.30	1.80	0.70	< 0.5	< 0.5	1.40	< 0.5
In	< 0.1	< 0.1	0.20	< 0.1	< 0.1	< 0.1	0.20
Sn	8	4	7	2	< 1	5	5
Sb	< 0.2	< 0.2	< 0.2	< 0.2	0.20	< 0.2	< 0.2
Cs	0.20	0.80	0.80	5.40	11.90	5.00	0.80
Ba	591	1174	491	5633	4713	1015	476
La	671	69.40	2910	5460	427	35.90	25100
Ce	1420	138	4820	8540	744	79.60	40400
Pr	157	15.50	442	766	68.80	10.20	3600
Nd	579	58.70	1390	2250	217	44.50	10400
Sm	106	9.97	147	177.00	22.80	9.48	776
Eu	6.77	1.45	16.80	17.30	2.70	2.25	75.60
Gd	89.70	7.74	95.60	98.70	14.40	9.03	462.00
Tb	14.20	1.05	10.50	5.53	1.49	1.58	25.10
Dy	75.70	5.49	51.50	21.20	6.94	9.03	81.30
Ho	14.20	0.99	9.44	3.20	1.24	1.92	10
Er	35.30	2.54	26.50	8.02	3.64	5.47	24.70
Tm	4.90	0.31	3.55	0.98	0.51	0.88	3.18
Yb	25.90	1.80	20.10	5.20	3.47	5.70	16.30
Lu	3.81	0.30	3.10	0.80	0.63	0.98	2.80
Hf	25.50	6.10	4.20	0.60	0.30	5.50	1.30
Ta	4.91	3.90	4.97	0.95	2.42	3.30	0.92
W	190	609	136	162	319	208	196
Tl	0.38	0.42	0.77	1.15	1.95	0.77	0.22
Pb	16	17	47	31	56	22	23
Bi	< 0.1	< 0.1	0.20	0.30	0.50	< 0.1	0.30
Th	48.30	16.20	337	523	46.20	8.36	2060
U	3.88	0.86	4.13	3.49	3.90	3.46	15.80

TABLE 1. WHOLE ROCK MAJOR AND TRACE ELEMENT GEOCHEMISTRY

Sample	Ore				Syenite			Host Rock		
	PH-1	PH-2	PH-3	PH-4	PH-5	PH-6	PH-7	PH-8	PH-9	PH-10
%										
SiO_2	31.52	45.23	41.44	33.93	71.80	63.70	60.93	52.15	67.11	58.86
Al_2O_3	4.75	7.62	5.06	1.24	14.36	15.93	18.34	13.68	14.85	16.64
Fe_2O_3(T)	10.17	17.83	22.99	26.71	1.44	4.52	5.03	7.81	5.43	8.97
MnO	0.24	0.39	0.59	0.43	0.03	0.10	0.21	0.10	0.10	0.19
MgO	0.24	0.63	0.60	0.96	0.28	0.53	0.50	6.64	1.43	0.20
CaO	10.46	9.45	13.69	10.95	0.49	1.72	1.24	4.66	2.67	3.50
Na_2O	0.33	1.72	1.30	0.47	4.20	4.17	4.54	1.53	2.82	4.49
K2O	0.52	2.32	1.21	0.16	5.71	6.73	7.23	7.38	3.81	5.30
TiO_2	4.37	2.02	0.68	1.57	0.18	0.06	0.44	2.28	0.75	0.76
P_2O_5	4.84	1.85	2.00	2.58	0.03	0.08	0.03	1.78	0.23	0.16
LOI	1.42	1.44	0.36	2.40	0.24	0.70	0.82	1.43	0.07	0.00
Total	68.85*	90.5*	89.92*	81.39*	98.76	98.24	99.30	99.44	99.26	98.52
Nb_2O_5	0.54	N.D.	N.D.	0.18	N.D.	N.D.†	N.D.	N.D.	N.D.	N.D.
TREE§	21.90	7.77	5.96	13.07	0.07	0.08	0.04	0.07	0.04	0.06

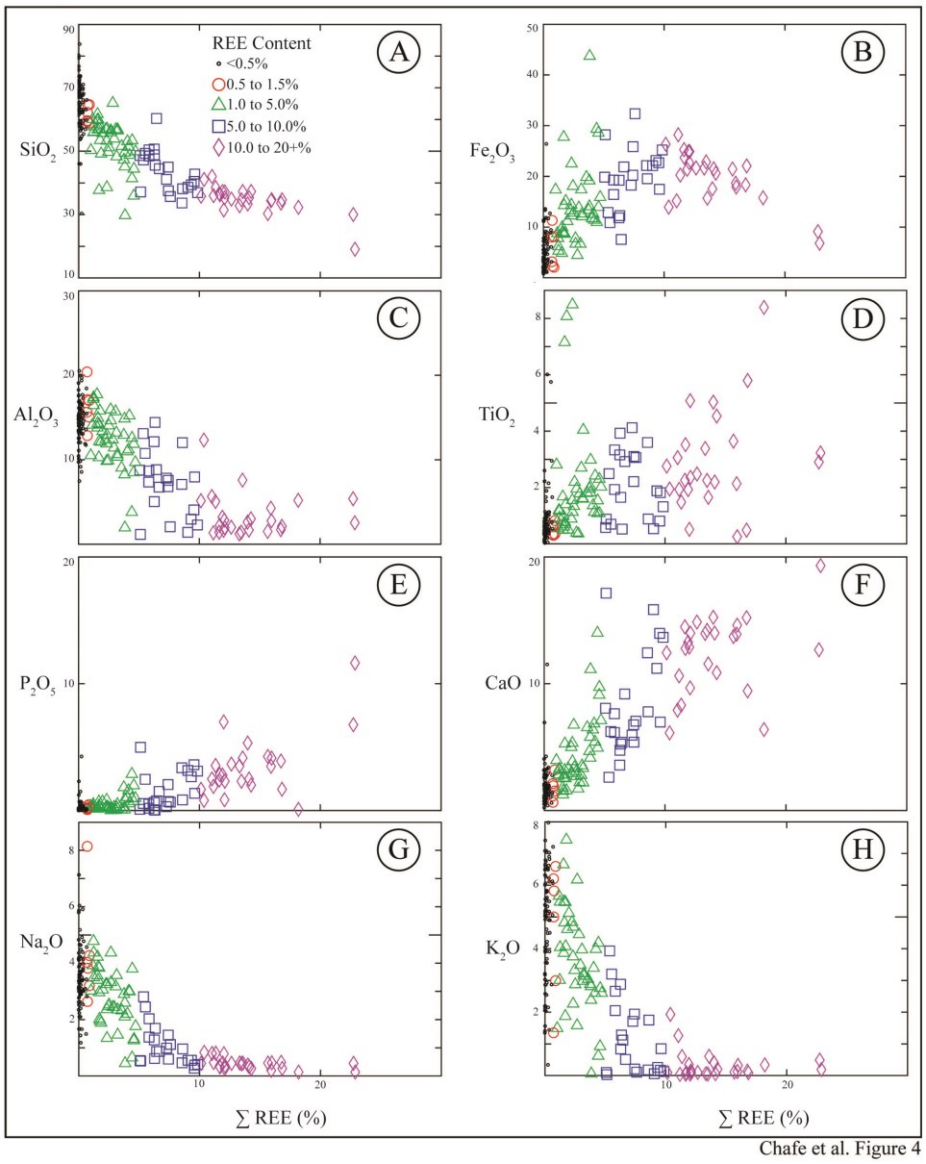

Figure 4.

Whole rock geochemistry plots showing major elements on vertical axis, plotted against TREE. Individual analyses are labeled based on REE content. Samples < 0.5% are shown as small dots, 0.5 - 1.5% as red circles, 1.0 - 5.0% as green triangles, 5.0 - 10.0% as blue squares, and 10% or > as purple diamonds. These plots show the effect of extreme REE enrichment on major element concentrations.

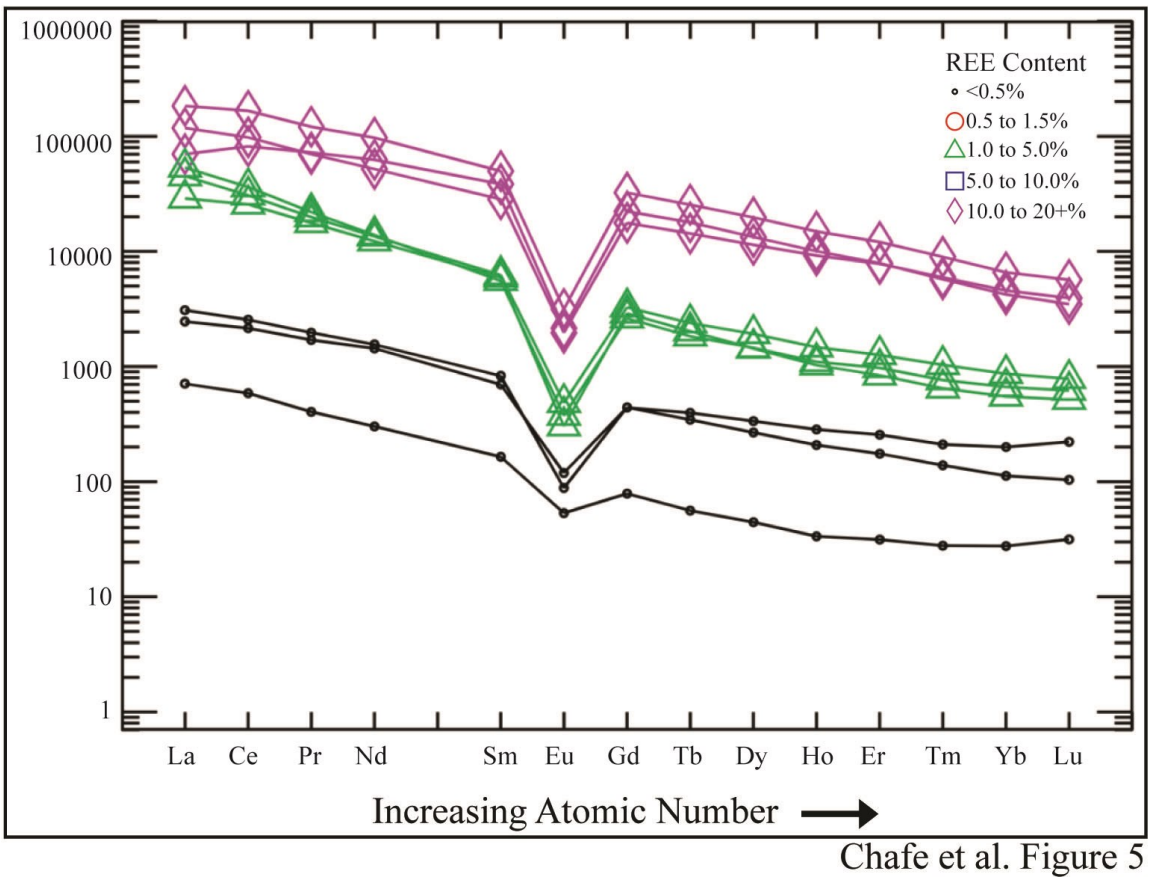

Figure 5.

Chondrite-normalized whole-rock REE spider diagram of country rock, syenitic, and ore samples from Pope's Hill based on Anders & Greevasse (1989) and analytical data (Table 1). Samples are divided into three groups based on REE content.

2.4.2 Petrography

Mineralized samples taken from Pope's Hill (Fig. 3d) are medium coarse-grained and are dominated by dark-grey to black vitreous allanite surrounding dull, earthy red grains of britholite with lesser veins of white quartz and chalky K-feldspar. Fine replacement textures in both the allanite and britholite crystals suggest alteration and replacement by secondary mineral phases. Examination of these samples in thin section

reveals that the dark vitreous allanite is in fact a mixture of highly metamict allanite and coarse-grained, deep red, subrounded, titanite. Britholite crystals are either rimmed, or completely replaced, by a symplectic mixture of apatite, britholite, monazite, quartz and carbonate with an average grain size around 100 μm. The most abundant REE mineral, allanite, appears dark grey-green, and surrounds britholite symplectite grains, and titanite. Most REE minerals are isotropic due to radiation-induced metamictization.

Accessory phases are fine-grained and occur as inclusions in the coarse-grained primary minerals. These include hornblende, biotite, garnet, and ilmenite. Zircon occurs both as fine and coarse-grained crystals, up to mm-scale in size.

Unmineralized syenite samples from Pope's Hill are far less complex pink, medium course-grained mixtures of pink alkali feldspar and white quartz with a minor concentration of dark green hornblende. The alkali feldspar is perthitic and hornblende crystals are altered by small inclusions of biotite and garnet. Trace percentage of monazite is found throughout the perthite.

2.4.3 SEM, BSE Imaging

Representative samples of REE ore and syenite, PH-1 (Fig. 6) and PH-5, respectively (Appendix 1), were reexamined by SEM in order to fully understand the coarse textures and mineral abundances of each rock type. As representative of the Pope's Hill ore, PH-1 shows the texture and modal abundance of the REE minerals (Fig. 6a). Composite thin section images of PH-1 were created using the FEI MLA software to

construct BSE (Fig. 6b) and false color, “GXMAP” images, (Fig. 6c). The PH-1 thin section is medium-grained and minerals

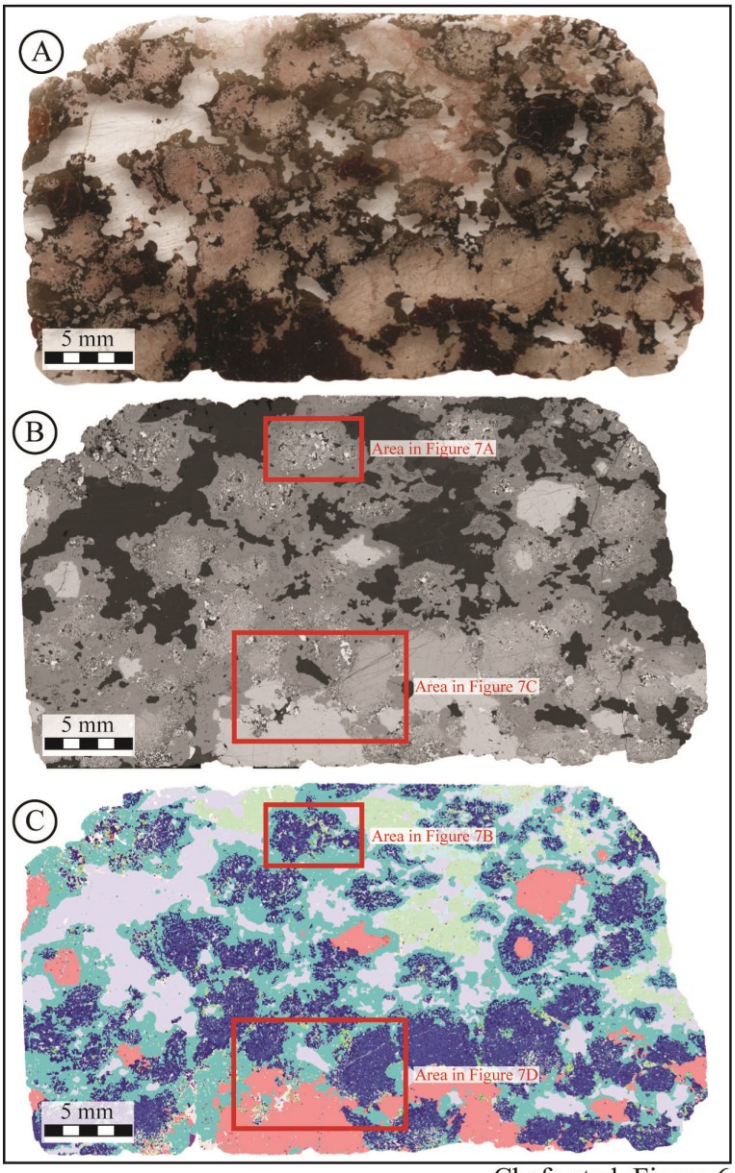

Figure 6.

Images from a thin section of representative sample of mineralization, PH-1, are presented in plain light, BSE and a false colour GXMAP produced by SEM-MLA in A, B and C, respectively. A colour legend for the GXMAP is presented in Figure 7, in which the areas outlined by red boxes are shown in detail.

appear equigranular and subhedral. The largest grains of allanite found at Pope's Hill and MRT reach over 30 mm; britholite occurs in grains up to 10 mm and monazite occurs as grains nearing 5 mm.

Detailed imaging of mineral relationship and textures (Fig. 7) was completed using the XBSE tool of the FEI MLA software. Imaging focused on britholite symplectite (mixtures of fine-grained britholite-monazite-calcite-quartz) (Fig. 7a, b) and on titanite and coarse-grained britholite (Fig. 7c, d) regions in the thin section. Replacement textures occur on many scales in mineralized samples. Small, sub-mm symplectic bands of monazite, apatite-britholite and quartz-carbonate form around allanite and titanite-(Ce). A similar mixture of medium to coarse-grained monazite, quartz-carbonate, REE carbonates, and fine-grained apatite-britholite partially to fully replace coarse britholite. Allanite is the most dominant REE mineral throughout the occurrence. In some areas, allanite is very coarse grained and euhedral, with crystals are observed up to centimeters in size (Fig. 3b). Where mineralization is strongest, allanite is subhedral to anhedral, surrounding all REE minerals. In all cases, allanite is vitreous (glassy) and metamict. Titanite-(Ce) has REE-depleted rims that are closely associated with symplectic bands of monazite and quartz, or grain boundaries with britholite symplectite, (Fig. 8). Large grains (>5 mm) of both allanite and titanite-(Ce) can contain cores with inclusions of fergusonite, ilmenite, galena, stoichiometric titanite, in addition to separate crystals of allanite and titanite-(Ce) (these textures are shown in plane light in Fig. 6a).

Scanning electron microscope BSE imaging of zircon grains from crushed sample grain separates was used to examine intra-grain chemical variations and guide future LA-

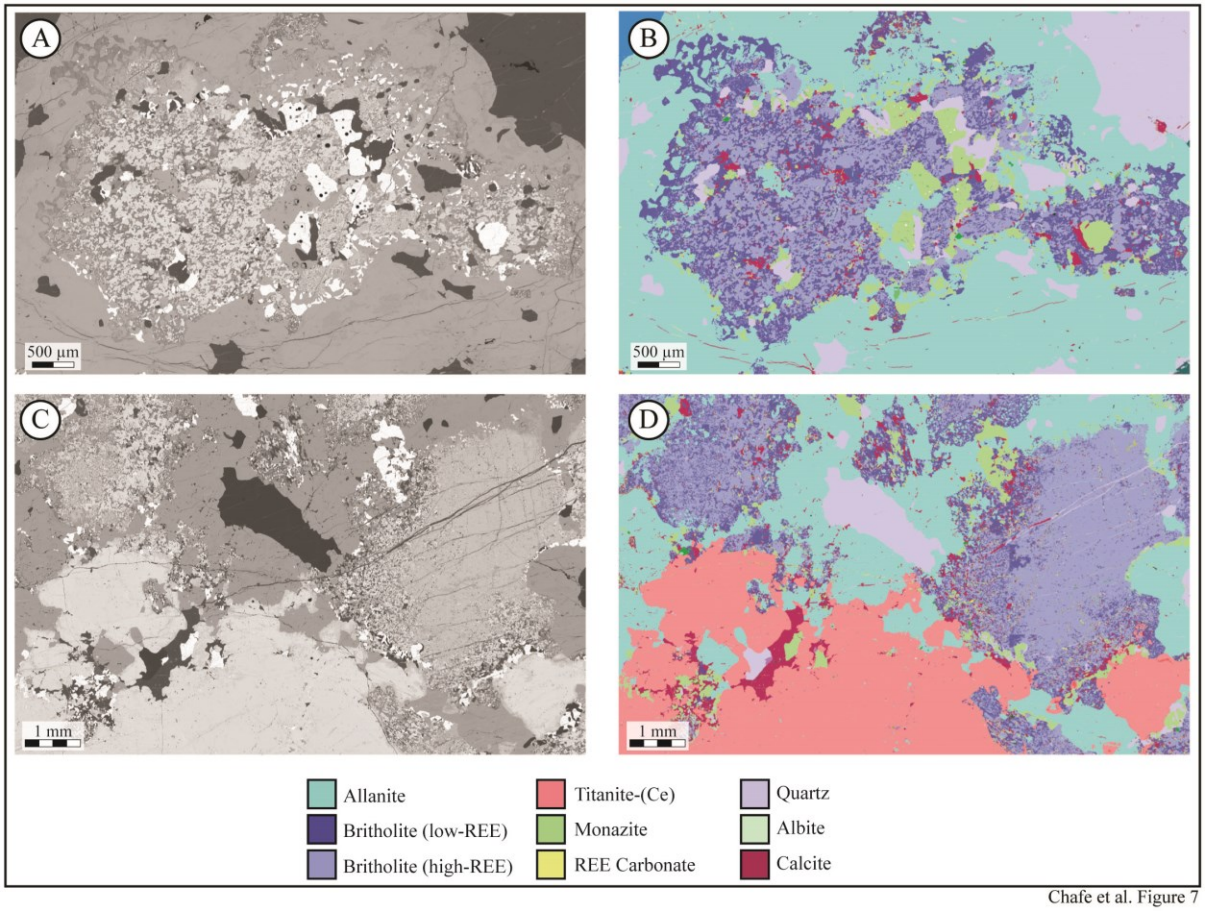

Figure 7.

Detailed BSE (left) and false colour images (right) generated by XBSE using SEM-MLA. Each area is highlighted in Figure 6B and 6C. A. mixture of fine- and coarse-grained minerals in an allanite crystal with varying BSE emissions. B. False color image of image A, showing a mixture of fine-grained apatite-britholite, monazite, allanite, quartz, and calcite in larger allanite grain. C. Interface between Titanite-(Ce), lower-left, allanite and britholite-rich mixture. D. False color image of C, showing both a homogenous britholite grain and britholite-rich aggregate grains.

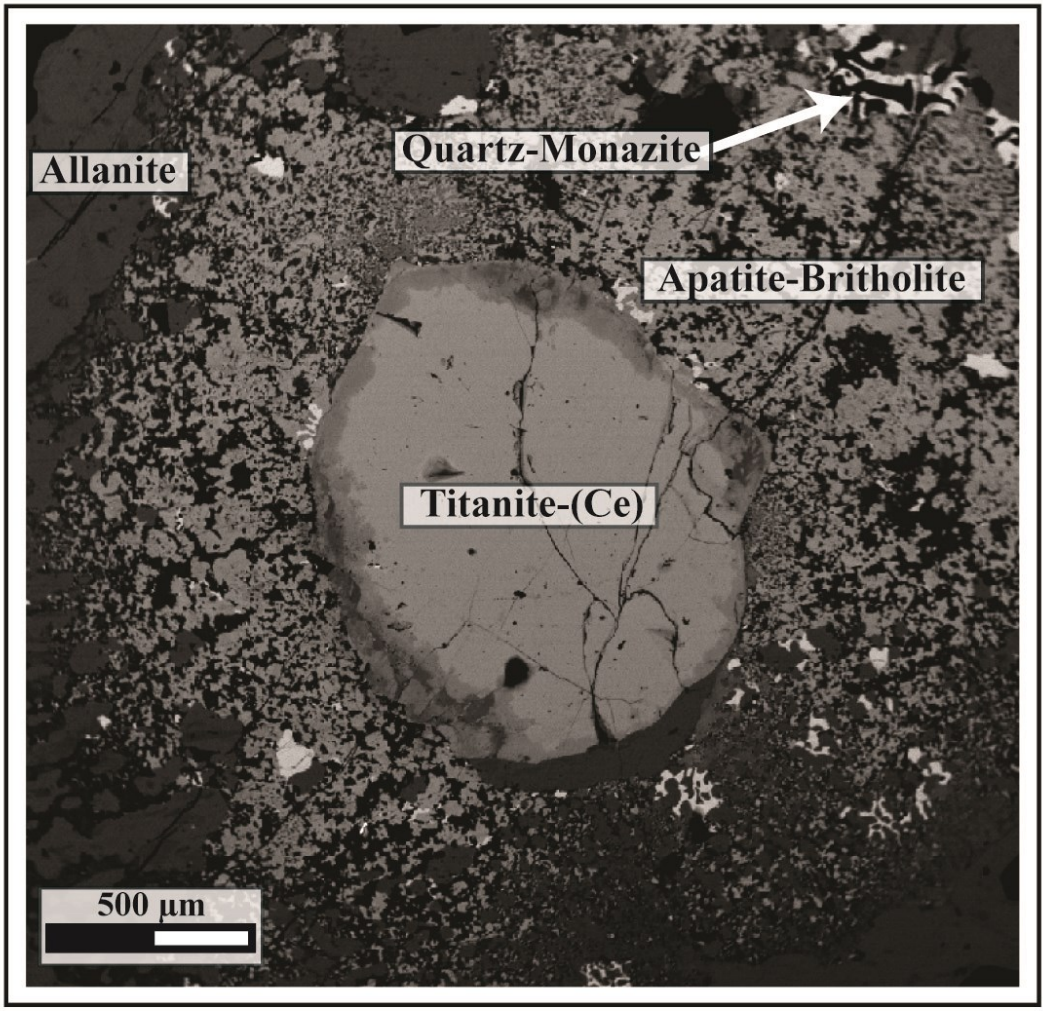

Chafe et al. Figure 8

Figure 8.

Titanite-(Ce) crystal shown in BSE with depleted rims interfacing with britholite-rich aggregate grains. Monazite-quartz symplectite is shown in the top right corner.

ICPMS work. Zircon from the ore sample, PH-1, appear relatively homogenous in BSE, however, many crystals are fractured and broken along sharp angular edges (Fig. 9f). Since most minerals in the ore samples are coarse grained, it is likely that these zircon grains were originally large crystals, >500 micrometers, and were broken during the crushing process; additional analyses were completed on thin sections for this reason.

Zircon from the syenitic sample, PH-5, are euhedral and ~200 μm in length. In BSE images, however, the samples are clearly altered, exhibiting dark areas in sharp contact with bright areas (Fig. 9d). Complex zonation is observed alternating between bright and dark discontinuous layers in BSE images. This zonation may indicate hydrothermal alteration (Schaltegger, 2007 and references therein). Neither bright, nor dark zircon is limited to the rim or the core; both occur throughout entire crystals. Cracking, however, is limited to the rim of these zircon grains, indicating either swelling of the zircon core, or fluid pathways from accumulated radiation damage.

Zircon from the country rock sample, PH-10, is much less complex. They are sub- to euhedral and sized 100-200 μm. In BSE, they show turbidity in the form of slight variation between dark and bright regions that are in gradual, diffused contact (Fig 9b). Both phases appear to be of similar chemistry and – as will be shown in later sections – age.

Monazite grains from PH-1 were imaged by BSE (Fig. 9a, c, and e). Zoning is observed where darker layers, surround bright, turbulent cores, which are both rimmed by slightly lighter monazite. The grains range from 100 to 200 μm, and therefore represent monazite in allanite and britholite symplectite. The very fine-grained monazite observed with quartz reacting surrounding titanite-(Ce) and allanite (Fig. 8) may be dissimilar.

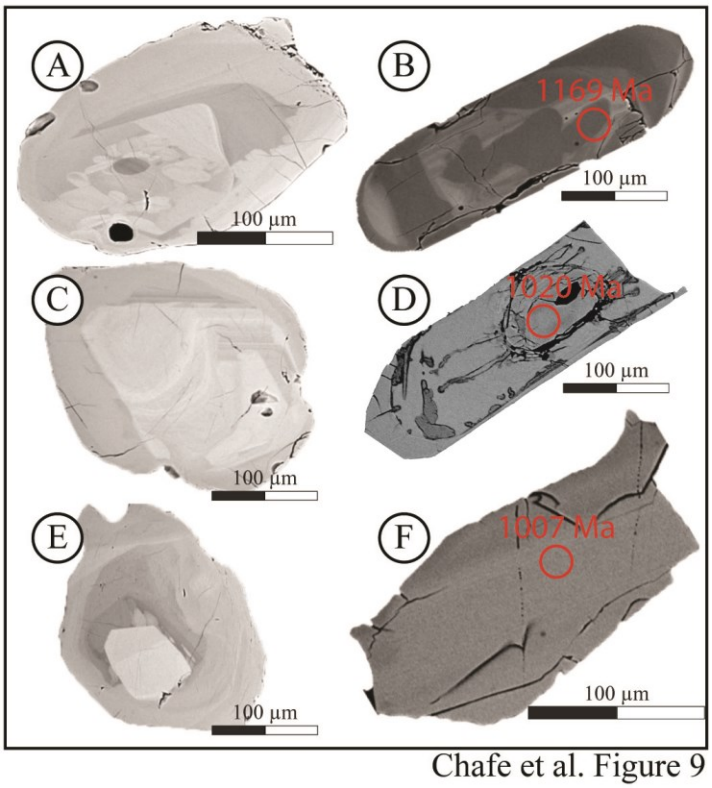

Figure 9.

BSE images of representative monazite (left) and zircon (right) grains from samples PH-1, PH-5, and PH-10 analyzed by ID-TIMS. All monazite, A, C, and D, are from syenitic sample PH-5 and represent those analyzed by ID-TIMS. Zircon from country rock sample PH-10, syenitic sample PH-5, and ore sample PH-1 are B, D, and F, respectively. These grains were analyzed by LA-ICPMS with laser spots and $^{206}Pb/^{238}U$ ages shown in red.

2.4.4 EPMA

Twelve thin sections from Pope's Hill and MRT underwent EPMA analysis to further characterize the REE minerals, textures, and their relationships. Mineral chemistries are presented using an average of WDS results (Tables 2 and 3). A remarkably wide variety of minerals were identified including 9 REE minerals, 4 major and 5 minor, that host the extreme REE enrichment. Element schedules and detection

limits did not allow for measurement of all REE and in some cases other major and minor elements by EPMA, however the total REE_2O_3 concentrations (Table 2) differ only slightly from complete REE totals acquired during later LA-ICPMS work. Gangue minerals were also examined for comparison (Table 3).

Yttrium has been excluded from the definition of "REE" used here, since it behaves contradictory to REE concentrations in titanite-(Ce), allanite, monazite and REE carbonate. Only in apatite-britholite does yttrium concentration increase with REE.

Significant intra-mineral compositional variations noted in the mineralization at Pope's Hill. Specifically, analyses of apatite-britholite vary from stoichiometric apatite to britholite with up to, 46.5 wt% REE oxides. Apatite-britholite analyses have been divided into three groups in order to show the continuum of compositions (Table 2): 1) "apatite" representing stoichiometric apatite with less than 5 wt% REE_2O_3; 2) "britholite-

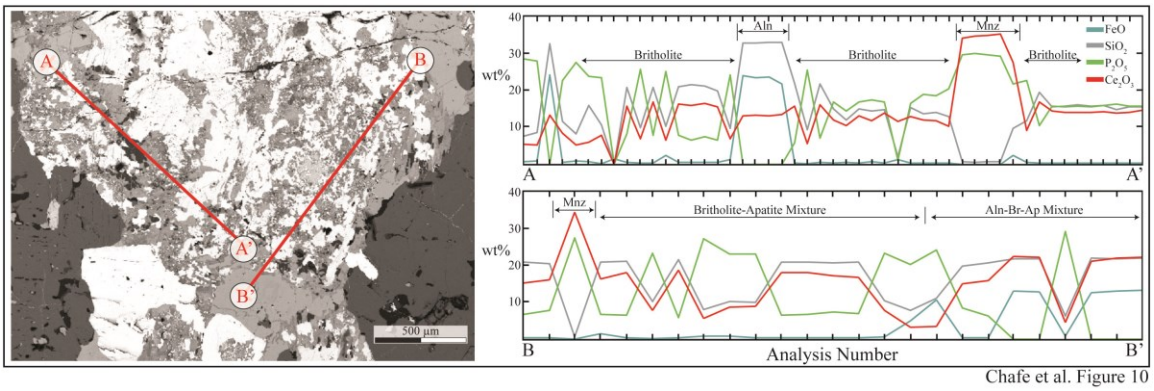

Figure 10.

Two multi-point EPMA traverses across britholite aggregate grain (left) from sample PH-2. The grains variable composition is shown on the right where FeO, SiO_2, P_2O_5, and Ce_2O_3 are plotted in wt%. Areas of increased in FeO and P_2O_5 and darker BSE emissions are analyses of allanite. Areas of increased Ce_2O_3 and P_2O_5 and very bright BSE emissions are analyses of monazite. Areas of moderate BSE emission correlate with variable, mid-range concentrations of Ce_2O_3, P_2O_5, and SiO_2, indicating analyses of britholite.

TABLE 2. AVERAGE ELECTRON MICROPROBE MINERAL GEOCHEMISTRY

Element Oxides	Titanite	Titanite(-Ce)	Allanite	Fergusonite	Monazite
	$CaTiSiO_4$	$(Ca,REE)(Ti,Fe)(SiO_4)O$	$(Ca,REE)_2(Al,Fe)_3(SiO4)_3OH$	$(Ce,La,Y)NbO_4$	$(Ce,La,Nd,Th)PO_4$
wt%					
SiO_2	30.58	21.22	33.30	1.77	2.11
Al_2O_3	3.07	1.21	11.48	0.05	N.D.
FeO	4.66	11.28	17.77	1.46	0.16
MnO	0.22	0.15	0.52	0.13	0.00
CaO	27.31	3.23	10.69	2.44	0.69
Na_2O	0.03	0.01	0.15	0.05	0.00
TiO_2	30.29	15.39	1.48	0.39	N.D.
P_2O_5	N.D.*	N.D.	N.D.	N.D.	27.17
La_2O_3	0.14	11.20	6.14	0.48	20.04
Ce_2O_3	0.39	17.24	9.84	2.45	29.45
Pr_2O_3	0.07	1.71	0.82	0.04	N.D.
Nd_2O_3	0.31	6.70	3.00	4.91	8.47
Sm_2O_3	0.01	0.03	0.00	2.34	0.78
Eu_2O_3	0.00	0.00	0.00	5.21	0.10
Gd_2O_3	0.14	0.44	0.17	0.47	0.29
Dy_2O_3	0.09	0.20	0.04	5.17	0.14
Yb_2O_3	0.04	0.09	0.03	1.57	0.02
Y_2O_3	0.40	0.84	0.28	17.61	0.38
UO_2	0.00	0.04	0.03	1.10	0.27
ThO_2	0.02	1.18	0.32	3.56	6.26
Ta_2O_5	0.12	0.17	0.09	0.06	N.D.
Nb_2O_5	2.92	3.19	0.71	45.51	N.D.
ZrO_2	0.04	0.21	0.01	0.00	N.D.
BaO	0.54	0.30	0.04	0.02	0.02
SrO	0.00	0.00	0.01	0.00	0.05
PbO	0.03	0.09	0.08	0.73	0.30
As_2O_5	0.01	0.02	0.01	0.00	0.02
SO_3	N.D.	N.D.	N.D.	N.D.	0.76
Cl	0.00	0.04	0.18	0.21	0.02
F	0.18	0.00	0.00	0.38	0.41
Total	101.54	95.83	96.01	98.14	97.76
Total REE Oxide	1.19	37.62	20.03	22.66	59.31

Data represent an average of all EPMA analyses taken on each mineral from Pope's Hill (PH-*n*) samples.

*N.D. = not determined, most analyses used to calculate the average are below detection limit

†The average grain size of REE-carbonate is less than 10µm, which was the size of the electron beam.

Results are often contaminated by other phases containing elements not accounted for in the analysis schedule.

TABLE 2 (continued). ELECTRON MICROPROBE MINERAL GEOCHEMISTRY

Element Oxides	Apatite	Britholite-(Ce)	Britholite-(high REE)	REE Carbonate
	$Ca5(PO_4)3F$	$(REE,Ca)_5(SiO_4,PO_4)_3(OH,F)$	$(REE,Ca)_5(SiO_4,PO_4)_3(OH,F)$	$REE_2Ca(CO_3)3F_2$
wt%				
SiO_2	0.99	2.92	12.79	9.35
Al_2O_3	N.D.	N.D.	N.D.	N.D.
FeO	0.37	1.32	1.25	5.64
MnO	0.06	0.06	0.09	0.05
CaO	54.44	47.14	25.50	2.79
Na_2O	0.07	0.08	0.05	0.02
TiO_2	N.D.	N.D.	N.D.	N.D.
P_2O_5	39.27	34.95	18.67	0.24
La_2O_3	0.25	1.00	3.59	15.08
Ce_2O_3	0.69	2.71	10.18	25.43
Pr_2O_3	N.D.	N.D.	N.D.	N.D.
Nd_2O_3	0.48	1.63	5.69	11.69
Sm_2O_3	0.13	0.36	1.20	0.68
Eu_2O_3	0.04	0.05	0.14	0.00
Gd_2O_3	0.21	0.64	1.66	0.74
Dy_2O_3	0.14	0.47	1.41	0.19
Yb_2O_3	0.05	0.09	0.36	0.03
Y_2O_3	0.68	2.12	7.72	0.01
UO_2	0.01	0.03	0.16	1.00
ThO_2	0.01	0.10	0.65	0.00
Ta_2O_5	N.D.	N.D.	N.D.	N.D.
Nb_2O_5	N.D.	N.D.	N.D.	N.D.
ZrO_2	N.D.	N.D.	N.D.	N.D.
BaO	0.01	0.01	0.03	0.06
SrO	0.04	0.04	0.04	0.01
PbO	0.01	0.05	0.20	0.03
As_2O_5	0.00	0.01	0.00	0.01
SO_3	0.08	0.39	0.91	0.11
Cl	0.05	0.08	0.15	0.09
F	3.46	2.77	1.53	2.11
Total	100.07	97.84	93.27	74.45[†]
Total REE Oxide	2.52	8.61	30.54	53.84

Table 2

TABLE 3: ELECTRON MICROPROBE HOST MINERAL CHEMISTRY

Element Oxides	Albite	K-Feldspar	Pyroxene	Hornblende
wt%				
SiO_2	67.13	64.22	50.56	43.04
Al_2O_3	20.17	18.64	1.02	8.59
FeO	0.32	0.16	22.19	30.09
MnO	0.02	0.01	0.85	0.52
MgO	0.03	0.01	5.38	3.56
CaO	0.59	0.03	19.02	10.53
Na_2O	11.10	1.02	1.05	1.34
K_2O	0.22	15.60	0.02	1.05
TiO_2	0.02	0.02	0.08	0.59
Rb_2O	0.07	0.05	N.D.*	N.D.
SrO	0.13	0.03	N.D.	N.D.
BaO	0.01	0.30	0.01	0.01
Total	99.80	100.10	100.18	99.32

*N.D. = not determined

(Ce)" representing between 5 and 15 wt% REE_2O_3; and 3) "britholite-(high REE)" representing analyses above 15 wt%. Two EPMA traverses across britholite grains in ore sample PH-2 (Fig. 10, lines A and B) show inclusions of allanite, causing spikes in FeO and SiO_2, and correlating with darker grains in BSE. Monazite causes spikes in Ce_2O_3 and P_2O_5 and correlate with bright grains in BSE. The presence of these minerals indicates "britholite symplectite" is in fact aggregates of a variety of minerals, more than a symplectic solid solution of apatite-britholite, and they will be referred to as britholite aggregate grains for the remainder of this paper.

The deep red, high relief mineral (Fig. 6, 7 colored pink, and 8) mentioned above is compositionally similar to titanite, consisting primarily of REE, Fe_2O_3, TiO_2, and SiO_2 with minor CaO and Nb_2O_5 (Table 2). This new, REE-rich titanite end-member, called here, "titanite-(Ce)" appears to represent a previously unknown (to the authors of this paper) REE-enriched titanite structure where Fe^{3+}+REE are involved with a coupled substitution with Ca+Ti (Fig 11a). In similar fashion to the apatite-britholite, titanite is divided into "titanite" and "titanite-(Ce)"; for the stoichiometric, <3 wt% REE_2O_3, titanite; and Fe^{3+}+REE enriched phases, up to 43 wt% REE_2O_3, respectively.

At MRT, the mineralogy is less complex. Extreme LREE-enrichment in mineralized samples relative to the host rock confirm petrographic observations, showing that only allanite and apatite host REE mineralization, causing the. The amount of REE concentrated in each mineral is generally lower than at the Pope's Hill Occurrence. At MRT allanite contains ~14.0 wt% REE and apatite ~2.5 wt%.

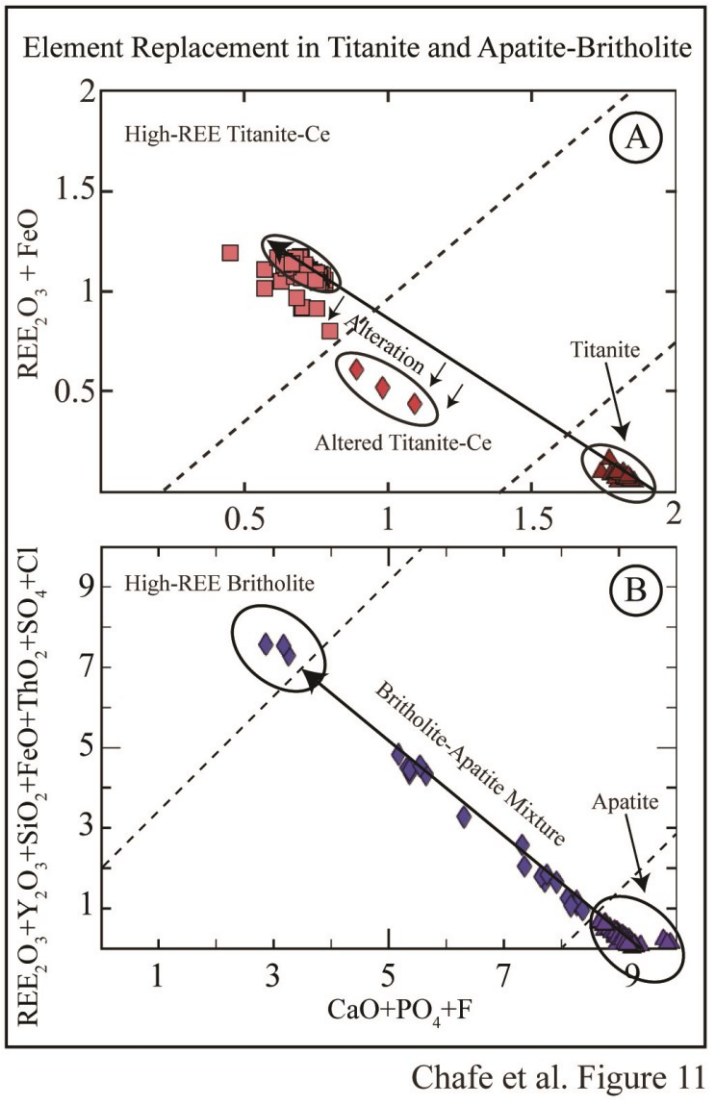

Figure 11.

The continuum of chemistries observed in titanite-(Ce) (top) and apatite-britholite (bottom). Mixing lines for each solid solution are plotted. A. Stoichiometric titanite, lacking REE, plots on the bottom of the mixing line and strongly enriched titanite-(Ce) at the top. Analyses from rims of depleted titanite-(Ce), Figure 8, plot below the mixing line, likely due to alteration. B. Stoichiometric apatite plot on the bottom of the mixing line with strongly enriched "high-REE britholite" at the top. All analyses plot along the mixing line, conforming to the substitution of REE and Si for Ca and P in apatite structure.

2.4.4.1 Allanite

Allanite composition varies and is dependent on the location where it was collected. At Pope's Hill, allanite contains on average 24.1 wt% REE_2O_3 and at MRT, 14.0 wt%. Compensating for this difference are Ca and Al, depleted at Pope's Hill and enriched at MRT. Both varieties contain trace amounts of Ti and as REE concentration increases so does Fe and Ti, while Th decreases.

2.4.4.2 Titanite

Stoichiometric titanite is present throughout the entire region. Samples from Pope's Hill tend to average <1 wt% REE_2O_3, with a single analysis from sample PH-13 at 2.9 wt%. Analyses on sample MRT-1 indicate an elevated REE concentration ranging from 1.6 to 3.8 wt % REE_2O_3. Both samples contain trace amounts of Fe and Al.

2.4.4.3 Titanite-(Ce)

This new, REE-enriched titanite end-member is only found at Pope's Hill and a titanite with similar composition could not be found in the literature research. On average Titanite-(Ce) contains 37.6 wt% REE_2O_3, to a maximum of 42.5 wt %. REE are accommodated into a titanite-like composition by incorporation of Fe in a major percentage accompanied by a trace amount of Nb, Th and Y. While Al commonly participates in coupled substitutions with REE, titanite-(Ce) contains only a negligible

concentration of Al (Hughes et al. 1997). The range of titanite-(Ce) compositions, lie on a mixing line between the composition of stoichiometric titanite and titanite-(Ce) (Fig. 11a). A small percentage of titanite-(Ce) grains show REE depletion in the rim of grains located at interfaces with britholite aggregate grains.

2.4.4.4 Monazite

Monazite is present in two distinct compositions. In and surrounding the ore, monazite is close to stoichiometric containing, on average, 62.4 wt% REE_2O_3 and 2.4 wt% ThO_2. Ore samples, PH-3 and PH-5 also contain monazite that is relatively enriched in Pb, Si, S, and Th.

2.4.4.5 Apatite

Present in significant abundance at both Pope's Hill and MRT, fluorapatite, averaging 2.5 wt% REE_2O_3, 3.5 wt% F, and <1 wt% SiO2, accounts for the vast majority of EPMA analyses.

2.4.4.6 Britholite-(Ce)

In solid solution with apatite, moderately REE and Si enriched britholite incorporates a number of trace elements. In the EPMA analyses, grains of apatite-britholite range from a minimum of 2.5 wt% REE_2O_3 and 1.0 % SiO_2, to a maximum of 46.5 wt% REE_2O_3 and 28.1 wt% SiO_2 with an average of 8.6 wt% REE_2O_3 and SiO_2, 2.9

wt%. Increasing REE and Si are accompanied by trace amounts of Al_2O_3, As_2O_5, Cl, SrO, ThO_2 and UO_2. These trace elements are accompanied by a loss of CaO, F, and P_2O_5, the essential structural components of apatite. Similar to titanite-(Ce), the compositions of apatite-britholite plot along a mixing line with between stoichiometric apatite and highly enriched britholite (Fig. 11b).

2.4.4.6 Fergusonite

While there are a number of silicates, phosphates, and carbonates at Pope's Hill, fergusonite ($YNbO_4$) is the only niobate. Present in only trace abundance, fergusonite shows consistent chemistry, with only slight variation in REE concentration. The most abundant REE in fergusonite is Nd, averaging 4.9 wt%. Overall, fergusonite averages 22.7 wt% REE_2O_3, with variance in REE content due to the direct substitution of REE^{3+} for Y^{3+}, as Nb_2O_5 remains consistent. A result of the minerals high ThO_2 and UO_2 content; 2.6 ad 1.1 wt%, respectively, fergusonite in sample PH-2 is highly metamict and exhibits radiation swelling, where cracks fan out from the fergusonite grains through surrounding allanite and titanite-(Ce).

2.4.4.7 REE-carbonate

REE-carbonate at Pope's Hill is not well characterized. It exists in grains too small for EPMA or LA-ICPMS, often interstitial filling micron-scale cracks. REE-carbonate chemistry will not be examined in-depth in later sections, however, their presence at Pope's Hill and MRT is important to note as it adds to the wide variety of

REE minerals from different REE-ligand complexes coexist in the rock units of the Pope's Hill region.

2.4.4.8 K-Feldspar

As typical of syenite, the most abundant mineral in syenite from the Pope's Hill area is the K-feldspar, orthoclase. It is nearly stoichiometric, containing ~0.3 wt% BaO as the only significant trace element (Table 3). Centimeter-scale grains show metasomatic alteration and albite replacement.

2.4.4.9 Albite

Both alkali-feldspar phases are mutually exclusive, occurring as perthite. The scale of albite lamellae varies from sub-micron up to ~100 μm. Albite is also stoichiometric containing ~0.6 wt% CaO as the only trace element.

2.4.4.10 Pyroxene

Throughout ore samples, near end-member hedenbergite is the primary pyroxene phase. MgO content varies from 0.7 to 11 wt%, averaging 4.6 wt% trace Al_2O_3 present in many analyses. In syenitic sample PH-5, clinopyroxene contains near equal amounts of MgO and FeO, each ~11 wt%. The only trace element in all pyroxene varieties is sodium, averaging around 1 wt% NaO.

2.4.4.11 Amphibole

All amphibole analysis were of hornblende containing a minor percentage of Na_2O, K_2O, MgO and TiO_2 in addition to its essential structural components, FeO, SiO_2, CaO and Al_2O_3. They are limited to PH-6, PH-7, and PH-11 samples taken from host rock directly adjacent to mineralization and in all MRT samples. Mafic phases outside of the mineralized zone are solely pyroxene.

2.4.4.12 Quartz and Calcite

Found throughout all rock samples from all groups, quartz and calcite chemistries are typical and stoichiometric. In ore samples, both are found in close association with REE phosphate and carbonate minerals.

2.4.4.13 Trace Minerals

EDS observations identified small amounts of fine-grained, <<1 mm, ilmenite, galena, xenotime, and thorite located at grain boundaries of REE minerals at Pope's Hill. At MRT, pyrite is the only other trace mineral in addition to those mentioned.

Table 4

TABLE 4. REE CONTRIBUTION BY MINERAL

Mineral	Mineral Abundance (Whole Rock) (volume %)	Average REE_2O_3 (wt%)	Mineral REE_2O_3 (wt%)	Mineral Contribution to REE_2O_3 Budget* (%)
Allanite	41.71	20.03	8.35	47.64
Titanite-(Ce)	11.25	37.62	4.23	24.13
Monazite	4.95	59.31	2.94	16.74
Britholite-(Hi REE)	3.43	46.36	1.59	9.07
Britholite-(Ce)	4.12	8.61	0.35	2.02
Fergusonite	0.16	22.66	0.04	0.21
REE carbonate	0.05	53.84	0.03	0.15
Apatite	0.28	2.50	0.01	0.04
Titanite	0.01	1.19	0.00	0.00
Total	65.96	N.A.	17.54	100.00

*Calculated by constructing a "REE budget" based on the EPMA determined chemistry and SEM-MLA determined abundance of each mineral phase.

N.A. = Not applicable.

2.4.5 SEM-MLA

False color images generated by the SEM-MLA software (Fig. 6c) represent a digitized map of every grain, of every mineral in sample PH-1. The MLA software has assigned an ID to every pixel in the image, giving each mineral a unique colour. The user assigns a mineral name to false-colour crystal and the computer uses the minerals density to calculate the abundance, weight percent, of each phase. Combining these abundances with the quantitative EPMA results (Table 2) we are able to construct the whole rock "REE budget" (Table 4). This simple calculation multiplies mineral abundance by its average weight percent REE_2O_3 to create a whole rock REE_2O_3 concentration. It then divides each phase's contribution to total REE_2O_3 by the whole rock value, yielding the contribution of each mineral toward the total REE budget of the sample. The result shows that allanite contributes 48%, titanite-(Ce) contributes 24%, monazite contributes 17%, britholite contributes 11%, fergusonite contribute 0.2%, apatite contributes 0.04% and stoichiometric titanite has no significant contribution (Table 4). Quartz, calcite, feldspar, pyroxene, amphibole, mica, zircon, ilmenite, rutile, sulphides do not contribute to the REE budget.

2.4.6 XRD

Both experimental and analytical issues hindered identification of some minerals in samples from Pope's Hill. While the existing XRD spectrum databases are extensive, they do not contain the range of data on apatite-britholite, titanite and allanite necessary to identify the diverse chemistry and hence, variation in the unit cell that will affect XRD

peaks. For example, since only a fraction of Pope's Hill britholite may conform to the existing diffraction data for britholite, only a small amount can be identified (XRD spectra in Appendix 1).

All REE ore samples show a small number of low intensity peaks that often correlate with host rock minerals, orthoclase, albite and quartz. The absence of XRD peaks for abundant mineral phases, allanite, apatite and monazite, in place of amorphous material between 21˚ and 36˚ 2θ is indicative of complete destruction of the crystal structure by metamictization. The amorphous phase, or phases, occupies the space where the primary peaks for titanite, allanite and all other observed mineral phases lie making definitive mineral identification impossible.

2.4.7 LA-ICPMS, Trace Elements

The trace element composition of each mineral has been measured by LA-ICPMS. These data have been used to create REE chondrite-normalized diagrams (Fig. 12) using chondrite compositions from Anders and Greevasse (1989). In general, the minerals analyzed resemble the trends of the whole rock analyses, they are highly LREE-enriched and have a pronounced Eu-depletion. In allanite, monazite, titanite-(Ce) and some britholite analyses, La is over 2 orders of magnitude higher than Lu. The britholite analyses are suspect as individual grains of britholite are very fine-grained, existing within britholite symplectite (Fig. 7, 10an therefore, the laser spot size often exceeds grain size.

2.4.8 LA-ICPMS, U-Pb Ages

Zircon from all three rock groupings, country rock, syenite and mineralization were dated by LA-ICPMS (Table 5). To supplement zircon dating, monazite was analyzed for U-Pb age simultaneously with Sm-Nd isotope composition, presented below (Table 6).

2.4.8.1 Country Rock Zircon

Twenty analyses of sample PH-10, show a spread in $^{206}Pb/^{238}U$ dates from ~1210 to 1040 Ma, excluding a single outlier with a date of 1004 Ma. While BSE images show faint zonation (Fig. 9a, c, e), clear core and rim domains are typically difficult to determine. The two oldest dates of ~1210 and 1200 Ma, appear to be from distinct core regions and are considered to represent an inherited ~1200 Ma component (Fig. 13a, c; Z1). Nine analyses from relatively unzoned grains yield a weighted mean $^{206}Pb/^{238}U$ age of 1099 ± 11 Ma (MSWD = 1.0) (Fig. 13a, c; Z2), which we interpret to be the age of crystallization of the country rock. The four youngest dates overlap and give a weighted mean $^{206}Pb/^{238}U$ age of 1047 ± 12 Ma (MSDW = 0.6), which we interpret to represent a metamorphic age. Five analyses have intermediate ages, and likely represent either domains which underwent Pb loss at ~1050 Ma or have resulted from analytical mixing during laser sampling.

2.4.8.2 Syenite Zircon

Intricate zoning of the syenitic samples from PH-5 (Fig. 9d), give two dates; a limited sampling of zircon cores (n=3) yield a weighted mean $^{206}Pb/^{238}U$ age of 1069 ± 13 Ma (MSWD = 0.1), slightly younger than the country rock, while the rim yielded a

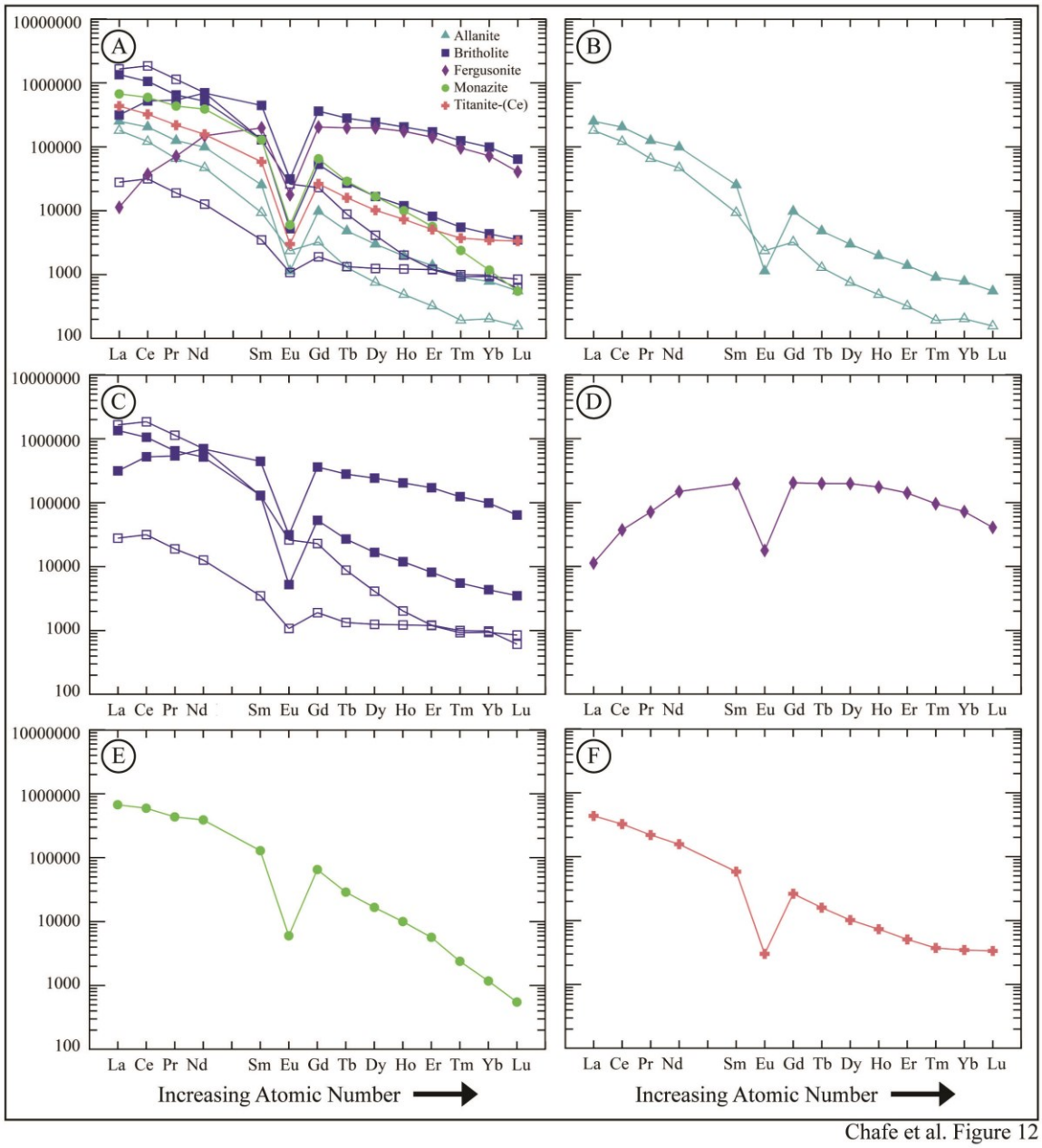

Figure 12.

Chondrite-normalized mineral spider diagram showing single representative analyses of REE enrichment patterns based on Anders & Greevasse (1989), using data obtained by LA-ICPMS. Solid points are analyses from Pope's Hill and open points from MRT. A. all analyses together. B. allanite. C. apatite-britholite. D. fergusonite. E. monazite. F. titanite-(Ce).

Table 5

TABLE 5: LA-ICPMS ZIRCON U-Pb RESULTS

Grain & Analysis No.	Measured Values					Calculated Ages			
	$^{207}Pb/^{235}U$	2σ Error (abs.)*	$^{206}Pb/^{238}U$	2σ Error (abs.)	RHO	$^{206}Pb/^{238}U$ Age (Ma)	2σ Error (abs.)	$^{207}Pb/^{235}U$ Age (Ma)	2σ Error (abs.)
Ore Rock, PH-1:									
A1	1.801	0.050	0.1731	0.0038	0.1603	1031	21	1048	18
A2	1.634	0.053	0.1675	0.0037	0.1579	999	21	979	20
A3_Rim	1.755	0.052	0.1734	0.0039	0.1815	1031	22	1030	19
A3_Core	1.944	0.051	0.1840	0.0042	0.2980	1088	23	1096	17
B1	1.843	0.057	0.1719	0.0040	0.1404	1023	22	1063	21
B2	1.688	0.047	0.1650	0.0036	0.1841	985	20	1003	18
C2	1.834	0.058	0.1764	0.0040	0.1671	1048	22	1057	21
C3	1.656	0.049	0.1658	0.0036	0.2666	989	20	992	19
D1	1.717	0.058	0.1677	0.0040	0.0601	999	22	1016	22
D2	1.747	0.054	0.1681	0.0037	0.1681	1001	21	1028	19
D3	1.668	0.048	0.1706	0.0038	0.2192	1015	21	995	18
D4	1.741	0.044	0.1750	0.0037	0.2207	1040	20	1024	16

Note: Each analysis represents a singe laser ablation point on zircon grains in mineral mount from ore rock, country rock and syenite, PH-1, PH-5, and PH-10, respectively.
Data were measured using LA-ICPMS and reduced using Iolite (version 2.15) by Paton et al. (2011).
*All errors are 2 sigma and absolute.

TABLE 5 (continued): LA-ICPMS ZIRCON U-Pb RESULTS

Grain & Analysis No.	Measured Values					Calculated Ages			
	$^{207}Pb/^{235}U$	2σ Error (abs.)*	$^{206}Pb/^{238}U$	2σ Error (abs.)	RHO	$^{206}Pb/^{238}U$ Age (Ma)	2σ Error (abs.)	$^{207}Pb/^{235}U$ Age (Ma)	2σ Error (abs.)
Ore Rock, PH-1:									
E2	1.912	0.049	0.1854	0.0040	0.1661	1096	22	1085	17
E3	1.743	0.050	0.1698	0.0037	0.0744	1011	21	1023	18
E3	1.743	0.051	0.1738	0.0039	0.1416	1033	21	1025	19
E4	1.715	0.053	0.1694	0.0037	0.0890	1009	21	1012	20
E5	1.867	0.047	0.1793	0.0039	0.1986	1063	21	1069	17
F1	1.738	0.052	0.1662	0.0037	0.1595	991	21	1024	20
F2	1.733	0.054	0.1732	0.0040	0.1533	1030	22	1019	20
F3	1.684	0.051	0.1684	0.0037	0.0977	1003	20	1003	19
F4	1.653	0.049	0.1660	0.0038	0.0037	991	19	988	19
G1	1.744	0.052	0.1686	0.0037	0.1098	1004	21	1025	19
G2	1.828	0.045	0.1783	0.0038	0.1268	1058	21	1055	16
G4	1.660	0.052	0.1648	0.0037	0.0338	983	21	990	20
G5	1.664	0.047	0.1669	0.0037	0.1545	995	20	994	18
H1	1.584	0.044	0.1625	0.0036	0.0264	971	20	963	18
H3	1.647	0.057	0.1661	0.0038	0.1601	990	21	982	22
I3	1.713	0.042	0.1690	0.0036	0.1332	1007	20	1012	16
I4	1.690	0.047	0.1678	0.0037	0.1491	1000	20	1005	17
I5	1.844	0.049	0.1770	0.0039	0.2286	1051	21	1060	17
H2	1.806	0.066	0.1693	0.0040	0.0329	1008	22	1042	24
H5	1.751	0.056	0.1762	0.0040	0.0526	1046	22	1027	20
J1	1.695	0.053	0.1693	0.0038	0.1584	1009	21	1007	20
J2	1.716	0.056	0.1670	0.0039	0.0969	996	21	1016	21

TABLE 5 (continued): LA-ICPMS ZIRCON U-Pb RESULTS

Grain & Analysis No.	Measured Values					Calculated Ages			
	$^{207}Pb/^{235}U$	2σ Error (abs.)*	$^{206}Pb/^{238}U$	2σ Error (abs.)	RHO	$^{206}Pb/^{238}U$ Age (Ma)	2σ Error (abs.)	$^{207}Pb/^{235}U$ Age (Ma)	2σ Error (abs.)
Syenite, PH-5:									
A1_Rim	1.713	0.040	0.1713	0.0038	0.4946	1019	21	1013	15
A2_Core	1.939	0.051	0.1800	0.0041	0.5300	1067	23	1093	17
B1_Rim	1.974	0.051	0.1810	0.0044	0.9612	1073	23	1109	16
B2	1.847	0.066	0.1704	0.0056	0.9928	1008	27	1050	19
B3_Rim	1.793	0.044	0.1701	0.0039	0.7394	1013	21	1042	16
C2	1.927	0.050	0.1802	0.0041	0.7150	1068	23	1090	17
C3	1.707	0.041	0.1681	0.0038	0.6494	1002	21	1011	15
C4_Rim	1.761	0.041	0.1714	0.0038	0.7613	1020	21	1031	15
D1	1.703	0.040	0.1696	0.0037	0.4686	1010	20	1010	15
D3	1.768	0.042	0.1755	0.0039	0.6078	1043	21	1034	15
D4_Rim	1.614	0.038	0.1656	0.0036	0.5570	988	20	975	15

TABLE 5 (continued): LA-ICPMS ZIRCON U-Pb RESULTS

Grain & Analysis No.	Measured Values					Calculated Ages			
	$^{207}Pb/^{235}U$	2σ Error (abs.)*	$^{206}Pb/^{238}U$	2σ Error (abs.)	RHO	$^{206}Pb/^{238}U$ Age (Ma)	2σ Error (abs.)	$^{207}Pb/^{235}U$ Age (Ma)	2σ Error (abs.)
Country Rock, PH-10:									
A1	2.172	0.065	0.1963	0.0045	0.2623	1155	25	1171	21
A2	1.822	0.059	0.1750	0.0041	0.0784	1040	23	1054	21
A3	2.206	0.072	0.1999	0.0049	0.2079	1175	26	1184	23
A4	1.992	0.091	0.1877	0.0051	0.0752	1109	28	1111	31
B1	2.123	0.077	0.1938	0.0046	0.2139	1142	25	1163	25
B2	1.817	0.054	0.1763	0.0041	0.1817	1047	22	1049	20
B3	2.298	0.090	0.2042	0.0051	0.0987	1198	27	1205	27
C1	2.292	0.069	0.2069	0.0048	0.5742	1212	26	1207	21
C2	1.798	0.076	0.1686	0.0043	0.0199	1004	24	1046	28
C3	2.180	0.110	0.1899	0.0051	0.3066	1120	28	1151	32
C4	1.880	0.084	0.1757	0.0045	0.0137	1042	25	1061	29
D2_Core	1.933	0.055	0.1857	0.0043	0.3272	1099	24	1090	19
E1	2.287	0.074	0.1989	0.0047	0.0814	1169	25	1208	23
E2	2.219	0.097	0.1953	0.0053	0.2145	1151	29	1174	30
E3	2.049	0.058	0.1864	0.0043	0.1363	1102	23	1129	19
E4	2.010	0.065	0.1876	0.0045	0.1003	1108	24	1122	22
F2	1.976	0.058	0.1823	0.0042	0.1889	1079	23	1105	20
F3	2.143	0.086	0.1917	0.0048	0.0757	1130	26	1155	27
F4	1.881	0.071	0.1792	0.0047	0.1431	1062	26	1077	26
D3	2.180	0.110	0.1984	0.0055	0.2593	1166	30	1163	34
D4	2.211	0.085	0.1923	0.0047	0.2404	1133	26	1182	26

weighted mean age of 1013± 9 Ma (MSWD = 0.5) in agreement with the age obtained for ore zircon age (Fig, 13a, c; Z3, Z4).

2.4.8.3 Ore Rock Zircon

Analyses of zircon separated from the REE ore show faint zoning in BSE images. Twenty analyses of zircon overlap within analytical precision and yield a weighted mean $^{206}Pb/^{238}U$ age of 995 ± 7 Ma (MSWD=0.8) (Fig. 13a, c; Z3). The remaining eleven analyses yield a weighted mean $^{206}Pb/^{238}U$ age of 1022 ± 8 Ma (MSWD=1.5) (Fig. 13a, c; Z4), and may represent slightly older inherited component similar in age to zircon rims of the host syenite.

2.4.8.4 Syenitic Monazite

BSE images of syenititic monazite show light irregular zonations in the cores, with rims that are homogenous (Fig 9a, c, e). Ages do not significantly differ between rim and core analyses. Sixteen analyses of monazite from the syenite host rock overlap within analytical precision and give a weighted mean $^{206}Pb/^{238}U$ age of 1041±11Ma (MSWD=1.4) (Fig. 13b, d; M1).

2.4.8.5 Ore monazite

Fifteen analyses of monazite, a single sample with large error and upper and lower outliers were omitted, from the ore body form two groups that overlap within analytical precision and yield a weighted mean $^{206}Pb/^{238}U$ ages of 1013 ± 8 Ma (MSWD=2.1) (Fig. 13, b, d; M1), and 985 ± 14 Ma (MSWD = 3.6) (Fig. 13b, d; M2),

respectively. The youngest age is in agreement with the age determined from zircon in same ore sample (999 ± 5 Ma) (Fig. 13a, c; Z4).

2.4.9 ID-TIMS

Given that LA-ICPMS analyses are accurate and precise to ~2%, further refinement of age data was completed using ID-TIMS. Samples of ore monazite, titanite-(Ce), allanite, and syenitic monazite from PH-1, PH-2, and PH-5 were taken to represent the $^{207}Pb/^{235}U$ ages of REE ore and syenite (Fig. 14, 15; Table 7).

2.4.9.1 Allanite

Five fragments of allanite were removed from thin sections. The oldest age is 1083 ± 11 Ma with four other ages are between 1022 ± 14 and 994 ± 7 Ma (Fig. 14, 15d).

2.4.9.2 Titanite-(Ce)

Four fragments of titanite-(Ce) were removed from thin sections PH-2. Ages range from 1064 ± 4 to 1055 ± 4 Ma (Fig. 14, 15e).

2.4.9.3 Ore Rock Monazite

One or two fragments were removed from thin section from the centers of three grains of monazite in sample PH-1 and additional fragments from three grains were removed from a grain mount of the same sample. The oldest date is 1001 ± 2 Ma. The next five youngest dates are equivalent with a weighted mean of 984 ± 1 Ma (Fig 14, 15b), slightly younger than U-Pb ages determined using the LASS technique. The two youngest dates are from the same grain are equivalent at ~963 Ma. The youngest date is

Table 6

TABLE 6: LASS MONAZITE U-Pb RESULTS

Grain & Analysis No.	Measured Values					Calculated Ages			
	$^{207}Pb/^{235}U$	2σ Error (abs.)*	$^{206}Pb/^{238}U$	2σ Error (abs.)	RHO	$^{206}Pb/^{238}U$ Age (Ma)	2σ Error (abs.)	$^{207}Pb/^{235}U$ Age (Ma)	2σ Error (abs.)
Syenitic Monazite									
mz1_pt1	1.776	0.019	0.1704	0.0010	0.3465	1015	6	1036	7
mz1_pt2	1.954	0.032	0.1780	0.0016	0.2308	1055	9	1097	11
mz2_pt1	1.855	0.022	0.1796	0.0013	0.3359	1065	7	1065	8
mz2_pt2	1.860	0.016	0.1790	0.0010	0.3870	1062	6	1068	6
mz5_pt1	1.799	0.023	0.1703	0.0013	0.3825	1014	7	1045	9
mz5_pt2	1.774	0.015	0.1711	0.0010	0.3480	1019	6	1036	5
mz6_pt1	1.763	0.020	0.1731	0.0013	0.3047	1029	7	1032	8
mz6_pt2	1.778	0.015	0.1728	0.0012	0.4390	1028	7	1037	6
mz6_pt3	1.851	0.019	0.1737	0.0012	0.3751	1032	6	1063	7
mz6_pt4	1.807	0.017	0.1766	0.0013	0.3379	1048	7	1047	6
mz6_pt5	1.862	0.015	0.1800	0.0012	0.4813	1067	7	1068	5
mz6_pt6	2.076	0.031	0.1793	0.0012	0.3831	1063	7	1140	10
mz7_pt1	1.960	0.014	0.1797	0.0010	0.1888	1065	5	1101	5
mz7_pt2	1.751	0.022	0.1706	0.0012	0.1922	1015	6	1028	8
mz7_pt3	1.879	0.021	0.1761	0.0012	0.2983	1045	7	1074	7
mz7_pt4	1.954	0.023	0.1755	0.0012	0.2529	1043	7	1097	8

Note: Each analysis represents a singe laser ablation point on monazite grains in ore and syenitic thin sections, PH-1 and PH-5, respectively.

Data were measured using LASS, LA-MC-ICPMS and reduced using Iolite (version 2.15) by Paton et al. (2011).

*All errors are 2 sigma and absolute.

TABLE 6 (continued): LASS MONAZITE U-Pb RESULTS

Grain & Analysis No.	Measured Values					Calculated Ages			
	$^{207}Pb/^{235}U$	2σ Error (abs.)*	$^{206}Pb/^{238}U$	2σ Error (abs.)	RHO	$^{206}Pb/^{238}U$ Age (Ma)	2σ Error (abs.)	$^{207}Pb/^{235}U$ Age (Ma)	2σ Error (abs.)
Ore Monazite									
mz1_pt1	1.686	0.042	0.1704	0.0020	0.2204	1014	11	999	16
mz1_pt2	1.657	0.037	0.1671	0.0017	0.1804	996	9	991	14
mz1_pt3	1.692	0.052	0.1694	0.0021	0.0794	1009	12	998	19
mz2_pt1	1.641	0.057	0.1619	0.0026	0.1593	966	14	988	22
mz2_pt2	1.765	0.073	0.1727	0.0029	0.1218	1028	16	1027	26
mz2_pt3	1.875	0.063	0.1744	0.0025	0.2358	1036	14	1069	22
mz3_pt1	1.760	0.055	0.1721	0.0023	0.1430	1025	12	1025	20
mz3_pt2	1.741	0.052	0.1687	0.0022	0.0846	1004	12	1020	19
mz3_pt3	1.694	0.068	0.1668	0.0027	0.2125	994	15	1010	25
mz4_pt1	1.714	0.047	0.1707	0.0020	0.1677	1015	11	1010	17
mz4_pt2	1.596	0.033	0.1642	0.0018	0.3051	980	10	966	13
mz4_pt3	1.789	0.049	0.1784	0.0020	0.1460	1058	11	1037	18
mz4_pt4	1.685	0.038	0.1690	0.0018	0.2156	1006	10	998	14
mz5_pt1	1.651	0.055	0.1626	0.0024	0.1566	970	13	991	21
mz5_pt2	1.752	0.068	0.1638	0.0024	0.1433	977	14	1022	25
mz5_pt3	1.663	0.088	0.1726	0.0035	0.0570	1025	19	998	33

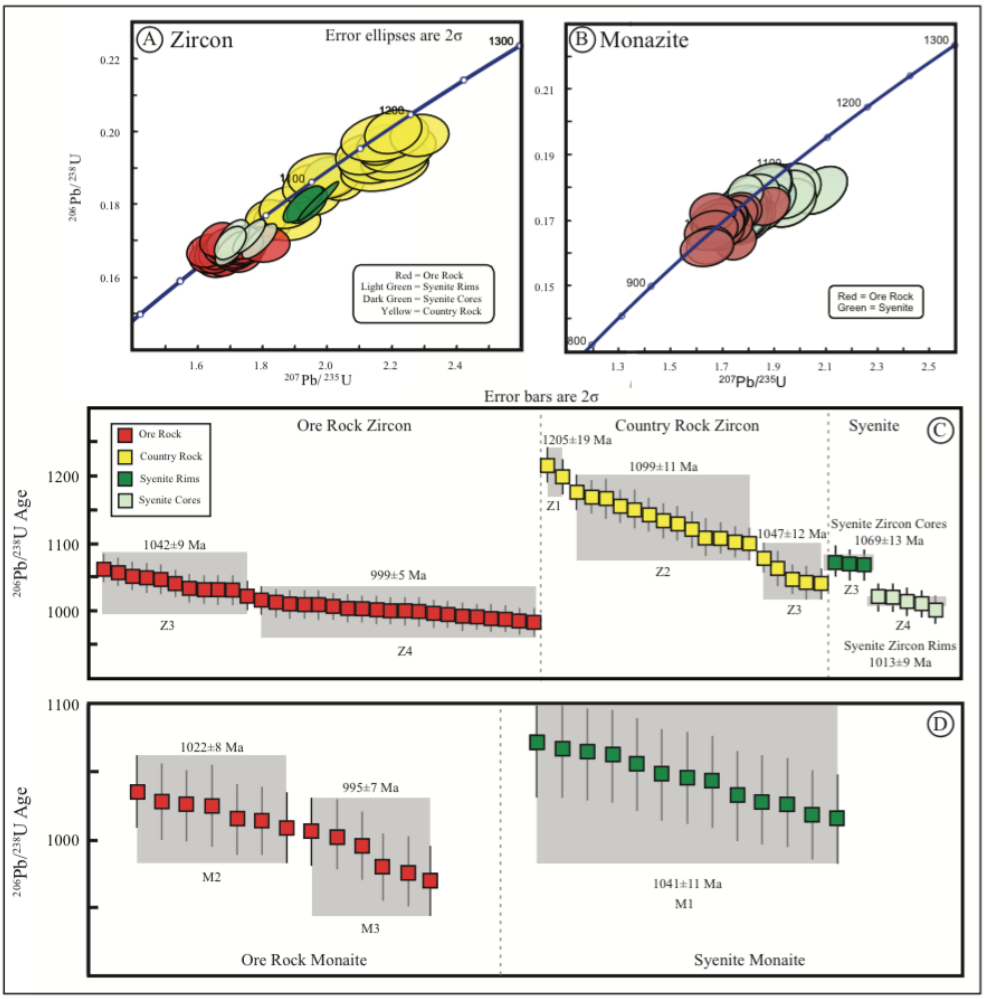

Chafe et al. Figure 13

Figure 13.

U-Pb concordia diagrams (top) and weighted mean plots (bottom) based on LA-ICPMS analyses on zircon and monazite. Grains from ore rock (PH-1, PH-2) are shown in red, syenite (PH-5) is shown in green, and country rock (PH-10) is shown in yellow. Concordia plots for zircon and monazite, A and B, respectively contain all analyses. ^{206}Pb-^{238}U ages have been used to calculate weighted mean ages. Results are presented in C and D where grey rectangles show the average age of generations of each mineral. Four generations of zircon are observed and represent the following; Z1, inherited country rock cores; Z2, crystallization of country rock; Z3, late alteration of country rock during crystallization of syenite and early ore; Z4, late crystallization of syenitic zircon rims and ore.

944 ± 1 Ma. Due to the agreement of monazite results at 984 Ma, this age has been chosen to represent the age of monazite and non-silicate REE mineral crystallization at Pope's Hill.

2.4.9.4 Fergusonite

Five fragments of fergusonite were removed from thin sections. All ages are discordant, and lie along a poorly fitted concordia line, closer to the upper intercept than the lower, with intercept ages of 937 ± 23 and 339 ± 110 Ma with an MSWD of 61 (Fig 15f) for this reason, fergusonite was dropped from further examination.

Overall, dates range from 1063 to 984 Ma in allanite, 1055 to 1046 Ma in titanite, and 1000 to 944 Ma in monazite.

2.4.9.5 Syenite Monazite

Fragments from five grains of monazite were removed from thin sections and another five grains were removed from a grain mount of sample PH-5 (Fig 14, 15c). The oldest date is 1009 ± 1 Ma. The next youngest 12 dates are evenly spaced in time between 1002 ± 1 and 986 ± 2 Ma. The youngest age is 977 ± 1 Ma.

Table 7

Table 7. ID-TIMS U-Pb ISOTOPIC DATA

Sample (a)	Th/U (b)	$^{206}Pb^*$ x10^{-13} mol (c)	mol % $^{206}Pb^*$ (c)	Pb^*/Pb_c (c)	Pb_c (pg) (c)	$^{206}Pb/^{204}Pb$ (d)
Ore Rock, PH-1 (grain mount):						
m18	45.885	3.0759	99.60%	951	1.01	4616
m97a	259.538	0.6633	98.36%	1208	0.91	1121
m97b	245.107	0.9141	99.01%	1899	0.76	1848
m103b	131.082	11.5679	99.17%	1203	8.21	2083
Ore Rock, PH-1 (thin section):						
m5a	135.266	0.7718	98.86%	907	0.74	1570
m5b	124.784	0.5451	98.27%	551	0.80	1032
m6a	123.812	1.0088	98.51%	637	1.28	1185
m6b	126.471	0.7631	98.60%	693	0.91	1271
m8	37.190	0.6972	98.92%	284	0.63	1678
Ore Rock, PH-2 (thin section):						
t2	33.650	5.9435	86.70%	17	80.02	127
t3	33.043	6.1740	87.00%	18	80.97	130
t4	34.880	4.5957	86.36%	18	63.73	124
t5	34.601	5.1880	86.43%	17	71.48	125
f1	3.329	40.9457	99.80%	257	7.02	8687
f2	3.117	61.4393	99.94%	762	3.41	26807
f3	3.287	39.0230	99.86%	359	4.74	12256
f4	3.213	32.3978	99.93%	742	1.88	25729
f5	3.300	38.3836	99.96%	1215	1.37	41903
a1	118.343	0.3169	75.23%	26	9.13	69
a2	118.601	0.4604	81.80%	39	8.97	93
a3	94.620	0.2537	78.69%	26	6.00	80
a4	100.896	0.3371	84.16%	40	5.54	108
a5	161.371	0.2175	76.79%	39	5.74	73
Syenite, PH-5 (grain mount):						
m1	44.838	73.7149	99.77%	1535	14.70	7349
m2	51.524	446.7521	99.41%	689	226.38	2896
m3	36.711	111.4575	99.26%	401	70.82	2314
m4	50.361	124.7298	99.50%	796	53.51	3419
m5	38.577	88.6348	99.61%	795	29.74	4368
Syenite, PH-5 (thin section):						
m1	36.394	4.7200	98.17%	160	7.49	941
m2a	45.822	9.3547	99.65%	1065	2.74	5060
m2b	19.221	9.6411	99.71%	585	2.36	6062
m3	36.553	2.2358	99.07%	321	1.77	1903
m4a	38.843	25.6459	99.72%	1120	6.14	6145
m4b	36.486	4.3084	99.61%	775	1.41	4599
m5a	40.676	14.4912	99.49%	647	6.27	3407
m5b	39.038	10.9225	99.61%	804	3.66	4419
m5c	33.851	11.4908	99.75%	1105	2.47	6901

TABLE 7 (continued). ID-TIMS U-Pb ISOTOPIC DATA

	Radiogenic Isotope Ratios								Isotopic Ages					
Sample (a)	$^{208}Pb/^{206}Pb$ (e)	$^{207}Pb/^{206}Pb$ (e)	% err (f)	$^{207}Pb/^{235}U$ (e)	% err (f)	$^{206}Pb/^{238}U$ (e)	% err (f)	corr. coef.	$^{207}Pb/^{206}Pb$ (g)	± (f)	$^{207}Pb/^{235}U$ (g)	± (f)	$^{206}Pb/^{238}U$ (g)	± (f)
Ore Rock, PH-1 (grain mount):														
m18	13.980	0.071914	0.150	1.635044	0.200	0.164899	0.074	0.775	983.50	3.06	983.80	1.26	983.94	0.67
m97a	78.642	0.071642	0.569	1.643111	0.642	0.166340	0.131	0.626	975.79	11.61	986.91	4.05	991.92	1.21
m97b	74.469	0.071687	0.352	1.633282	0.414	0.165241	0.124	0.611	977.07	7.17	983.13	2.61	985.84	1.13
m103b	39.983	0.070467	0.142	1.534614	0.202	0.157948	0.085	0.813	941.98	2.90	944.35	1.24	945.36	0.74
Ore Rock, PH-1 (thin section):														
m5a	40.951	0.072134	0.286	1.680107	0.347	0.168926	0.111	0.657	989.72	5.82	1001.02	2.21	1006.19	1.04
m5b	37.922	0.071774	0.423	1.637793	0.505	0.165498	0.180	0.597	979.53	8.61	984.86	3.18	987.26	1.65
m6a	37.814	0.071303	0.247	1.583328	0.300	0.161050	0.088	0.693	966.12	5.05	963.68	1.87	962.61	0.79
m6b	38.524	0.071098	0.293	1.582199	0.364	0.161400	0.103	0.761	960.23	5.99	963.23	2.26	964.55	0.93
m8	11.312	0.071755	0.317	1.632583	0.373	0.165013	0.099	0.651	979.01	6.47	982.86	2.35	984.58	0.91

Note: J. Crowley at Boise State University collected analyses and compiled this table.

(a) m1, m2, etc. are labels for analyses composed of single grains or fragments of monazite. t1, t2, etc. are labels for analyses composed of single fragments of titanite-(Ce). a1, a2, etc. are labels for analyses composed of single fragments of allanite. f1, f2, etc. are labels for analyses composed of single fragments of fergusonite. Labels with letters are fragments from the same grain. Labels in bold denote dates used in weighted mean calculation.

(b) Model Th/U ratio calculated from radiogenic $^{208}Pb/^{206}Pb$ ratio and $^{207}Pb/^{235}U$ date.

(c) Pb* and Pbc are radiogenic and common Pb, respectively. mol % ^{206}Pb* is with respect to radiogenic and blank Pb.

(d) Measured ratio corrected for spike and fractionation only. Fractionation correction is 0.18 ± 0.03 (1 sigma) %/amu (atomic mass unit) for single-collector Daly analyses, based on analysis of EARTHTIME ^{202}Pb-^{205}Pb tracer solution. Fractionation correction is 0.10 ± 0.02 (1 sigma) %/amu (atomic mass unit) for multi-collector Faraday-Daly analyses, based on analysis of EARTHTIME ^{202}Pb-^{205}Pb tracer solution.

(e) Corrected for fractionation, spike, common Pb, and initial disequilibrium in $^{230}Th/^{238}U$. Procedural Pb blank is assumed to be 1.0 pg with composition of $^{206}Pb/^{204}Pb$ = 18.35 ± 1.50%; $^{207}Pb/^{204}Pb$ = 15.60 ± 0.75%; $^{208}Pb/204Pb$ = 38.08 ± 1.00% (1 sigma). The remainder of the common Pb is assigned to the mineral with a composition determined by Stacey and Kramers (1975) or from K-feldspar analysis (see text).

(f) Errors are 2 sigma, propagated using algorithms of Schmitz and Schoene (2007).

(g) Calculations based on the decay constants of Jaffey et al. (1971).

TABLE 7 (continued). ID-TIMS U-Pb ISOTOPIC DATA

	Radiogenic Isotope Ratios								Isotopic Ages					
Sample (a)	$^{208}Pb/^{206}Pb$ (e)	$^{207}Pb/^{206}Pb$ (e)	% err (f)	$^{207}Pb/^{235}U$ (e)	± % err (f)	$^{206}Pb/^{238}U$ (e)	% err (f)	corr. coef.	$^{207}Pb/^{206}Pb$ (g)	± (f)	$^{207}Pb/^{235}U$ (g)	± (f)	$^{206}Pb/^{238}U$ (g)	± (f)
Ore Rock, PH-2 (thin section):														
t2	10.207	0.074791	0.545	1.849845	0.604	0.179385	0.097	0.659	1062.88	10.96	1063.37	3.98	1063.62	0.95
t3	10.025	0.074647	0.531	1.838622	0.591	0.178641	0.099	0.652	1059.00	10.70	1059.37	3.88	1059.55	0.97
t4	10.634	0.074824	0.557	1.826037	0.616	0.176997	0.098	0.654	1063.78	11.21	1054.86	4.04	1050.55	0.95
t5	10.520	0.075010	0.554	1.852608	0.613	0.179128	0.099	0.652	1068.77	11.13	1064.36	4.04	1062.21	0.97
f1	1.064	0.068037	0.044	1.179885	0.092	0.125776	0.055	0.942	869.67	0.91	791.26	0.51	763.72	0.40
f2	0.978	0.069006	0.041	1.316269	0.091	0.138343	0.058	0.946	898.92	0.85	852.88	0.53	835.28	0.45
f3	1.038	0.069122	0.066	1.294426	0.131	0.135819	0.072	0.954	902.39	1.36	843.26	0.75	820.97	0.56
f4	1.012	0.069012	0.069	1.299960	0.132	0.136617	0.072	0.938	899.10	1.42	845.70	0.76	825.50	0.56
f5	1.025	0.069595	0.062	1.398491	0.127	0.145740	0.069	0.969	916.43	1.27	888.30	0.75	877.04	0.57
a1	35.553	0.074873	1.502	1.904637	1.619	0.184496	0.230	0.561	1065.10	30.21	1082.71	10.78	1091.49	2.31
a2	35.851	0.072546	1.010	1.715123	1.103	0.171467	0.183	0.571	1001.29	20.51	1014.20	7.08	1020.19	1.73
a3	28.607	0.072881	2.069	1.736837	2.225	0.172839	0.366	0.494	1010.65	41.95	1022.29	14.34	1027.74	3.47
a4	30.809	0.072495	0.993	1.662781	1.096	0.166351	0.187	0.612	999.87	20.16	994.44	6.95	991.97	1.72
a5	48.938	0.072298	1.725	1.682698	1.890	0.168803	0.470	0.460	994.33	35.06	1002.00	12.04	1005.51	4.37

TABLE 7 (continued). ID-TIMS U-Pb ISOTOPIC DATA

	Radiogenic Isotope Ratios								Isotopic Ages					
Sample (a)	$^{208}Pb/^{206}Pb$ (e)	$^{207}Pb/^{206}Pb$ (e)	% err (f)	$^{207}Pb/^{235}U$ (e)	± % err (f)	$^{206}Pb/^{238}U$ (e)	% err (f)	corr. coef.	$^{207}Pb/^{206}Pb$ (g)	± (f)	$^{207}Pb/^{235}U$ (g)	± (f)	$^{206}Pb/^{238}U$ (g)	± (f)
Syenite, PH-5 (grain mount):														
m1	13.657	0.072200	0.045	1.655282	0.092	0.166277	0.055	0.938	991.60	0.91	991.57	0.58	991.56	0.50
m2	15.728	0.072365	0.062	1.655579	0.141	0.165928	0.111	0.903	996.22	1.27	991.69	0.89	989.64	1.02
m3	11.176	0.072277	0.059	1.663003	0.105	0.166876	0.061	0.877	993.74	1.20	994.52	0.67	994.87	0.57
m4	15.347	0.072492	0.053	1.672131	0.106	0.167293	0.069	0.900	999.79	1.08	998.00	0.68	997.18	0.64
m5	11.768	0.072493	0.055	1.667412	0.098	0.166819	0.056	0.888	999.82	1.12	996.20	0.62	994.56	0.52
Syenite, PH-5 (thin section):														
m1	11.108	0.072162	0.145	1.643101	0.206	0.165142	0.091	0.792	990.50	2.95	986.90	1.30	985.29	0.83
m2a	13.943	0.072063	0.095	1.651127	0.151	0.166174	0.072	0.864	987.73	1.94	989.98	0.95	991.00	0.66
m2b	5.828	0.072574	0.094	1.701843	0.149	0.170074	0.072	0.863	1002.07	1.91	1009.22	0.95	1012.52	0.68
m3	11.127	0.071928	0.201	1.640166	0.252	0.165383	0.081	0.725	983.89	4.09	985.78	1.59	986.62	0.74
m4a	11.826	0.072473	0.072	1.675289	0.135	0.167654	0.071	0.944	999.24	1.46	999.20	0.86	999.18	0.66
m4b	11.108	0.072065	0.120	1.648708	0.173	0.165927	0.073	0.829	987.78	2.44	989.06	1.09	989.63	0.67
m5a	12.393	0.072335	0.084	1.662728	0.146	0.166713	0.074	0.913	995.39	1.70	994.42	0.92	993.97	0.68
m5b	11.874	0.072499	0.080	1.681729	0.141	0.168238	0.070	0.932	999.97	1.63	1001.64	0.90	1002.40	0.65
m5c	10.360	0.071979	0.079	1.618127	0.141	0.163044	0.072	0.919	985.35	1.62	977.26	0.88	973.67	0.65

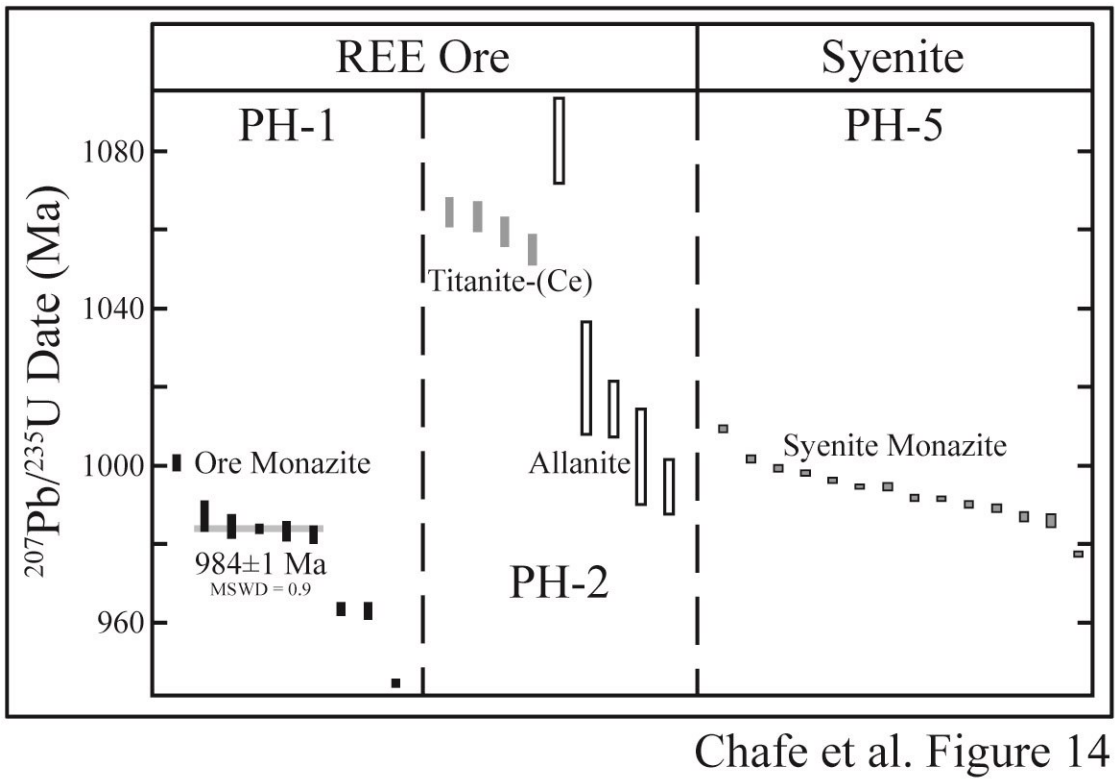

Figure 14.

^{207}Pb-^{235}U ages from ID-TIMS analyses from ore samples PH-1 and PH-2 (left), and syenitic sample PH-5 (right) arranged by mineral in decreasing order. Ore monazite ages are in agreement at 984±1 Ma with MSWD of 0.9. A wide range of ages observed in allanite and titanite-(Ce) may be the result of mixing.

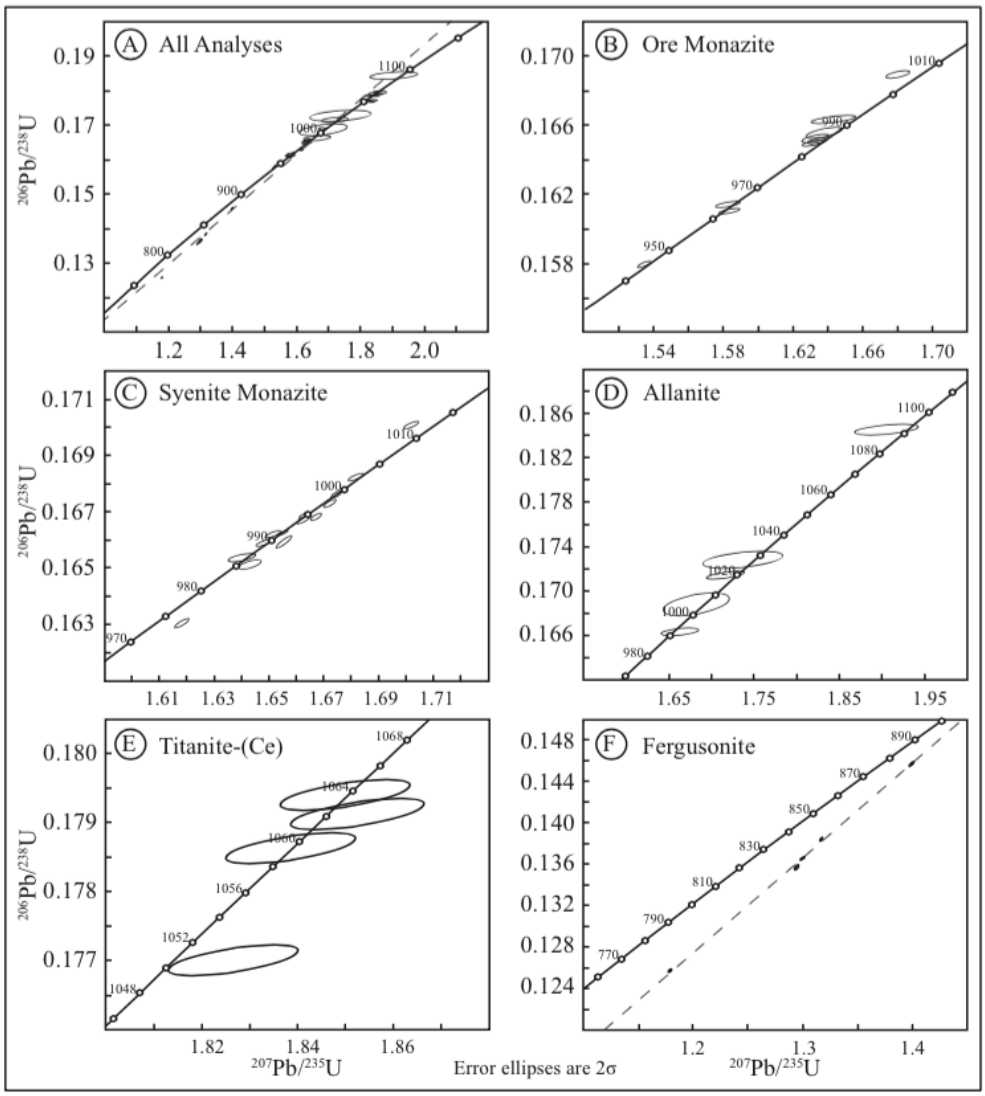

Figure 15.

U-Pb concordia diagrams based on ID-TIMS results from REE mineral analyses. Concordia is plotted as a solid line, with mean sampled values plotted as a dashed line. A. all analyses; B. ore monazite; C. host monazite; D. allanite; E. titanite-(Ce); F. fergusonite.

2.4.10 Sm-Nd Isotope Systematics

Given that mineral textures and ID-TIMS geochronology reveal the replacement of allanite and titanite by later monazite and britholite, the $^{147}Sm/^{144}Nd$ and $^{143}Nd/^{144}Nd$ ratios are discussed based on this distinction (Table 8, Fig 16a). Titanite-(Ce), and allanite overlap in Sm-Nd isotope space and give an isochron age of 943 ± 98 Ma (MSWD = 2.3) (Fig. 16a). Isochrons for ore monazite and britholite have not been calculated since there exists potential for differential loss of radiogenic Sm during secondary crystallization in an open hydrothermal system. A single whole rock sample from the host syenite along with ore monazite plot on an isochron below the ore minerals with a highly imprecise age of 922 ± 240 Ma (MSWD = 0.26) (Fig. 16a). The age of these isochrons, however, should be viewed with caution as the errors are generally quite large given the limited spread in Sm-Nd, and the relative infancy of the LA-MC-ICPMS LASS technique that has yet to be tested for the veracity of the resulting isochron ages.

Epsilon Nd isotope compositions were calculated using CHUR values of Bouvier et al. (2008), and the age of mineralization from ore monazite ID-TIMS results, 984 Ma (Table 8, Fig. 14a), and have been shown to be both accurate and precise (Fisher et al., 2011). The silicate REE minerals allanite and titanite have ϵNd_{984} of +0.2 and +0.3, respectively which overlap within analytical uncertainty with the non-silicate, ore minerals which give a mean ϵNd_{984} of +0.9 for ore monazite and +0.6 for britholite. Monazite from the syenitic sample has a lower ϵNd_{984} of -2.4, compared to other REE bearing minerals.

Table 8

TABLE 8: LA-ICPMS Sm-Nd RESULTS

	Isochron Values				Measured Values						Calculated Values*	
Grain & Analysis No.	$^{147}Sm/^{144}Nd$	2σ Error (abs.)*	$^{143}Nd/^{144}Nd$	2σ Error (abs.)	$^{145}Nd/^{144}Nd$	2σ Error (abs.)	Eu*	2σ Error (abs.)	Ce/Gd	2σ Error (abs.)	ϵNd_{984}	2σ Error (abs.)
Syenite Monazite, PH-5												
mz1_pt1	0.0444	0.000062	0.511519	0.000038	0.348438	0.000019	0.5273	0.0040	141	0.46	-2.5	0.7
mz1_pt2	0.0432	0.000140	0.511499	0.000032	0.348440	0.000022	0.5493	0.0017	154	2.00	-2.8	0.6
mz2_pt1	0.0442	0.000034	0.511491	0.000025	0.348433	0.000028	0.5813	0.0006	147	0.48	-3.1	0.5
mz2_pt2	0.0437	0.000190	0.511553	0.000045	0.348455	0.000027	0.5693	0.0018	158	1.70	-1.5	0.9
mz5_pt1	0.0451	0.000013	0.511523	0.000039	0.348441	0.000028	0.5006	0.0033	139	0.18	-2.3	0.8
mz5_pt2	0.0449	0.000110	0.511525	0.000048	0.348451	0.000037	0.5213	0.0089	141	1.20	-2.5	0.9
mz6_pt1	0.0451	0.000014	0.511539	0.000038	0.348440	0.000031	0.4945	0.0014	140	0.14	-2.1	0.7
mz6_pt2	0.0445	0.000100	0.511521	0.000053	0.348439	0.000021	0.5610	0.0009	150	0.55	-2.5	1.0
mz6_pt3	0.0460	0.000330	0.511521	0.000040	0.348447	0.000023	0.4928	0.0022	136	1.80	-2.9	0.8
mz6_pt4	0.0450	0.000025	0.511520	0.000044	0.348421	0.000019	0.5099	0.0005	143	0.59	-2.7	0.9
mz6_pt5	0.0437	0.000110	0.511536	0.000030	0.348436	0.000031	0.5676	0.0038	157	1.50	-2.1	0.6
mz6_pt6	0.0449	0.000040	0.511507	0.000030	0.348427	0.000030	0.5134	0.0011	144	0.59	-2.6	0.6
mz7_pt1	0.0439	0.000170	0.511503	0.000038	0.348446	0.000030	0.5737	0.0018	156	1.30	-2.6	0.7
mz7_pt2	0.0450	0.000057	0.511536	0.000041	0.348462	0.000016	0.4981	0.0093	142	0.35	-2.6	0.8
mz7_pt3	0.0449	0.000042	0.511520	0.000031	0.348452	0.000029	0.5139	0.0062	144	0.35	-2.7	0.6
mz7_pt4	0.0451	0.000008	0.511549	0.000033	0.348458	0.000025	0.4900	0.0006	142	0.31	-2.0	0.6

Note: Each analysis represents a singe laser ablation point on grains in ore and syenitic thin sections, PH-1, PH-2, and PH-5.

Titanite-(Ce), allanite, and britholite were measured by LA-MC-ICPMS. Monazite was measured by LASS simultaneously with U-Pb.

All data were reduced using Iolite (version 2.15) by Paton et al. (2011).

*All errors are 2 sigma and absolute.

TABLE 8 (continued): LA-ICPMS Sm-Nd RESULTS

Grain & Analysis No.	Isochron Values				Measured Values						Calculated Values*	
	$^{147}Sm/^{144}Nd$	2σ Error (abs.)*	$^{143}Nd/^{144}Nd$	2σ Error (abs.)	$^{145}Nd/^{144}Nd$	2σ Error (abs.)	Eu*	2σ Error (abs.)	Ce/Gd	2σ Error (abs.)	ϵNd_{984}	2σ Error (abs.)
Ore Monazite, PH-1												
mz1_pt1	0.0776	0.000430	0.511910	0.000027	0.348429	0.000019	0.0739	0.0001	26	0.36	+0.9	0.5
mz1_pt2	0.0816	0.000055	0.511963	0.000028	0.348434	0.000025	0.0740	0.0001	23	0.09	+1.4	0.5
mz1_pt3	0.0749	0.000150	0.511898	0.000023	0.348449	0.000011	0.0747	0.0003	29	0.18	+1.0	0.5
mz2_pt1	0.0708	0.000064	0.511879	0.000028	0.348428	0.000023	0.0789	0.0003	36	0.10	+1.1	0.5
mz2_pt2	0.0666	0.000099	0.511823	0.000047	0.348432	0.000021	0.0738	0.0001	43	0.16	+0.6	0.9
mz2_pt3	0.0708	0.000080	0.511887	0.000025	0.348449	0.000017	0.0738	0.0002	36	0.15	+1.3	0.5
mz3_pt1	0.0697	0.002000	0.511797	0.000037	0.348412	0.000028	0.0760	0.0007	38	3.10	-0.3	0.7
mz3_pt2	0.0677	0.000200	0.511845	0.000026	0.348413	0.000017	0.0775	0.0001	40	0.32	+0.8	0.5
mz3_pt3	0.0726	0.000700	0.511866	0.000032	0.348425	0.000013	0.0754	0.0002	32	0.93	+0.6	0.6
mz4_pt1	0.0767	0.000036	0.511926	0.000034	0.348430	0.000022	0.0736	0.0001	27	0.05	+1.3	0.7
mz4_pt2	0.0820	0.000270	0.511944	0.000017	0.348441	0.000016	0.0733	0.0001	22	0.28	+1.0	0.3
mz4_pt3	0.0768	0.000240	0.511901	0.000025	0.348430	0.000024	0.0743	0.0002	26	0.36	+0.8	0.5
mz4_pt4	0.0801	0.000230	0.511930	0.000019	0.348430	0.000019	0.0733	0.0001	24	0.18	+0.9	0.4
mz5_pt1	0.0754	0.000060	0.511858	0.000023	0.348434	0.000020	0.0746	0.0001	28	0.12	+0.1	0.5
mz5_pt2	0.0713	0.000082	0.511858	0.000017	0.348442	0.000017	0.0759	0.0001	34	0.18	+0.6	0.3
mz5_pt3	0.0703	0.000350	0.511860	0.000023	0.348435	0.000022	0.0748	0.0001	32	0.41	+0.8	0.5
mz6_pt1	0.0800	0.000140	0.511918	0.000019	0.348435	0.000017	0.0725	0.0003	23	0.09	+0.7	0.4
mz7_pt1	0.0712	0.000081	0.511879	0.000027	0.348453	0.000025	0.0754	0.0004	32	0.11	+1.1	0.5
mz8_pt1	0.0708	0.000380	0.511863	0.000032	0.348442	0.000025	0.0747	0.0005	32	0.50	+0.8	0.6
mz9_pt1	0.0833	0.000240	0.511962	0.000024	0.348448	0.000021	0.0726	0.0003	19	0.13	+1.2	0.5
mz10_pt1	0.0731	0.000270	0.511919	0.000023	0.348457	0.000018	0.0742	0.0005	27	0.38	+1.6	0.5
mz10_pt2	0.0701	0.000093	0.511891	0.000032	0.348458	0.000026	0.0755	0.0007	31	0.10	+1.4	0.6

TABLE 8 (continued): LA-ICPMS Sm-Nd RESULTS

Grain & Analysis No.	Isochron Values				Measured Values						Calculated Values*	
	$^{147}Sm/^{144}Nd$	2σ Error (abs.)*	$^{143}Nd/^{144}Nd$	2σ Error (abs.)	$^{145}Nd/^{144}Nd$	2σ Error (abs.)	Eu*	2σ Error (abs.)	Ce/Gd	2σ Error (abs.)	ϵNd_{984}	2σ Error (abs.)
Titanite-(Ce), PH-1												
ti1_pt1	0.0715	0.000030	0.511837	0.000025	0.348411	0.000021	0.0778	0.0001	35	0.11	+0.2	0.5
ti1_pt2	0.0723	0.000400	0.511835	0.000021	0.348422	0.000015	0.0785	0.0002	34	0.42	+0.1	0.4
ti1_pt3	0.0712	0.000026	0.511822	0.000025	0.348421	0.000024	0.0801	0.0001	37	0.08	-0.0	0.5
ti1_pt4	0.0743	0.000290	0.511911	0.000031	0.348457	0.000023	0.0774	0.0002	31	0.35	+1.3	0.6
ti2_pt1	0.0712	0.000049	0.511846	0.000019	0.348437	0.000017	0.0785	0.0002	35	0.07	+0.4	0.4
ti2_pt2	0.0696	0.000029	0.511837	0.000018	0.348421	0.000016	0.0803	0.0001	38	0.01	+0.4	0.4
ti2_pt3	0.0735	0.000096	0.511867	0.000021	0.348423	0.000016	0.0805	0.0002	33	0.17	+0.6	0.4
ti2_pt5	0.0747	0.000089	0.511926	0.000029	0.348435	0.000017	0.0784	0.0002	30	0.07	+1.5	0.6
ti3_pt1	0.0729	0.000120	0.511836	0.000033	0.348420	0.000031	0.0767	0.0001	33	0.12	+0.0	0.6
ti3_pt2	0.0694	0.000039	0.511832	0.000027	0.348411	0.000023	0.0813	0.0001	38	0.04	+0.4	0.5
ti3_pt3	0.0689	0.000043	0.511836	0.000032	0.348422	0.000020	0.0817	0.0001	40	0.09	+0.5	0.6
ti3_pt4	0.0705	0.000086	0.511807	0.000023	0.348424	0.000029	0.0810	0.0001	38	0.15	-0.3	0.5
ti3_pt5	0.0936	0.000790	0.511980	0.000020	0.348424	0.000020	0.0578	0.0006	19	0.40	+0.2	0.4
ti3_pt6	0.1039	0.000410	0.512039	0.000024	0.348429	0.000026	0.0486	0.0002	14	0.15	+0.1	0.5
ti3_pt7	0.1068	0.001000	0.512051	0.000026	0.348417	0.000025	0.0492	0.0012	13	0.41	-0.1	0.5

TABLE 8 (continued): LA-ICPMS Sm-Nd RESULTS

Grain & Analysis No.	Isochron Values				Measured Values						Calculated Values*	
	$^{147}Sm/^{144}Nd$	2σ Error (abs.)*	$^{143}Nd/^{144}Nd$	2σ Error (abs.)	$^{145}Nd/^{144}Nd$	2σ Error (abs.)	Eu*	2σ Error (abs.)	Ce/Gd	2σ Error (abs.)	ϵNd_{984}	2σ Error (abs.)
Titanite-(Ce), PH-2												
ti1_pt1	0.0724	0.000210	0.511890	0.000038	0.348433	0.000028	0.0797	0.0001	35	0.28	+1.1	0.7
ti1_pt2	0.0714	0.000072	0.511852	0.000031	0.348437	0.000027	0.0813	0.0001	37	0.12	+0.5	0.6
ti1_pt3	0.0733	0.000062	0.511866	0.000028	0.348442	0.000017	0.0780	0.0001	34	0.11	+0.6	0.5
ti1_pt4	0.0748	0.000071	0.511822	0.000034	0.348423	0.000015	0.0772	0.0001	32	0.10	-0.5	0.7
ti1_pt5	0.0701	0.000670	0.511834	0.000030	0.348437	0.000027	0.0779	0.0001	40	1.30	+0.3	0.6
ti1_pt6	0.0764	0.001600	0.511854	0.000020	0.348432	0.000026	0.0762	0.0005	33	1.70	-0.1	0.4
ti1_pt7	0.0704	0.000440	0.511801	0.000037	0.348415	0.000029	0.0773	0.0002	42	0.97	-0.4	0.7
ti1_pt8	0.0780	0.000860	0.511921	0.000035	0.348462	0.000035	0.0785	0.0001	32	1.10	+1.0	0.7
ti1_pt9	0.0751	0.000150	0.511862	0.000028	0.348428	0.000024	0.0768	0.0003	34	0.19	+0.2	0.5
ti1_pt10	0.0751	0.000053	0.511844	0.000031	0.348416	0.000017	0.0758	0.0001	33	0.06	-0.1	0.6
Allanite, PH-1												
al1_pt1	0.0666	0.000230	0.511802	0.000025	0.348418	0.000023	0.0818	0.0004	44	0.35	+0.1	0.5
al1_pt2	0.0633	0.000084	0.511781	0.000027	0.348405	0.000020	0.0788	0.0002	50	0.18	+0.1	0.5
al1_pt3	0.0643	0.000180	0.511788	0.000030	0.348416	0.000022	0.0790	0.0002	47	0.50	+0.2	0.6
al2_pt1	0.0625	0.000210	0.511768	0.000026	0.348400	0.000018	0.0772	0.0002	55	0.41	-0.0	0.5
al2_pt2	0.0732	0.001300	0.511848	0.000032	0.348427	0.000018	0.0749	0.0003	34	1.70	+0.2	0.6
al2_pt3	0.0608	0.000110	0.511765	0.000020	0.348409	0.000014	0.0802	0.0001	60	0.22	+0.2	0.4
al2_pt4	0.0624	0.001000	0.511809	0.000022	0.348410	0.000009	0.0791	0.0003	57	1.90	+0.8	0.4
al2_pt5	0.0627	0.000110	0.511787	0.000026	0.348419	0.000015	0.0786	0.0003	54	0.23	+0.3	0.5
al2_pt6	0.0797	0.002200	0.511907	0.000026	0.348421	0.000016	0.0762	0.0002	29	2.40	+0.5	0.5
al3_pt1	0.0623	0.000069	0.511765	0.000025	0.348387	0.000029	0.0789	0.0001	53	0.10	-0.0	0.5

TABLE 8 (continued): LA-ICPMS Sm-Nd RESULTS

Grain & Analysis No.	Isochron Values				Measured Values						Calculated Values*	
	$^{147}Sm/^{144}Nd$	2σ Error (abs.)*	$^{143}Nd/^{144}Nd$	2σ Error (abs.)	$^{145}Nd/^{144}Nd$	2σ Error (abs.)	Eu*	2σ Error (abs.)	Ce/Gd	2σ Error (abs.)	ϵNd_{984}	2σ Error (abs.)
Allanite, PH-2												
al1_pt1	0.0848	0.000120	0.511926	0.000023	0.348432	0.000025	0.0848	0.0002	26	0.09	+0.3	0.5
al1_pt2	0.0738	0.000089	0.511829	0.000035	0.348437	0.000023	0.0784	0.0002	37	0.06	-0.2	0.7
al1_pt3	0.0835	0.000160	0.511905	0.000030	0.348418	0.000022	0.0875	0.0005	26	0.10	+0.0	0.6
al1_pt4	0.0834	0.000120	0.511873	0.000027	0.348436	0.000026	0.0843	0.0003	26	0.05	-0.6	0.5
al1_pt5	0.0778	0.000130	0.511879	0.000032	0.348448	0.000037	0.0800	0.0005	31	0.11	+0.2	0.6
al1_pt6	0.0736	0.000140	0.511838	0.000035	0.348437	0.000030	0.0799	0.0001	37	0.14	-0.0	0.7
al1_pt7	0.0809	0.000520	0.511908	0.000033	0.348416	0.000032	0.0812	0.0002	29	0.48	+0.4	0.6
al1_pt8	0.0819	0.000230	0.511917	0.000020	0.348432	0.000017	0.0885	0.0002	29	0.27	+0.5	0.4
al2_pt1	0.0813	0.000096	0.511888	0.000023	0.348426	0.000021	0.0757	0.0001	28	0.06	-0.0	0.5
al2_pt2	0.0879	0.000075	0.511933	0.000032	0.348424	0.000027	0.0852	0.0002	23	0.06	+0.0	0.6
Britholite, PH-1												
br1_pt1	0.1734	0.000390	0.512550	0.000032	0.348469	0.000028	0.0793	0.0002	3	0.03	+0.9	0.5
br1_pt2	0.1786	0.000150	0.512563	0.000023	0.348440	0.000025	0.0795	0.0002	2	0.01	+1.3	0.6
br1_pt3	0.1891	0.000740	0.512627	0.000035	0.348453	0.000031	0.0798	0.0001	2	0.02	+0.8	0.7
br2_pt1	0.1654	0.000720	0.512460	0.000048	0.348469	0.000045	0.0814	0.0006	3	0.06	+0.2	0.5
br2_pt2	0.1685	0.000500	0.512464	0.000028	0.348431	0.000035	0.0777	0.0004	3	0.04	+0.5	0.9
br2_pt3	0.1712	0.000230	0.512462	0.000022	0.348443	0.000025	0.0819	0.0001	3	0.02	-0.2	0.4

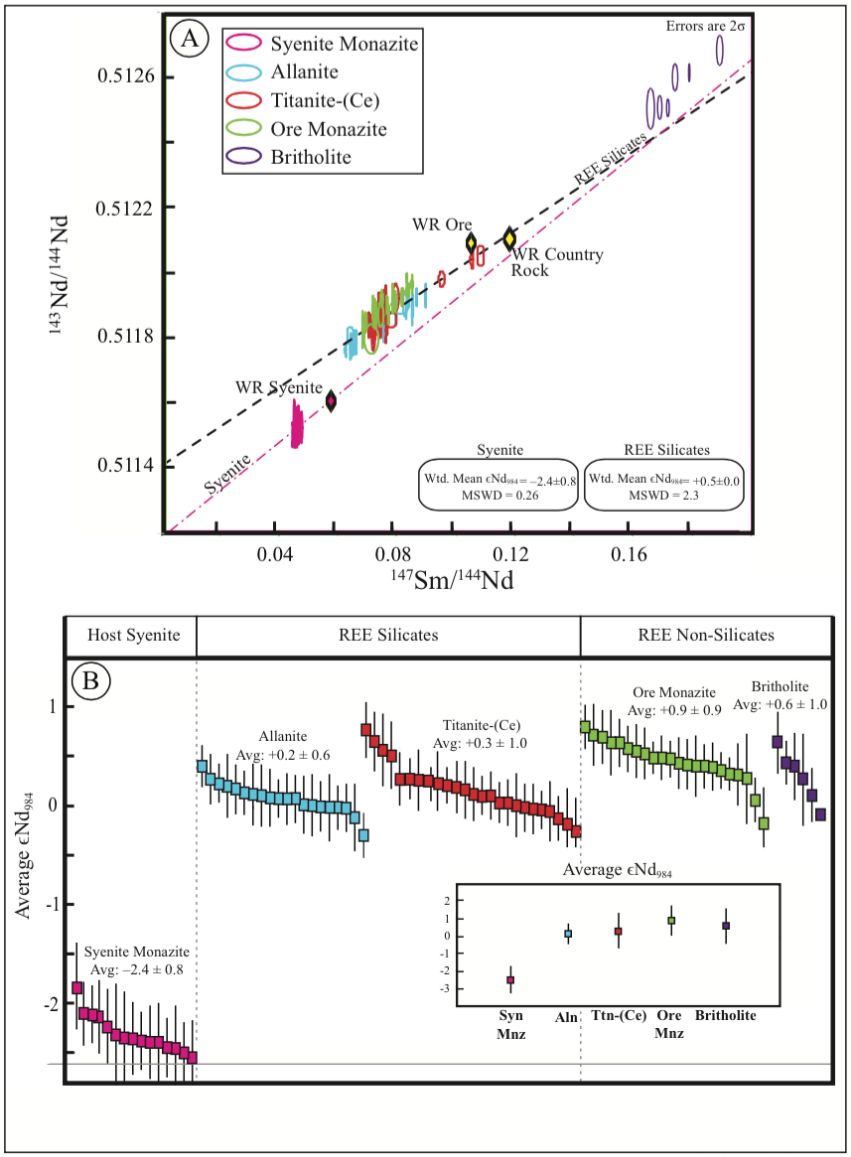

Chafe et al. Figure 16

Figure 16.

(A) Sm-Nd isochrons for silicate REE minerals and syenite based on LA-ICPMS analyses. Ore rock isochron is shown in black and intersects analyses of ore monazite, allanite and titanite-(Ce). The isochron for the syenite has been plotted using the homogenous monazite data as well as whole rock (WR) Sm-Nd values. (B) Weighted mean plot for all data arranged in descending order for each mineral presented in epsilon units at 984 Ma. The average for all ore rock analysis is shown in yellow, ϵNd_{984}=0.4.

2.5 DISCUSSION

2.5.1 REE Abundance and Distribution

The extreme whole rock enrichment of REE found in the mineralized samples of both Pope's Hill and MRT (Table 1) has been characterized above. REE-enriched rocks contain a variety of REE minerals with the REE as essential structural components as opposed to their typical role as trace elements in non-REE minerals. Sample PH-1 contains 18 wt% REE_2O_3 (Table 4) as calculated using SEM-MLA and EPMA results. Whole rock analysis on the same sample by ActLabs (Table 1) yield 21.90% REE. This variation is due to the variable amount of syenitic material included within the whole rock powder compared to the thin section, which essentially dilutes the REE.

Europium depletion and parallel REE patterns in spider diagrams (Fig. 5) in both syenite and ore whole rock samples show a genetic link between mineralization and its host, indicating the ore may be derived from either the syenite itself or share the same source.

2.5.2 Mineral Characterization

The mineral chemistry of Pope's Hill samples is complex both due to the numerous silicate, phosphate, carbonate, and niobate minerals present, but also due to intra-phase chemical variations. A continuum of compositions are present between stoichiometric titanite and titanite-(Ce) (Fig 11a), as well as between apatite and britholite (Fig.11b), both of which have been extensively analyzed by EPMA and LA-ICPMS allowing quantification of their chemical compositions.

The widest variation in chemistry occurs in the Pope's Hill britholite symplectite between apatite and britholite, where samples range from 2.5 to 30.54 wt% REE_2O_3, for apatite and the most enriched britholite. The britholite symplectite has been thoroughly examined and REE substitutions into the structure of apatite-britholite are well studied (i.e.: Fleet and Pan, 1994, 1995, 1997; Pan and Fleet, 2002; Pasero et al., 2010). Britholite from Pope's Hill conforms to the known substitution mechanisms, primarily:

Equation 1

$$REE^{3+} + Si^{4+} = Ca^{2+} + P^{5+}$$

The REE-enrichment is observed to accompany minor increases of ThO_2, SO_3 and Cl, as well as a decrease in F (Table 2). Samples of apatite-britholite plot along a mixing line between stoichiometric apatite and REE-enriched britholite (Fig 11b). Analyses plotting near the $CaO + P_2O_5$ x-axis, the lower right, are stoichiometric apatite and samples near the $REE_2O_3 + Y_2O_3 + SiO_2 + ThO_2 + SO_3 + FeO$ axis are britholite-(high REE). The 1:1 line (Fig. 11b) illustrates the sum of coupled substitutions into the Ca and P_2O_5 sites, including the contribution of trace elements, composition varies linearly between phosphate and silicate-rich end-members.

The REE-enriched titanite-like mineral, titanite-(Ce), represents a new (i.e., unreported in the literature to the best of our knowledge) REE-enriched end-member of titanite. Its chemical composition (Table 2), is 37.6 wt% REE_2O_3, 21.2 wt% SiO_2, 15.4 wt% TiO_2, 11.3 wt% FeO, 3.2 wt% CaO, and 3.2 wt% Nb_2O_5. The mineral is dark red and isotropic in thin section (Fig. 6). This "titanite-(Ce)" is part of a continuum of titanite chemistries and positions this REE enriched Titanite-(Ce) on a mixing line between it and stoichiometric titanite (Fig. 11a). Unfortunately, a flat XRD pattern

indicates the mineral is completely amorphous, alpha-decay has caused extensive metamictization in the mineral due to its high concentration of Th and U (e.g., Holland and Gottfried, 1955 in zircon). Texturally, titanite-(Ce) is subrounded and occupies the core of aureole comprised of ,from center to rim, titanite-(Ce), apatite-britholite-monazite mixture, and allanite (Fig. 8). Titanite-(Ce) has a selective association with fergusonite, ilmenite and stoichiometric titanite, each occurring exclusively in titanite-(Ce) crystals. It is evident that the breakdown of titanite-(Ce) has provided the elements for the crystallization of other Fe-, Nb- and Ti-bearing minerals, while the majority of contained REE may have moved into minerals within the britholite aggregates.

As outlined by Gieré and Sørensen (2004), allanite, a member of the epidote group, is a REE^{3+} and Fe^{2+} end-member of the allanite-epidote (Ca^{2+} and Fe^{3+}) and allanite-clinozoisite (Ca^{2+} and Al^{3+}) series; the former involves a coupled substitution as $REE^{3+} + Fe^{2+}$ replace $Ca^{2+} + Al^{3+}$. Consistent with REE-enrichment described by Gieré and Sørensen (2004) are Th-depletion in enriched samples, as Th and Fe are replaced by REE and Al; and Ti as Fe moves from 3+ to 2+ oxidation states. The chemical composition of allanite at Pope's Hill does not vary significantly, and its composition is between the allanite and clinozoisite end-members.

The amorphous REE silicate phases, allanite and titanite-(Ce) contain between 0.1 and 6.26 wt% ThO_2, and between 0.3 and 1.10 wt% UO_2 (Table 2); this concentration is sufficient to cause extensive radiation damage considering the late Proterozoic age of the rocks, however in the absence of a detailed study of the thermal history of the rock units, as well as the annealing temperature of each individual mineral, actinide concentration and age do not quantify the extent of metamictization. The previously explained glassy

appearance of both allanite and titanite-(Ce), combined with the presence of an amorphous phase, as shown by XRD, is adequate evidence for extensive, radiation damage induced, metamictization. Berman (1955) suggests analysis while heating may provide addition data, however the lack of available literature on REE-enriched titanite renders such work extraneous to the goals of this study.

2.5.3 Geochronology

Uranium-lead dating of zircon, monazite, allanite, and titanite-(Ce) form a paragenetic sequence of the ore-forming events at Pope's Hill (Fig. 17). The crystallization of the country rock minerals and formation of the ore can be traced throughout the Grenvillian events for ~250 Ma, beginning with crystallization of country rock zircon, followed by crystallization of syenitic zircon and REE silicates, and ending with metasomatic breakdown of REE silicates by fluorine, phosphate, carbonate and niobate bearing fluids.

Besides fergusonite, the majority of REE minerals analyzed plot near concordia (Fig 15a), where REE silicates yield older ages than non-silicate REE minerals. Allanite reveals the widest range of ages (Fig. 15d) with the oldest just before crystallization of titanite-(Ce) (Fig. 15e) and the youngest at the beginning of non-silicate crystallization (Fig. 15b) representing a continuum of ages as the oldest primary allanite is mixed with younger, altered material. This is further evidence that silicate REE minerals, allanite and titanite-(Ce), provide an elemental source for the formation of the non-silicate REE minerals.

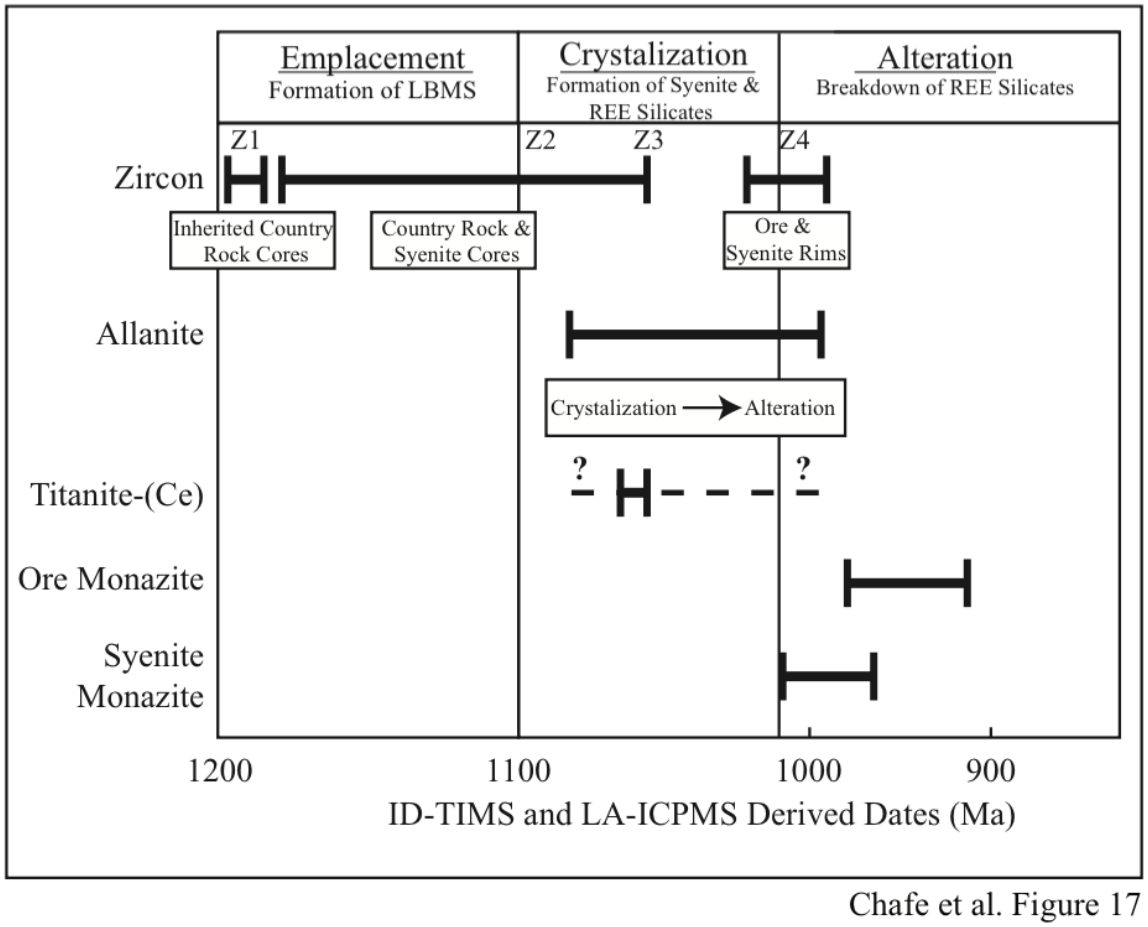

Figure 17.

Paragenetic sequence of the Pope's Hill REE mineralization. Three events are shown from oldest (left) to youngest (right): 1. Emplacement of highly metamorphosed granitic and syenitic rocks crystalizing zircon. 2. Crystallization of REE silicate minerals in isotopically homogenous mixtures. 3. Metasomatic alteration of REE silicates forming F- and REE-enriched phosphate, carbonate, and niobate minerals. Zircon are divided into 4 groups (as in Fig. 13) where labels are placed on the average age of zircon from each generation. Z1, inherited country rock cores; Z2, crystallization of country rock; Z3, late alteration of country rock during crystallization of syenite and early ore; Z4, late crystallization of syenitic zircon rims and ore.

Ore minerals, allanite and titanite all fall along a collinear array in Sm-Nd isotope space (Fig. 16) suggesting that they formed concurrently, but have a different initial Nd isotope composition from the syenitic rock (Table 8) precluding derivation solely from a syenitic host. The slightly higher Nd isotopic composition necessitates derivation, at least in part from a less isotopically evolved source. However, zircon $^{206}Pb/^{238}U$ ages from the syenite cores and titanite-(Ce) are similar at 1069 Ma and 1063 Ma, respectively, and indicate that both crystallized at the same time. Given the close relationship between titanite-(Ce) and allanite, as well as their exclusivity syenite, we conclude that the REE silicate minerals crystalized during the emplacement of syenite at Pope's Hill.

The dates obtained from zircon and monazite are most informative, as they span the largest amount of time. Zircon from mineralized Pope's Hill samples show little zonation in BSE images, but dates between the zones do not differ significantly. Based on field relationships with the gneissic country rock and mineralization, the syenite produces zircon that have weighted mean $^{206}Pb/^{238}U$ ages that: 1) have cores representing the age of syenite emplacement at 1069 Ma, concurrent with the cooling of granitic gneiss of the LBMS, where the country rock zircon ages range from ~1200 to ~1040 Ma; and 2) have rims with an age of 1012 Ma that correspond to younger mineralization at 999 Ma (Fig. 13). Evidently, zircon in the Pope's Hill system have recorded ~200 Ma of igneous, metamorphic, and metasomatic events: the earliest ages are interpreted as inherited cores in the country rock at ~1205 Ma (Fig. 13c; Z1); crystallization of the country rock at ~1100 Ma (Fig. 13c; Z2), the crystallization of the syenite and REE mineralization ~1070 Ma (Fig. 13c; Z3), and subsequent mineralizing events from ~1010 to ~1000 Ma (Fig. 13c; Z4) that record the mineralizing event during either replacement or new

crystallization of zircon in ore samples, associated with the 1012 Ma rims of syenite zircon and late stage mineralization. The similarity of rims from syenitic zircon and ore zircon (Fig. 13c; Z4), also supports late stage mineralization as each yields ages of 1013 Ma and 999 Ma, respectively, corresponding to ID-TIMS data at the youngest monazite age of 984±1 Ma, representing a second mineralizing event. A recent review paper indicates that similar intra-grain textures are due to hydrothermal alteration of the grain (Schaltegger, 2007), which indicates the later mineralizing event is metasomatic.

Persistent throughout all U-Pb data sets are a range of dates that span up to ~150 Ma (Fig. 13c, for example). It is possible that the open system behavior, as described previously for Sm-Nd, has affected U-Pb causing radiogenic Pb loss and skewing the younger dates. REE minerals would seem more susceptible to Pb loss as their breakdown during mineralizing and metasomatic events caused recrystallization and alteration of existing crystals (Fig. 8). However, the similarity of ages across all rock sample types in the system, including country rock, syenite, and ore, which have each formed under either igneous, metamorphic, or metasomatic conditions indicate that the younger dates are valid.

Considering both the age difference between older silicate and younger non-silicate REE minerals (Fig. 14 and 17) and mineral chemistry (Table 2), it is evident that non-silicate REE minerals, apatite-britholite, monazite, fergusonite, and REE carbonate have crystallized as a product of the breakdown of the silicate REE-bearing minerals. Allanite and titanite-(Ce) contain abundant Ca, Fe, Nb, Th, Ti, REE and Y, thereby, meeting the chemical requirements for cations in the formation of non-silicate REE minerals. Hence, it is reasonable to assume that a metasomatic event, related to

Grenvillian metamorphism altered the REE silicates, breaking them down into the non-silicate REE minerals, where excess silica and trace elements formed the gangue minerals, associated with britholite aggregates (Fig. 7a, 7b, and 10). Missing from this scenario is one ligand – carbonate. Carbonate likely entered the system during metasomatism as a late fluid phase, which acted as a reactant producing fine-grained, crack-filling REE-rich carbonate and calcite. The single niobate, fergusonite, has been produced by the breakdown of titanite and titanite-(Ce), which contains abundant Y_2O_3 and NbO_4 (Table 2). The following equations summarize the reactions between the older silicate REE minerals and younger non-silicate REE minerals:

Equation 2

$$\underset{Titanite-(Ce)}{(Ca_{0.2}REE_{0.8})(Fe_{0.5}Ti_{0.5})(SiO_4)_{0.9}(NbO4)_{0.1}} + 0.2CO_3 + \underset{fluids}{0.8PO_4} \leftrightarrow$$
$$\underset{Fergusonite}{0.1(REE_{0.5}Y_{0.5})NbO_4} + \underset{Monazite}{0.8REE(PO_4)} + \underset{Ilmenite}{0.5FeTiO_3} + \underset{Quartz}{0.9SiO_4} + \underset{Calcite}{0.2CaCO_3}$$

and,

Equation 3

$$\underset{Allanite}{5(Ca_{0.8}REE_{0.2}Y_{0.01})(Fe_{0.4}REE_{0.6})(Fe_{0.5}Al_{0.5})(Fe_{0.5}Al_{0.5})(SiO_4)_3OH} + CO_3 + \underset{fluids}{5.5PO_4} + 1.5F + 14OH \leftrightarrow$$
$$\underset{Britholite}{0.9(Ca_{3.5}REE_{1.0}Y_{0.5})(PO_4)_{1.5}(SiO_4)(F_{0.5}OH_{0.5})} + \underset{Apatite}{0.1Ca_5(PO_4)_3F_{1.0}} + \underset{Monazite}{REE(PO_4)} +$$
$$\underset{Quartz}{15SiO_4} + \underset{Calcite}{CaCO_3} + \underset{excess}{2.5Al_2O_3} + 7.5FeO$$

These reactions represent segregation of REE by breakdown of silicate REE minerals, Allanite and Titanite-(Ce), to REE phosphate minerals, REE carbonate minerals, REE niobate, and gangue minerals at Pope's Hill.

2.5.4 Metasomatic Origin of REE

REE enriched rocks at Pope's Hill show two textural features typical of hydrothermally altered rocks (Fig. 6, 7, 8, and 10): 1) the selective associations of apatite-britholite, monazite, calcite and quartz in britholite symplectite grains; and stoichiometric titanite, ilmenite and fergusonite in titanite-(Ce); and 2) epitactic replacement of titanite-(Ce) and allanite by non-silicate REE minerals, including isotopically homogenous monazite (Fig 16a), quartz and calcite. This is direct evidence for metasomatic alteration caused by hydrothermal fluid(s) – fluid that could introduce the missing carbonate and phosphate anions and fluorine (Eq. 2, 3).

The formation of REE minerals by hydrothermal activity is a complex process that requires the fulfillment of two sets of parameters: 1) REE must enter a fluid phase, and 2) REE minerals must reach saturation. Moving REE into a fluid phase is a process that is not well understood in geological systems (Gieré, 1996). Limited research and experimentation by Haas et al. (1995) has shown that the REE tend to be transported by complexing with a combination of ligands including, fluoride, chloride, hydroxide, sulphate or carbonate. Therefore, REE mobility is initially dependent on temperature, pressure, fluid composition, and ligand availability. Certain ligands may also cause fractionation between LREE and HREE, as observed with niobate in Nd-enriched fergusonite at Pope's Hill (Fig 12d).

After conditions of transport are met and an aqueous fluid of appropriate composition is formed, the fluid must become supersaturated in a REE mineral, or minerals, in order for it to crystallize; this introduces a new set of parameters, in addition to temperature and pressure, where REE minerals can form. Four mechanisms of

crystallization are outlined by Gieré, 1996: 1) changes in temperature and pressure as the fluid is moved through the crust; 2) mixing of REE-bearing fluid with another fluid, of a different composition; 3) host rock interactions; and 4) through the crystallization of other minerals from the fluid. At Pope's Hill it appears the later is most significant.

Second to REE-silicates, phosphate minerals host a major percentage of REE at Pope's Hill. Unfortunately, phosphates do not behave in straightforward manner in hydrothermal systems. A study by Ayers and Watson (1991) shows that temperature and pressure condition play a trivial role in apatite solubility. Experimental data from as high as 1200˚C and 2.0 GPa, in H_2O, did not see apatite dissolve or recrystallize and even throughout the entire range of pressure and temperature conditions were tested, solubility varied by tenths of percent. However, with a quench solution that included HCl to decrease pH, solubility greatly increased. In fact, increased solubility was present throughout experimental and ambient conditions, with a decrease in pH. Monazite behaves in a similar fashion; although its solubility tends to increase slightly with increasing pressure. It is found to be generally less soluble than apatite, with a solubility that also increases with decreasing pH. A study by Chaïrat *et al.* (2006) on dissolution rates of Nd-britholite indicate that pH remains the determining factor of solubility, despite significant silica content.

It seems evident that these low pH REE-complexes transported REE at Pope's Hill, but their method of deposition must be addressed. Significant quantities of the REE minerals are phosphates that must be the result of REE-complex-bearing hydrothermal fluids that have undergone a change in pH conditions (Ayers and Watson, 1991). As mentioned earlier in reference to Gieré (1996), there are four ways transportation of REE

can occur and alter the fluids pH: changing P&T conditions, fluid interaction, wall rock interaction and/or crystallization of another phase.

The predominance of phosphate and carbonate mineral species with between 0.18 and 3.46 wt % fluorine, while primary silicates contain no fluorine indicates that the REE from the silicates were mobilized by fluids rich in fluorine accompanied by phosphate and carbonate; these three ligands are known to initiate the transport of REE in hydrothermal systems (e.g., Kosterin, 1959; Giere, 1990; Boily and William-Jones, 1994; Migdisov et al., 2009; Sheard et al., 2012). Once each secondary REE mineral reaches saturation in the fluid, its crystallization has a dramatic effect on fluid pH and the activity of other elements and compounds (Gieré, 1996). Experimental-based modeling by Haas et al. (1995) showed that at standard conditions in the crust and neutral pH, fluorine plays the largest role in complexation of REE. Since only secondary REE minerals at Pope's Hill contain fluorine (Table 2), these minerals formed under similar, F-rich, pH neutral conditions. Primary, silicate REE minerals, allanite and titanite-(Ce), lack fluorine indicating they crystalized by a different mechanism and served as the elemental source for F-bearing, REE scavenging fluids, as replacement textures suggest (Fig. 6, 7, 8, 10).

The activity of carbonate as a REE-mobilizing ligand is also significant. In the secondary britholite symplectite, a product of metasomatism, the only carbonate to reach saturation is REE-free calcite. Trace concentrations of REE carbonates are present in two distinctly different textures throughout the mineralized and host rocks at Pope's Hill. In the mineralized rock it is primarily found in close association with other REE-minerals – allanite, titanite, apatite-britholite and monazite – in subhedral microcrystals. Throughout the host, REE-carbonate fills cracks in hedenbergite. This petrographic observation infers

the a hydrothermal fluid, containing both CO_3^{2-} and F^-, bonded with REE; thus confirming the complexation of REE as their method of transport. Haas et al. (1995) concludes that carbonates become the dominant REE mobilization ligand only at lower temperature, hence, the REE-carbonates in syenitic rock samples of Pope's Hill are likely the result of a later, low temperature fluid event. REE-carbonate in the mineralized samples may also be a product of this later alteration, or an indication of small amounts of REE complexation occurring during the primary, mineralizing fluid event.

Constraints provided by petrography (Fig. 6, 7, 8), mineral chemistry (Table 2; Fig. 10, 11), Sm-Nd isotope geochemistry (Table 6, Fig. 16), and geochronology (Table 7, Fig. 14) strongly suggest that the non-silicate REE minerals at Pope's Hill are secondary and result from hydrothermal breakdown of the primary REE minerals, allanite and titanite-(Ce), by low pH, carbonate, phosphate and halogen bearing fluids.

2.5.5 Igneous or Metamorphic Origin of REE

Unlike the non-silicate REE minerals, allanite and titanite-(Ce) do not contain significant fluorine, phosphorus, or carbonate. Grain boundaries depleted in REE and bordered by britholite aggregate grains suggests individual grains of titanite-(Ce) have been altered (Fig. 8 and 11) during the metasomatic event, indicating that REE-minerals predate metasomatism. High-grade metamorphism accompanied by ductile deformation took place throughout the granitic gneiss of the LBMS during the late Mesoproterozoic.

Since the ages of the allanite and titanite-(Ce) are Grenvillian and petrographic evidence shows that they predate the non-silicate REE minerals there are two possible mechanisms of formation: 1) the minerals grew at a point in time before metamorphism,

likely during crust building at ~1900-1600 Ma (Rivers, 1997) and have been completely overprinted by metamorphism during the Grenville orogeny; or 2) the minerals formed during the Grenville age magmatism that formed the Pope's Hill syenite. The later theory is supported by Sm-Nd data from the silicate and non-silicate ore minerals that are in close agreement (within analytical error), suggesting a common source. Additionally U-Pb dating of multiple REE minerals and ziron in the ore and syenite did not produce any results older than ~1200 Ma. As REE-enriched ore rock is hosted in structurally controlled, boudinaged pods, the primary REE minerals, allanite and titanite-(Ce), either predate or have crystallized during this deformation event. Considering both analytical data and textural observations we conclude that the primary REE minerals are a product of the Grenvillian orogeny, crystallizing during the late Mesoproterozoic.

Supporting the metamorphic origin of REE minerals at Pope's Hill is work by Wing et al. (2003), which traces monazite as it transitions to and from allanite in pelitic rocks under going prograde metamorphism. Although Pope's Hill lacks traditional metamorphic indicator minerals, the chemical reactions proposed by Wing et al. appear to account for a number of minerals found at Pope's Hill including quartz, various carbonate species, and thorite. The issue of a source and transport mechanism for phosphate, carbonate, and halogens is not well explained in this model.

2.5.6 Source of REE at Pope's Hill

Initial Nd isotope compositions suggest that the secondary REE minerals monazite and britholite obtained their REE (assuming Nd can be taken as a proxy for all other REE elements) from the primary REE minerals allanite and titanite-(Ce). The

source of REE in the primary assemblage then must be addressed. The Nd isotope composition of the primary minerals allanite and titanite-(Ce) (ϵNd_{984} of +0.3) is notably more radiogenic than that of syenite as recorded by monazite (ϵNd_{984} of -2.4). The more radiogenic Nd isotope composition of the ore minerals requires contribution of a more radiogenic component. Given the exceptionally high Nd content of the primary minerals, many weight percent Nd_2O_3, the more radiogenic component likely requires a substantially more radiogenic composition and must have contributed a proportion of REE in order to leverage the Nd isotope composition of the syenite, assuming that the syenite was a source of REE elements in the later ore minerals. Alternatively, the syenite and/or country rock may not represent a substantial source component of the REE in the Pope's Hill ores. While these ores can potentially be explained by full or partial contribution of REE from a depleted source such as the mantle, at present there are few isotope constraints available to fully address the sources of REEs in the initial ore forming minerals. Unlike the study of Buchanan et al. (2015), where exceptionally high REE content of apatite in the Adirondack iron oxide apatite (IOA) deposits can be entirely accounted for by the rocks which host the deposit, the ores at Pope's Hill require a source other than the rocks which host the deposit.

2.5.7 Paragenesis of Minerals at Pope's Hill

A paragenetic sequence for the Pope's Hill samples is shown in Figure 17, which has been constructed using the LA-ICPMS (Table 4, Fig. 13 and 16) and ID-TIMS (Table 7, Fig. 13 and 14) data. These data indicate three populations of age data: 1) formation of country rock zircon beginning at ~1200 Ma during regional Grenvillian magmatism and

metamorphism in the LBMS; 2) slow cooling of country rock zircon continues as crystals close to radiogenic Pb loss while syenitic zircon forms along with allanite and titanite-(Ce), during metamorphism at 1060 to 1020 Ma; and 3) crystallization of hydrothermal ore zircon and rims of syenitic zircon at between 1012 and 999 Ma followed by the breakdown of primary REE silicates into F-bearing non-silicate phases with carbonate, phosphate and niobate as ligands provided by metasomatic fluid at the ore monazite age of 984 Ma, followed by relative slow cooling reflected in progressively younger ages of minerals with lower closure temperature to radiogenic Pb loss. Petrographically, coarse-grained monazite occurs primarily inside of apatite-britholite aggregate grains along with calcite and quartz, and its date of 984±1 Ma constrains the crystallization age of the britholite symplectite grains as ~985 Ma or less. The breakdown of silicate REE phases to non-silicate REE phases is supported by identical initial Nd isotope compositions at the age of non-silicate REE mineral growth.

2.6 CONCLUSIONS

The concentration of REE at Pope's Hill, up to ~21% REE, is remarkable for Labrador, where REE deposits typically contain <1% to 8% REE_2O_3 (Kerr, 2011). The REE are hosted in a variety of minerals, which likely formed during the continent-continent phase of Grenvillian orogenesis (Corrigan and Hanmer, 1995, Rivers, 1997). Its protracted history of metamorphism, metasomatism and tectonic deformation during back arc extension and intra-plate plutonism (River, 1997) make Pope's Hill an excellent natural laboratory for the study of metasomatic alteration by hydrothermal fluids and the

emplacement of REE mineralization, its preservation and destruction through complex geological processes.

1) REE at Pope's Hill are found in dark grey-red boudinaged massive "pods" that assay up to 21% REE (Table 1) and are hosted in syenite (Fig. 3). The pods contain a variety of silicate and non-silicate REE minerals that contribute to the rocks high enrichment, from highest contribution to lowest (Fig. 6, 7; Table 8), allanite, titanite-(Ce), monazite, and britholite, with a minor percentage in fergusonite, REE carbonate and (stoichiometric) apatite. Apatite-britholite and titanite represent a continuum of compositions from stoichiometric, lacking REE, to strongly enriched (Fig. 11)

2) Sm-Nd radiogenic isotope data indicate that REE silicates, allanite, and titanite-(Ce), crystallized from an isotopically homogenous source (Fig. 16) at 1100 and 1020 Ma coinciding with the crystallization of zircon in the LBMS country rock, and cores of syenitic zircon (Fig. 13). The Nd isotope composition of allanite and titanite-(Ce), suggests a local source for the REE, however simple mass balance considerations require contribution from a more radiogenic source yet to be identified.

3) Textural evidence (Fig. 6, 7, 8, 10) coupled with Nd isotope data show that allanite and titanite-(Ce) experienced deterioration via metasomatic alteration, mobilizing REE via a F-rich hydrothermal fluid and crystallizing isotopically homogenous hydrothermal monazite (Fig 16a) between 1020 and 980 Ma (Fig. 14, 15, 17). In addition to monazite, this metasomatic event crystallized all other secondary non-silicate REE minerals: apatite-britholite, fergusonite, and trace amounts of xenotime, thorite, ilmenite, pyrite, galena, and carbonate; while remnant silicate contributed to crystallization of stoichiometric titanite and quartz. Breakdown of allanite and titanite-(Ce) provided

cations, including REE, for the crystallization of these non-silicate minerals and anions (the ligands, fluorine, phosphorous, carbonate, and niobate) were provided by the metasomatic fluid.

4) Similar to other Grenvillian-age REE deposits (e.g., IOA –REE deposits in the Adirondacks, Buchanan et al., 2015), age and radiogenic isotope data at Pope's Hill point to a multi-stage evolution, where REE are initially concentrated (perhaps not in economically sufficient concentrations) in low grade deposits which are later dissolved, recrystallized, and possibly transported in the presences of fluorine- and other ligand-rich fluids, to further concentrate REE into more economically viable ores. At Pope's Hill, the REE mineralization appears to have been formed in the waning stages of continent-continent collisions, likely during extension.

CHAPTER 3: CONCLUSIONS

3.1 Summary

(Work was summarized in the previous section, 2.6).

3.2 Direction of Future Work

While this study was a detailed look at REE enriched rocks that occur in structurally controlled pods at the Pope's Hill REE Occurrence, future works may want to conduct mineralogical or wider-scale regional investigations. These include:

(1) Classification of the REE-enriched titanite end-member titanite-(Ce) by heat-induced annealing and XRD (e.g. Beirau et al., 2012) would provide great insight into its identity and structure.

(2) A larger scale regional sampling program of REE-enriched rocks and minerals from the Pope's Hill area may shed light on the source of REE and metasomatic fluids parental to the minerals at Pope's Hill.

(3) A study of Grenvillian REE deposits focusing on comparing the mineralogy, structure, tectonic setting, and ages of rocks and minerals at Pope's Hill to that found in the REE occurrences at the Port Hope Simpson REE District. This may show a regional connection between the two and indicate common traits that lead to the identification of similar deposits in the Grenville.

References

Anders, E., and Grevesse, N., 1989, Abundances of the elements: Meteoritic and solar: Geochimica et Cosmochimica Acta, v. 53, no. 1, p. 197-214.

Ayers, J. C., Watson, E. B., Ayers, J. C., and Watson, E. B., 1991, Solubility of apatite, monazite, zircon, and rutile in supercritical aqueous fluids with implications for subduction zone geochemistry: Philosophical Transactions of the Royal Society of London. Series A: Physical and Engineering Sciences, v. 335, no. 1638, p. 365-375.

Beirau, T., Mihailova, B., Matveeva, G., Kolb, U., Malcherek, T., Groat, L. A., & Bismayer, U. 2012. Structural anisotropy and annealing-induced nanoscale atomic rearrangements in metamict titanite. *American Mineralogist*, *97*(8-9), 1354-1365.

Berman, J., 1955, Identification of Metamict Minerals by X-Ray Diffraction: Am. Mineral, v. 40, p. 805-827.

Boily, M., and Williams-Jones, A. E., 1994, The role of magmatic and hydrothermal processes in the chemical evolution of the Strange Lake plutonic complex, Québec-Labrador: Contributions to Mineralogy and Petrology, v. 118, no. 1, p. 33-47.

Bouvier, A., Vervoort, J. D., & Patchett, P. J., 2008, The Lu–Hf and Sm–Nd isotopic composition of CHUR: constraints from unequilibrated chondrites and implications for the bulk composition of terrestrial planets. *Earth and Planetary Science Letters*, *273*(1), 48-57.

Buchanan, A. L. 2015. Tracking hydrothermal alteration and mineralization in rock-forming and accessory minerals from the Lyon Mountain Granite and related iron oxide apatite (IOA) ores from the Adirondack Mountains, New York State. (Unpublished master's thesis). Retrieved from Earth Sciences Dept., Memorial University of Newfoundland.

Castor, S. B., & Hedrick, J. B. 2006. Rare earth elements. *Industrial Minerals volume, 7th edition: Society for Mining, Metallurgy, and Exploration, Littleton, Colorado*, 769-792.

Chaïrat, C., Oelkers, E. H., Schott, J., and Lartigue, J. E., 2006, An experimental study of the dissolution rates of Nd-britholite, an apatite-structured actinide-bearing waste storage host analogue: Journal of nuclear materials, v. 354, no. 1, p. 14-27.

Chou, I-M., Eugster, H. P., 1977. Solubility of magnetite in supercritical chloride solutions. American Journal of Science, 277, p. 1296-1314.

Corrigan, D., Hanmer, S., 1995. Arc accretion, thickening, post- collisional extension and plutonism in the Grenville orogen; constraints from the Mauricie region, south-central Quebec. In: Precambrian '95, International Conference on Tectonics and

Metallogeny of Early/Mid Precambrian orogenic Belts, Program and Abstracts, Montreal, p. 106.

Drew, L. J., Meng, Q., Sun, W., 1990. The Bayan Obo iron-rare earth-niobium deposit, Inner Mongolia, China–Contraints on mineralization and Deposition of the Bayan Obo Group. Economic Geology, 87, p. 185-188.

Fisher C. M., McFarlane, , C. R. M., Hanchar, J. M., Schmitz, M. D., Sylvester, P. J., Lam, R., Longerich, H. P., (2011). Sm–Nd isotope systematics by laser ablation-multicollector-inductively coupled plasma mass spectrometry: Methods and potential natural and synthetic reference materials.

Fleet, M. E., and Pan, Y., 1994, Site Preference of Nd in Fluorapatite [$Ca_{10}(PO_4)_6F_2$]: Journal of Solid State Chemistry, v. 112, no. 1, p. 78-81.

Fleet, M. E., and Pan, Y.,, 1995, Site preference of rare earth elements in fluorapatite: American Mineralogist, v. 80, no. 3, p. 329-335.

Fleet, M. E., and Pan, Y.,, 1997, Site preference of rare earth elements in fluorapatite: Binary (LREE+ HREE)-substituted crystals: American Mineralogist, v. 82, no. 9, p. 870-877.

Gerstenberger, H., and Haase, G., 1997, A highly effective emitter substance for mass spectrometric Pb isotope ratio determinations: Chemical Geology, v. 136, no. 3–4, p. 309-312.

Gieré, R., 1990, Hydrothermal mobility of Ti, Zr and REE: examples from the Bergell and Adamello contact aureoles (Italy): Terra Nova, v. 2, no. 1, p. 60-67.

Gieré, R., 1996, Formation of Rare Earth Minerals in Hydrothermal Systems, in Jones, A. P., Wall, F., and Williams, C. T., eds., Rare Earth Minerals: Chemistry, Origin and Ore Deposits, Chapman & Hall.

Gieré, R., and Sørensen, S. S., 2004, Allanite and other REE-rich epidote-group minerals: Reviews in Mineralogy and Geochemistry, v. 56, no. 1, p. 431-493.

Goonan, T.G., 2011, Rare Earth Elements–End Use and Recyclability, U.S. Geological Survey Scientific Investigations Report 2011-5094, 15p. http://pubs.usgs.gov/sir/2011/5094/.

Goudie, D. J., Fisher, C. M., Hanchar, J. M., Crowley, J. L., & Ayers, J. C. (2014). Simultaneous in situ determination of U- Pb and Sm- Nd isotopes in monazite by laser ablation ICP- MS. *Geochemistry, Geophysics, Geosystems*, *15*(6), 2575-2600.

Gower, C., and Ryan, A., 1986, Proterozoic evolution of the Grenville Province and adjacent Makkovik Province in eastern-central Labrador: The Grenville Province. Edited by JM Moore, A. Davidson, and AJ Baer. Geological Association of Canada, Special Paper, v. 31, p. 281-296.

Gower, C. F., Haley, J., Moran, C. and Chafe, A., 2011, Eastern Labrador Field Excursion for Explorationists., in Resources, D. o. N., ed.: Government of Newfoundland and Labrador, Geological Survey, p. 44.

Gower, C. F., and Krogh, T. E., 2002, A U-Pb geochronological review of the Proterozoic history of the eastern Grenville Province: Canadian Journal of Earth Sciences, v. 39, no. 5, p. 795-829.

Gower, C. F., 2002, A U-Pb geochronological review of the Proterozoic history of the eastern Grenville Province: Canadian Journal of Earth Sciences, v. 39, no. 5, p. 795-829.

Gu, Y. and Napier-Munn, T., 1997, JK/Philips mineral liberation analyzer – an introduction. *In* Minerals Processing '97 Conf., Cape Town, SA, p. 2.

Haas, J. R., Shock, E. L., and Sassani, D. C., 1995, Rare earth elements in hydrothermal systems: estimates of standard partial molal thermodynamic properties of aqueous complexes of the rare earth elements at high pressures and temperatures: Geochimica et Cosmochimica Acta, v. 59, no. 21, p. 4329-4350.

Haxel, G. B., Hedrick, J. B., Orris, G. J., 2002, Rare Earth Elements—Critical Resources for High Technology: U.S. Geological Survey, U.S. Department of the Interior, USGS Fact Sheet 087-02.

Henderson, P., 1982, Inorganic geochemistry. Pergamon, London, 364p.

Holland, H. D., & Gottfried, D., 1955., The effect of nuclear radiation on the structure of zircon. *Acta Crystallographica*, *8*(6), 291-300.

Hughes, J.M., Bloodaxe, E.S., Hanchar, J.M. and Foord, E.E., 1997, Incorporation of rare earth elements in titanite: stabilization of the A2/a dimorph by creation of antiphase boundaries. *American Mineralogist,* 82: 512-516.

James, D., Kamo, S., Krogh, T., and Nadeau, L., 2002, Preliminary report on U-Pb ages for intrusive rocks from the Western Mealy Mountains and Wilson Lake terranes, Grenville Province, southern Labrador: St. John's, Newfoundland, Department of Mines and Energy Geological Survey, Report, p. 02-01.

Kerr, A., 2011, Rare-Earth-Element (REE) Mineralization In Labrador: A Review Of Known Environments And The Geological Context Of Current Exploration Activity: Newfoundland and Labrador Department of Natural Resources, Report 11-1.

Kosterin, A., 1959, The possible modes of transport of the rare earths by hydrothermal solutions: Geochemistry, v. 4, p. 381-387.

Wyllie, P. J., & Lee, W. J. (1998). Model system controls on conditions for formation of magnesiocarbonatite and calciocarbonatite magmas from the mantle. *Journal of*

Petrology, *39*(11-12), 1885-1893.

Ludwig, K., 2003, Isoplot/Ex Version 3.00: a geological toolkit for Microsoft Excel: Berkeley Geochronology Center Special Publication, 70pp, v. 4.

Markl, G., 2001, A new type of silicate liquid immiscibility in peralkaline nepheline syenites (lujavrites) of the Ilimaussaq complex, South Greenland, Contrib Min Petrol, 141, p. 458-472.

Migdisov, A. A., Williams-Jones, A., and Wagner, T., 2009, An experimental study of the solubility and speciation of the Rare Earth Elements (III) in fluoride-and chloride-bearing aqueous solutions at temperatures up to 300 C: Geochimica et Cosmochimica Acta, v. 73, no. 23, p. 7087-7109.

Miller, R. R., 1986, Geology of the Strange Lake Complex and the Associated Zr-Y-Nb-Be-REE Mineralization: Newfoundland and Labrador Department of Mines and Energy, Report 86-1.

Mulcahy, S.R., King, R.L., and Vervoort, J.D., 2009, Lawsonite Lu-Hf geochronology: A new geochronometer for subduction zone processes: Geology, v. 37, p. 987-990.

Olson, J. C., Shawe, D. R., Pray, L. C., & Sharp, W. N. (1954). Rare-earth mineral deposits of the Mountain Pass district, San Bernardino county, California. *Science*, *119*(3088), 325-326.

Pan, Y., and Fleet, M. E., 2002, Compositions of the apatite-group minerals: Substitution mechanisms and controlling factors: Reviews in mineralogy and geochemistry, v. 48, no. 1, p. 13-49.

Parrish, R. R., 1990, U-Pb dating of monazite and its application to geological problems: Canadian Journal of Earth Sciences, v. 27, no. 11, p. 1431-1450.

Pasero, M., Kampf, A. R., Ferraris, C., Pekov, I. V., Rakovan, J., and White, T. J., 2010, Nomenclature of the apatite supergroup minerals: European Journal of Mineralogy, v. 22, no. 2, p. 163-179.

Paton, C., Hellstrom, J., Paul, B., Woodhead, J., and Hergt, J., 2011, Iolite: Freeware for the visualisation and processing of mass spectrometric data: Journal of Analytical Atomic Spectrometry, v. 26, no. 12, p. 2508-2518.

Raczek, I., Stoll, B., Hofmann, A. W., & Peter Jochum, K., 2001, High- Precision Trace Element Data for the USGS Reference Materials BCR- 1, BCR- 2, BHVO- 1, BHVO- 2, AGV- 1, AGV- 2, DTS- 1, DTS- 2, GSP- 1 and GSP- 2 by ID-TIMS and MIC- SSMS. Geostandards Newsletter, v. 25, no. 1, p. 77-86.

Raczek, I., Jochum, K. P., & Hofmann, A. W., 2003, Neodymium and Strontium Isotope Data for USGS Reference Materials BCR- 1, BCR- 2, BHVO- 1, BHVO- 2,

AGV- 1, AGV- 2, GSP- 1, GSP- 2 and Eight MPI- DING Reference Glasses. Geostandards Newsletter, v. *27*, no. 2, p. 173-179.

Rivers, T., 1997, Lithotectonic elements of the Grenville Province: review and tectonic implications: Precambrian Research, v. 86, no. 3, p. 117-154.

Salvi, S., and Williams-Jones, A. E., 1990, The role of hydrothermal processes in the granite-hosted Zr, Y, REE deposit at Strange Lake, Quebec/Labrador: Evidence from fluid inclusions: Geochimica et Cosmochimica Acta, v. 54, no. 9, p. 2403-2418.

Salvi, S., and Williams-Jones, A. E., 1996, The role of hydrothermal processes in concentrating high-field strength elements in the Strange Lake peralkaline complex, northeastern Canada: Geochimica et Cosmochimica Acta, v. 60, no. 11, p. 1917-1932.

Salvi, S., and Williams-Jones, A. E., 2006, Alteration, HFSE mineralisation and hydrocarbon formation in peralkaline igneous systems: Insights from the Strange Lake Pluton, Canada: Lithos, v. 91, no. 1–4, p. 19-34.

Schärer, U., and Gower, C. F., 1988, Crustal evolution in eastern Labrador: Constraints from precise U-Pb ages: Precambrian Research, v. 38, no. 4, p. 405-421.

Schärer, U., Krogh, T. E., and Gower, C. F., 1986, Age and evolution of the Grenville Province in eastern Labrador from U-Pb systematics in accessory minerals: Contributions to Mineralogy and Petrology, v. 94, no. 4, p. 438-451.

Schmitz, M.D., Vervoort, J.D., Bowring, S.A., and Patchett, P.J., 2004, Decoupling of the Lu-Hf and Sm-Nd isotope systems during the evolution of the granulitic lower crust beneath southern Africa: Geology, v. 32, p. 405-408.

Schmitz, M. D., and Schoene, B., 2007, Derivation of isotope ratios, errors, and error correlations for U–Pb geochronology using 205 Pb–235 U–(233 U)-spiked isotope dilution thermal ionization mass spectrometric data: Geochemistry, Geophysics, Geosystems, v. 8, no. 8, p. 1-20.

Sheard, E. R., Williams-Jones, A. E., Heiligmann, M., Pederson, C., and Trueman, D. L., 2012, Controls on the Concentration of Zirconium, Niobium, and the Rare Earth Elements in the Thor Lake Rare Metal Deposit, Northwest Territories, Canada: Economic Geology, v. 107, no. 1, p. 81-104.

Smith, M., Chengyu, W., 2000, The Geology and Genesis of the Bayan Obo REE Deposit: A Review. In Porter T.M. (Ed.) Hydrothermal Iron Oxide Copper-Gold & Related Deposits: A Global Perspective, PGC Publishing, v. 1, p. 271-281.

Sørensen, H., 1997, The agpaitic rocks–an overview, Mineralogical Magazine, 61, p. 485-498.

Stacey, J. S., and Kramers, J., 1975, Approximation of terrestrial lead isotope evolution by a two-stage model: Earth and Planetary Science Letters, v. 26, no. 2, p. 207-221.

Taylor, S.R., and McLennan, S.M., 1985, The continental crust: its composition and evolution: Blackwell Scientific Pub.

Wang, H., 1985, Atlas of the Paleogeography of China. Cartographic Publishing House, Beijing, p. 143

Wardle, R. J., 1990, Geology of the Minipi River Area (NTS 13C/NW): Newfoundland and Labrador Department of Mines and Energy, Report 90-1.

Wardle, R. J., Gower, C. F., Ryan, B., Nunn, G. A. G., James, D. T., and Kerr, A., 1997, Geological Map of Labrador: Government of Newfoundland and Labrador, Department of Mines and Energy, Geological Survey, scale 1:1 million.

Weis, D., Kieffer, B., Maerschalk, C., Barling, J., de Jong, J., Williams, G. A., Hanano, D., Pretorius, W., Mattielli, N., Scoates, J. S., Goolaerts A., Friedman, R. M., Mahoney, J. B. 2006. High- precision isotopic characterization of USGS reference materials by TIMS and MC- ICP- MS. Geochemistry, Geophysics, Geosystems, v. 7 no. 8.

Wing, B. A., Ferry, J. M., and Harrison, T. M., 2003, Prograde destruction and formation of monazite and allanite during contact and regional metamorphism of pelites: petrology and geochronology: Contributions to Mineralogy and Petrology, v. 145, no. 2, p. 228-250.

Zhang, P., 1991, Mineralogical research of the Bayan-Obo rare earth – niobium – iron ore deposit. Journal of the Rare Earths, 9, 221-225.

APPENDIX 1: Analytical Results

This appendix contains analytical results that were not presented in the main body of the thesis.

A1.1 Summary of Work Completed on Samples from Pope's Hill

Samples are organized based on their PH-*n* label (Table A1). Former sample labels are from laboratory analyses, geological mapping, prospecting, and diamond drill core.

A1.2 Whole Rock ID-TIMS Results

Whole rock SM-Nd results from analysis completed by ID-TIMS at MUN (Table A2).

TABLE A1: WORK COMPLETED

Sample Name	Former Label[1]	Rock Type[2]	Sample Type[3]	Thin Section	Whole Rock		EPMA	SEM-MLA	XRD	LA-ICPMS			
					Major/Trace Elements	Sm/Nd				Trace Elements	U/Pb Age Dating	Sm/Nd Age Dating	Grain Mount
PH-01	470378	Ore	Grab	x	x	x	x	x	x	x	x	x	x
PH-02	941427	Ore	Grab	x	x		x		x	x		x	
PH-03	PH-MP-01	Ore	Grab	x	x				x	x			
PH-04	470329	Ore	Grab		x				x				
PH-05	AC-11-006	Syenite	Mapping	x	x	x	x	x	x	x	x	x	x
PH-06	Tr-1-01	Syenite	Mapping	x	x		x		x				
PH-07	Tr-2-02	Syenite	Mapping	x	x		x		x				
PH-08	AC-11-025	Andesite	Mapping	x	x				x				
PH-09	AC-11-030	Andesite	Mapping	x	x				x				
PH-10	PH-11-04	Granite	Drill Core		x	x			x		x	x	x
PH-11	Tr-2-01	Hbl Syenite	Mapping	x	x		x		x				
PH-12	470328	Ore	Grab	x			x			x			
PH-13	470379	Ore	Grab	x			x						
PH-14	PH-MP-02	Syenite	Grab	x									
PH-15	AC-11-029	Sedimentary	Mapping	x									
MRT-01	470261	Ore	Grab	x	x		x		x	x			
MRT-02	470259	Ore	Grab	x	x		x		x				
MRT-03	Tr-3-01	Syenite	Mapping	x	x		x		x				
MRT-04	Tr-3-02	Andesite	Mapping	x	x				x				
MRT-05	Tr-3-03	Ore	Mapping	x	x		x		x				

Note: "x" indicates analysis was performed.

[1]These sample labels were used during collection of field data and laboratory analyses.

[2]All rock units belong to the gneiss of the Lower Brook formation and can therefore, syenite, andesite and sedimentary are proceeded by "gneiss".

[3]Whole rock grab samples come from either regional mapping program, prospecting samples or diamond drill core.

Table A1

Summary of work completed on samples taken from Pope's Hill.

TABLE A2: WHOLE ROCK ID-TIMS RESULTS

Sample	Nd ppm	Sm ppm	$^{147}Sm/^{144}Nd$	$^{143}Nd/^{144}Nd$	2s
Rock:					
PH-1	31076	5230	0.1031	0.512059	0.000007
PH-5	230.6	22.34	0.0585	0.511604	0.000007
PH-10	139.3	27.57	0.1196	0.512143	0.000007
BCR Analysis					
1	27.73	6.354	0.1385	0.512633	0.000007
2	27.62	6.324	0.1384	0.512642	0.000007
3	27.63	6.328	0.1385	0.512631	0.000009
4	27.83	6.357	0.1381	0.512629	0.000007
5	27.58	6.317	0.1385	0.512643	0.000007
6	27.78	6.334	0.1378	0.512638	0.000007
7	27.61	6.31	0.1381	0.512635	0.000007
8	27.53	6.301	0.1384	0.512641	0.000007
2 std	0.21	0.040	0.0005	0.000011	

Table A2

ID-TIMS Results from whole rock samples of Pope's Hill with BCR standard analyses

A1.3: SEM-MLA

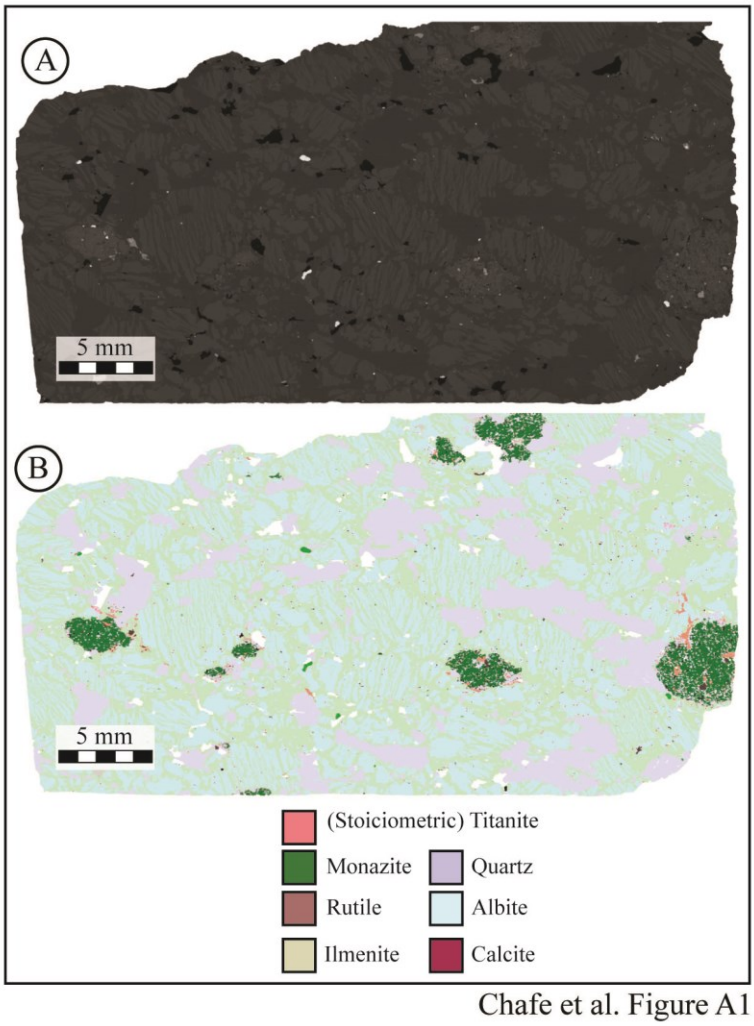

Figure A1

SEM-MLA generated BSE (A, top) and false color (B, below) images of thin section sample PH-5, Pope's Hill syenite. Legend indicates color of mineral in B.

A1.4 XRD

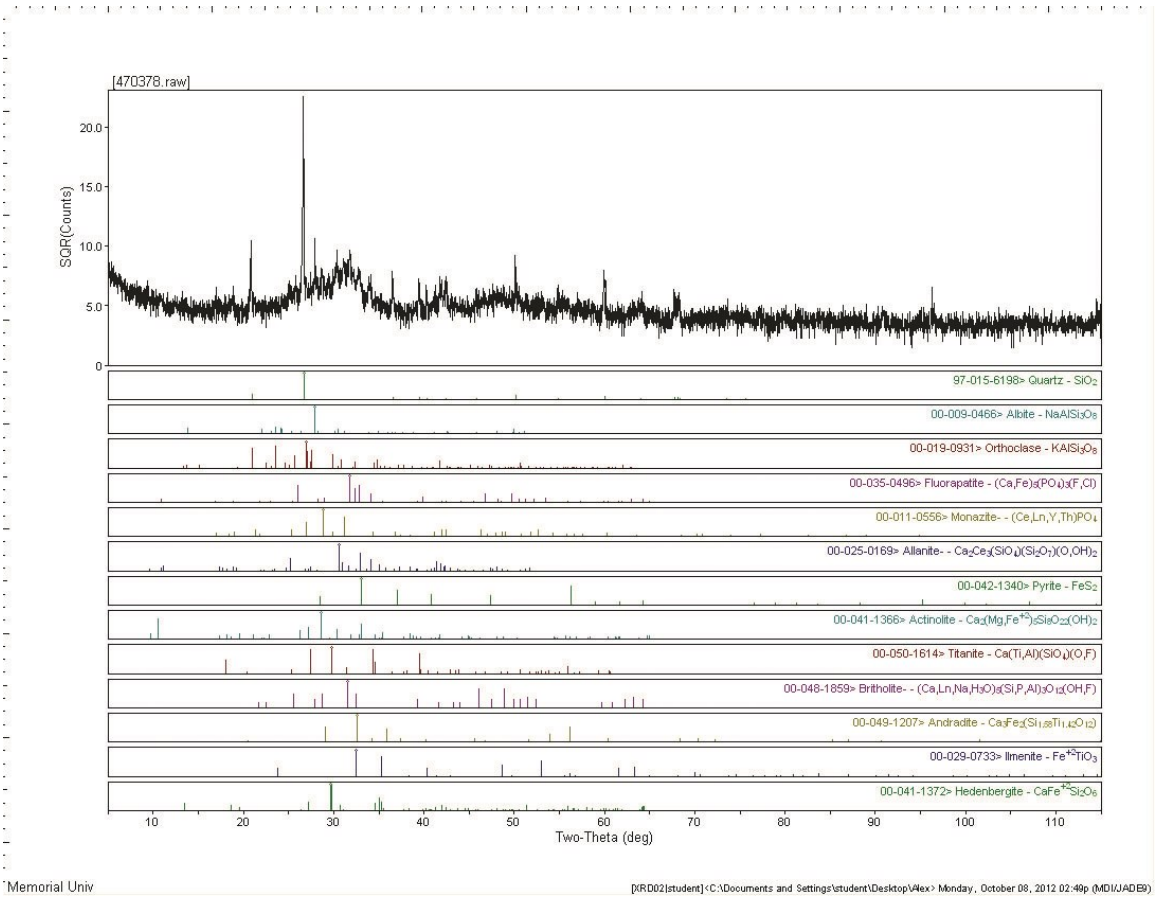

Figure A2

XRD Spectra of sample PH-1 (above), with stick plots showing XRD peaks for minerals identified during EPMA analyses.

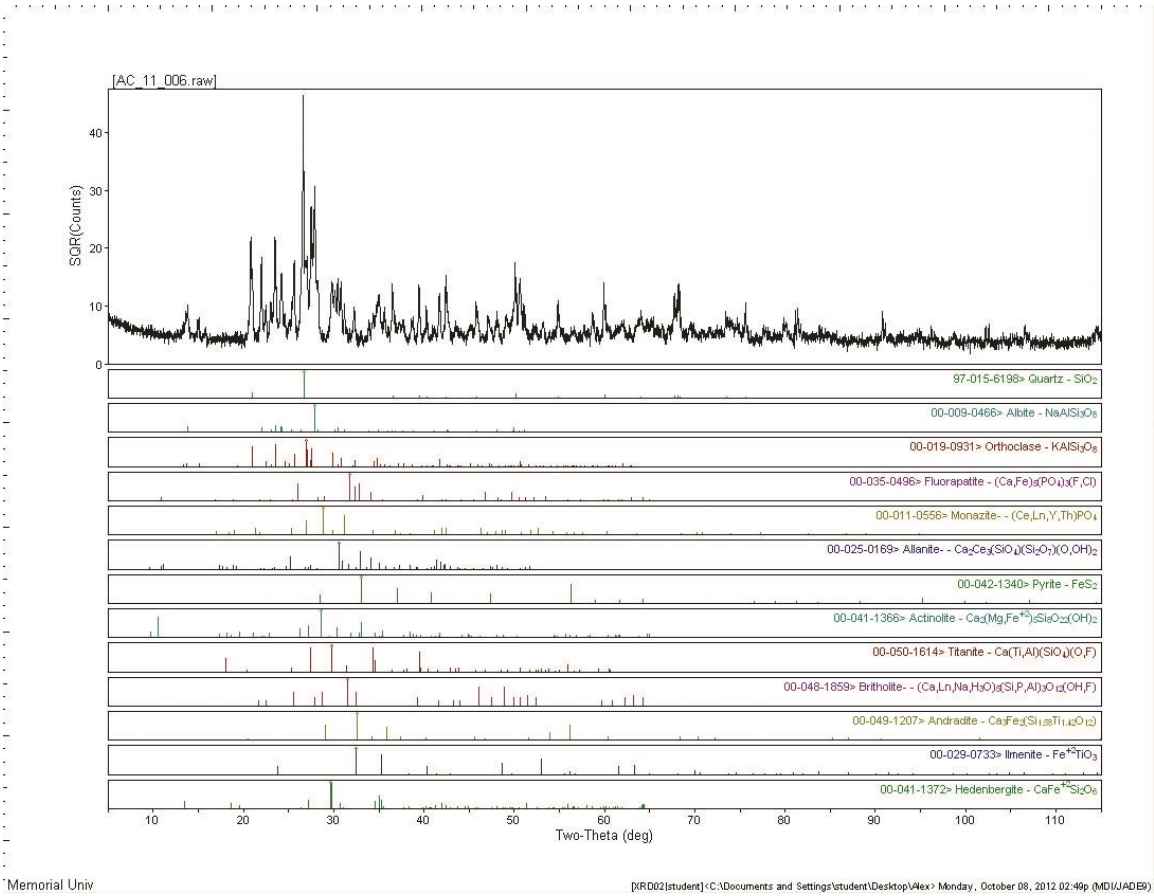

Figure A3

XRD Spectra of sample PH-5 (above), with stick plots showing XRD peaks for minerals identified during EPMA analyses.